AFRL-VS-TR-2000-1581

# THE AIR FORCE STATISTICAL AURORAL MODELS (AFSAM): FUNCTIONAL REPRESENTATIONS

William J. McNeil

Radex, Inc.
Three Preston Court
Bedford, MA 01730

June 28, 1999

Scientific Report #3

20010625 105

This technical report has been reviewed and is approved for publication

ALAN D. REBELLO
Contract Manager

FRANK A. ZAWADA, Lt Col, USAF
Branch Chief

# REPORT DOCUMENTATION PAGE

| 1. AGENCY USE ONLY (Leave Blank) | 2. REPORT DATE 28 June 1999 | 3. REPORT TYPE AND DATES COVERED Scientific Report No. 3 |
|---|---|---|

**4. TITLE AND SUBTITLE**

The Air Force Statistical Auroral Models (AFSAM): Functional Representations

**5. FUNDING NUMBERS**

PE 63871 C

PR 7659 TA GY WU AG

Contract F19629-98-C-0010

**6. AUTHORS**

William J. McNeil

**7. PERFORMING ORGANIZATION NAME(S) AND ADDRESS(ES)**
Radex, Inc.
Three Preston Court
Bedford, MA 01730

**8. PERFORMING ORGANIZATION REPORT NUMBER**

RXR-990601

**9. SPONSORING / MONITORING AGENCY NAME(S) AND ADDRESS(ES)**
Air Force Research Laboratory/VSSW
29 Randolph Road
Hanscom AFB, MA 01731-3010
Contract Manager: Robert J. Raistrick/VSSW

**10. SPONSORING / MONITORING AGENCY REPORT NUMBER**

AFRL-VS-TR-2000-1581

**11. SUPPLEMENTARY NOTES**

**12a. DISTRIBUTION / AVAILABILITY STATEMENT**

Approved for Public Release
Distribution Unlimited

**12b. DISTRIBUTION CODE**

**13. ABSTRACT** (Maximum 200 words)

We document here the Air Force Statistical Auroral Models (AFSAM), a set of empirical models for average auroral quantities. The quantities include electron and ion integral energy flux, number flux and average energy and the Pedersen and Hall conductivities. These quantities were computed by first computing average electron and ion spectra measured from the DMSP satellites, then converting these average spectra into the several quantities as a function of corrected geomagnetic latitude and magnetic local time. The two-dimensional maps were then fit to functional forms to reduce noise and provide continuity. The models are available as Fortran subroutines giving continuous values of each of the properties at either seven levels of $K_p$ or 30 combinations of solar wind speed with interplanetary magnetic field. This report describes the process and results of fitting of the model and gives references to the calculation of the properties themselves.

**14. SUBJECT TERMS**
AFSAM, Auroral oval, Auroral properties, Auroral models, Average aurora

**15. NUMBER OF PAGES**

**16. PRICE CODE**

| 17. SECURITY CLASSIFICATION OF REPORT Unclassified | 18. SECURITY CLASSIFICATION OF THIS PAGE Unclassified | 19. SECURITY CLASSIFICATION OF ABSTRACT Unclassified | 20. LIMITATION OF ABSTRACT SAR |
|---|---|---|---|

# Table of Contents

# List of Figures

**Color Plates**

# List of Tables

# Acknowledgment

# Executive Summary

Since 1985, the Air Force Research Laboratory (AFRL) has created a series of statistical auroral models based on electrostatic analyzer data (electron and ion flux) from the Defense Meteorological Satellite Program (DMSP) satellites. This report documents our recently completed major upgrades to these models which are now available to the community in digital form for incorporation into graphical display codes, as input to forecasting models, and for use in basic research applications. These have been designated as the Air Force Statistical Auroral Models (AFSAM).

The creation of these models required averaging the raw data to create average spectra, defined over a spatial grid in corrected geomagnetic latitude and magnetic local time coordinates. Individual maps were constructed for a wide range of auroral activities, parameterized both by $K_p$ and by solar wind conditions. From these averaged spectra, a number of averaged quantities were derived including integral number flux, integral energy flux, and average energies for both electrons and ions, and the Hall and Pedersen conductivities. All these quantities represent important drivers for many models of ionospheric and thermospheric dynamics. To facilitate the use of these models the gridded hemispheric maps were fit to functional forms. This makes the maps available as easy–to–use subroutines and provides smoothing and continuity to the data sets.

An initial set of models similar to AFSAM was published by AFRL in 1987 and 1991. The upgrade described in this report represents significant improvements in several respects. The initial $K_p$ parameterized electron maps were constructed from data from the SSJ/3 sensors on DMSP F2,F4; and P78–1 satellites. These sensors had an energy range from 50 eV to 20 keV. The subsequent $K_p$ ion flux maps and all other quantities given in AFSAM, including revised electron fluxes, were generated from improved SSJ/4 sensors on DMSP F6 and F7 which measure both electron and ion flux in the energy range from 30 eV to 30 keV.

The initial models included a total of seven maps, at various $K_p$, for electron and ion energy and number flux along with the Hall and Pedersen conductivities. AFSAM adds both the electron and ion average energies to the available quantities. Also, the electron fluxes have been fit with slightly more complicated functional forms which better represent the data. Furthermore, an entirely separate set of 30 maps have been added to the model giving the same quantities, but binned in various divisions of the solar wind speed and interplanetary magnetic field. This allows for a completely independent way to estimate the aurora, which is presumably somewhat more precise, when parameters other than $K_p$ are available. Finally, all maps in AFSAM are drawn from the same set of DMSP measurements, for consistency, and have been processed and fit by essentially the same procedures.

1

The four color plates that follow this summary should serve to introduce the reader to the basic features of the AFSAM model. The plates show polar projections in corrected geomagnetic latitude from 50° to 90° and in magnetic local time, with midnight at the bottom and 0600 on the right, of the average auroral oval as depicted by the several quantities that can be generated by AFSAM. In the models, northern and southern aurora are considered to be identical.

Plate 1 shows a comparison between the original electron number and energy flux and Pedersen and Hall conductivity published in the initial release of the models [*Hardy et al.*, 1987] and those generated from AFSAM. It can be seen that the fluxes are slightly higher in AFSAM, and the conductivities are higher by perhaps 40%. This is due primarily to the coverage of higher energies by the later instruments. We can see as well, though, that the original models exhibit more artificial "bumps and bulges" as a function of latitude, since AFSAM includes more terms in the latitude expansion.

Plate 2 shows electron and ion number fluxes for ascending $K_p$ activity. AFSAM represents here both the equatorward expansion of the oval and the intensification of the particle flux. The model also captures quite well the day–side cusp or intensification of low energy ions between 70° and 80°. This is an important feature for several applications. Plate 3 shows the same sort of progression in electron and ion number flux as $B_z$ moves from south to north, for a set solar wind velocity of 485 km/s. Again we see clearly defined cusps and the expansion and intensification of auroral fluxes. This progression is available in AFSAM at a total of six fixed values of solar wind velocity ranging from 345 km/sec to 675 km/sec.

Plate 4 compares the raw data, that is, the binned average maps of the auroral quantities, with the results of the model for electron energy and number flux and for electron average energy. These are for a $B_z$ of -4.5 and a solar wind speed of 485 km/s. We see here how the AFSAM result has provided smoothing of the statistical noise in the original maps and has also "filled in" some gaps at mid–latitude caused by inadequate satellite coverage in these regions. The general shape of the ovals, as well as the intensity, can be seen to be reproduced extremely well by the fits. This is evidence of the care taken in modeling as well as the quality of the original data set itself.

AFSAM is available as a series of Fortran subroutines with accompanying ASCII data files for incorporation into modeling, forecasting and visualization codes. The subroutines are quite simple and can be readily converted to C or any other popular language. The entire series of the AFSAM models can be obtained through Dr. Donald Brautigam, Air Force Research Laboratory / VSBS, Hanscom AFB, MA 01731, or by writing to brautigam@plh.af.mil.
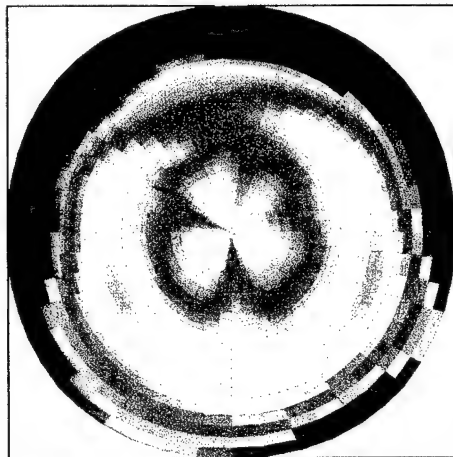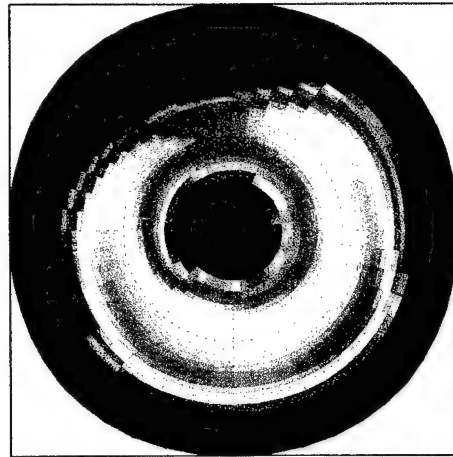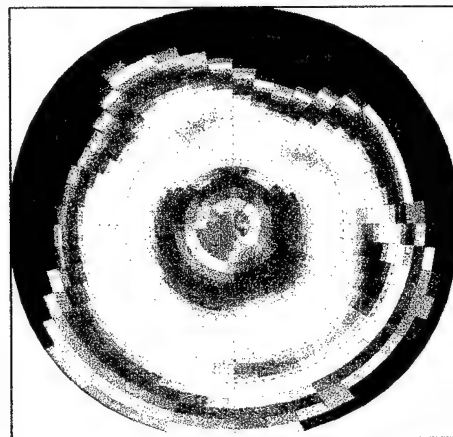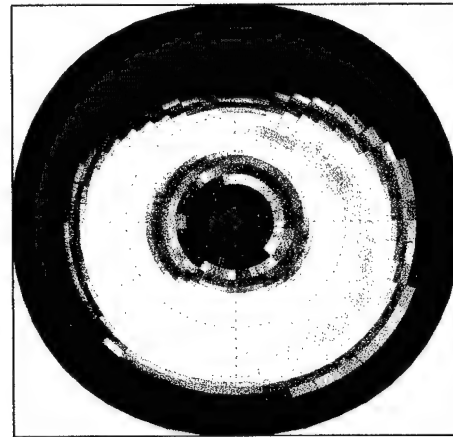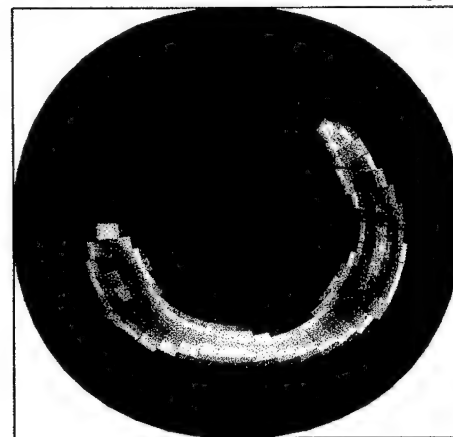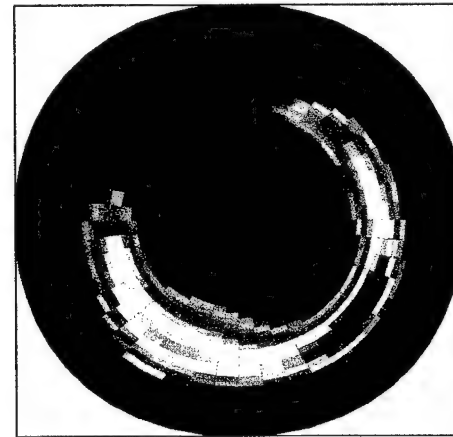
**Plate 1.** Comparison of the original auroral oval model published in 1987 (left) with the improved AFSAM model for Electron Energy and Number Flux and Hall Conductivity.
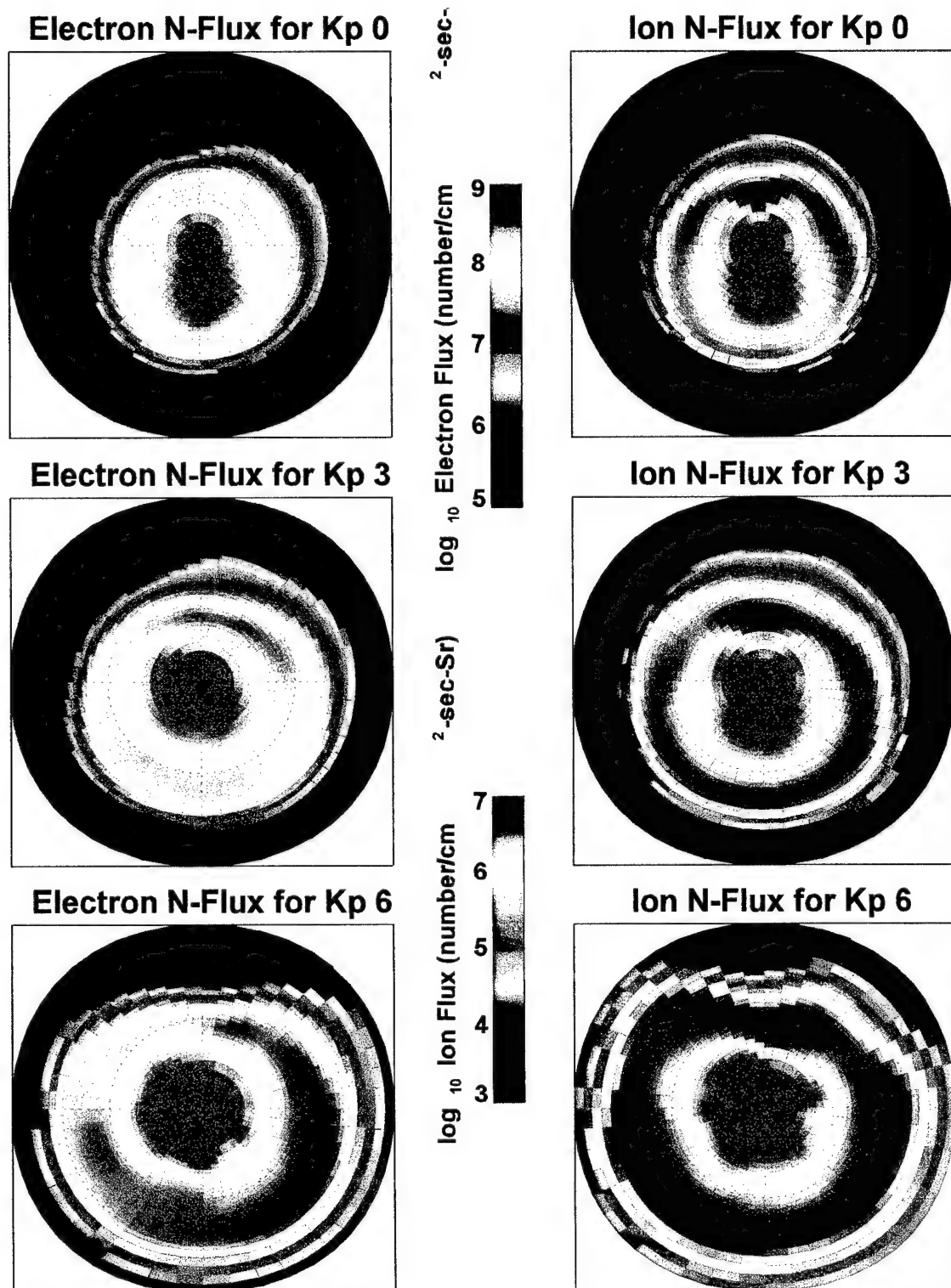
**Plate 2.** Electron and Ion Number Flux at three different $K_p$ levels, showing the intensification and expansion of the auroral oval.
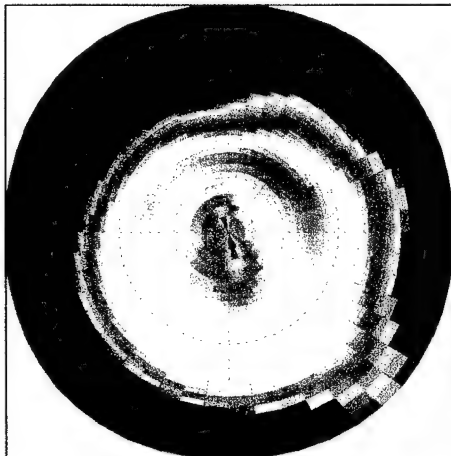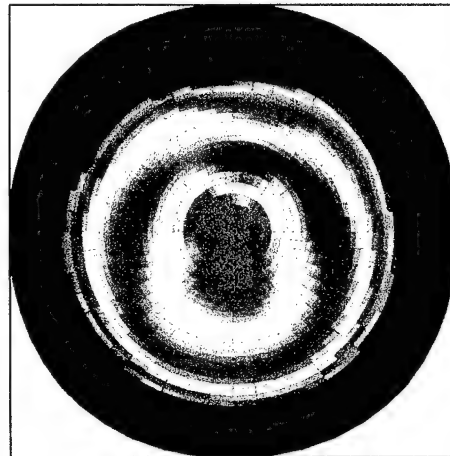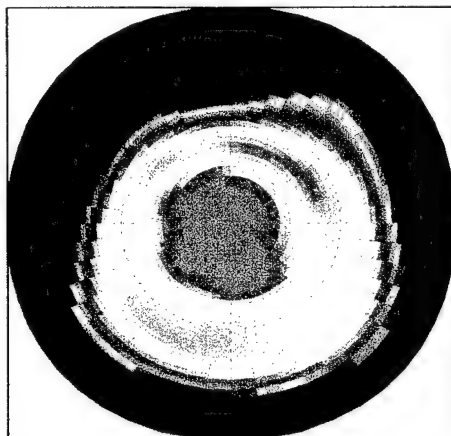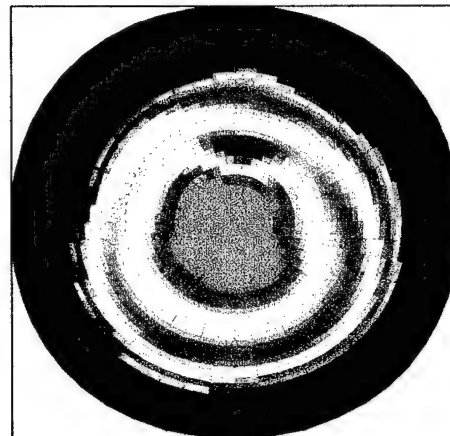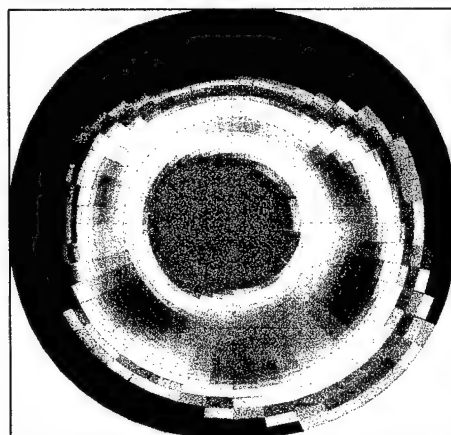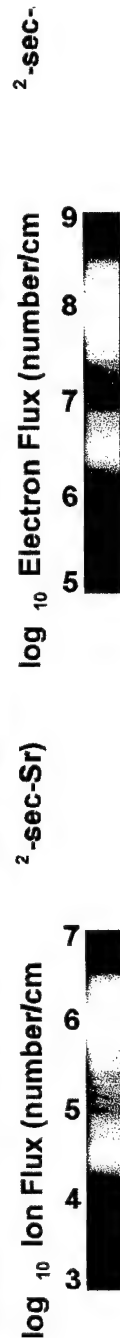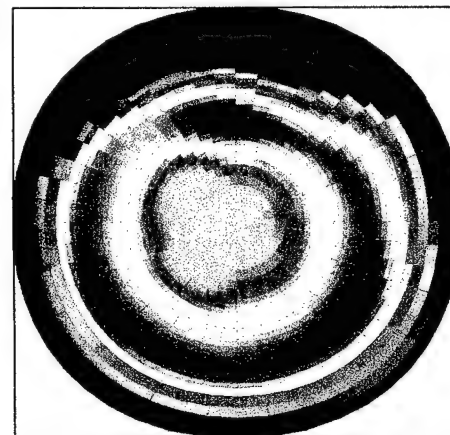
**Plate 3.** Electron and Ion Number Flux at fixed solar wind speed of 485 km/sec, showing the variability of the oval with the direction and magnitude of $B_z$.

5
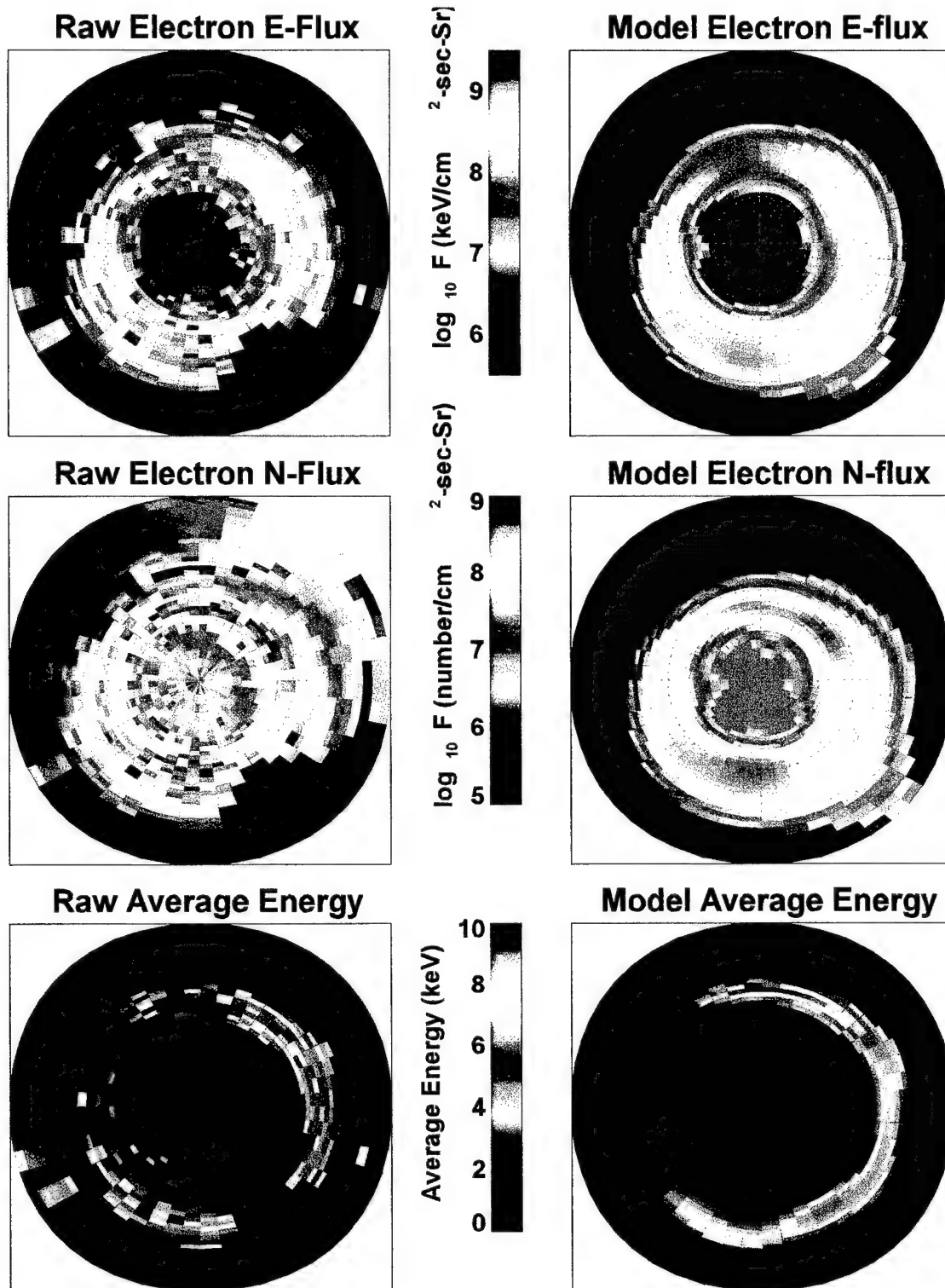
**Plate 4.** Comparison of the raw data (left) with the model results (right) for Electron Number and Energy Flux and Average Energy at SWS of 485 km/sec and $B_z$ of -4.5.

6

# 1. Introduction

The Defense Meteorological Satellite Program (DMSP) has been collecting space and tropospheric weather data for U.S. military operations for more than two decades. From 850 km dawn/dusk or noon/midnight orbits, each of these satellites pass over the polar regions thirty-two times per day, continuously monitoring polar electric and magnetic fields and measuring electron and ion precipitation. These data are employed in the assessment of space weather conditions and in the forecasting of geomagnetic and auroral activity for both military and commercial applications.

Because of the long history of the program, a large data base of auroral precipitation measurements has been amassed. This data base has been used to derive a number of statistical models of auroral flux and related properties. In early studies, Hardy *et al.* [1985] computed average auroral electron precipitation characteristics, ordering the data by magnetic local time, corrected geomagnetic latitude and the geophysical activity index $K_p$, using data from the DMSP/F2 and /F4 satellites. In addition to providing considerable insight into the structure of the diffuse aurora, these studies resulted in useful maps with which the regions and magnitude of electron precipitation could be estimated at varying levels of activity.

In order to make the use of these maps more convenient for a variety of applications, these data were fit to functional forms [*Hardy et al.*, 1987] through which each map of 1,440 discrete values was expressed as 52 coefficients of continuous functions. In addition to reducing the storage requirements, the functional modeling provided smoothing of the discrete maps and continuity between adjacent points, important for incorporation of the models into more elaborate theoretical modeling programs. In addition to the electron energy and number flux presented by Hardy *et al.* [1985] the Hall and Pedersen conductivities in the auroral region were computed from the raw maps and were modelled in the same manner. Specific techniques for data processing and for the computation of the auroral properties from the measured spectra, as well as details of the fitting process, are available in the references above. The success of this model led naturally to the application of the same technique to auroral ions [*Hardy et al.*, 1989, 1991]. Again here, maps of ion energy and number flux were generated at specified levels of $K_p$ and were fit to functional forms to provide smoothing and continuity.

Later, Brautigam *et al.* [1991] extended the statistical investigation of auroral morphology by ordering the maps in various combinations of the $z$ component of the interplanetary magnetic field (IMF $B_z$) and the solar wind velocity ($V_{sw}$) instead of by $K_p$. This work resulted in a total of 30 maps at six characteristic values of $B_z$ and five values of $V_{sw}$. These results allowed for the estimation of auroral properties based directly on the forces driving auroral precipitation rather than on the overall level of geomagnetic activity.

7

Naturally, it seemed desirable to represent these maps in terms of functional forms, as had been successfully done with the $K_p$ maps. Due to the rather large number of maps, 240 in all compared to 14 for the $K_p$ ion maps and 28 for the $K_p$ electron maps, some special techniques were required in the fitting. Also in this work, the average energy patterns for both electron and ion precipitation were included in the fitting, while these were not included as part of the original $K_p$ models. For current users of these models, here denoted by the "$K_p$ Models" as opposed to the models as functions of IMF and Solar Wind Speed ("IMF/SW Models"), it should be noted as well that the functional form for the electron fluxes of the present model differs from the model given in Hardy *et al*. [1987] in that more coefficients were used, accounting for the fact that the latitudinal dependence of the electron fluxes appears somewhat broader when distributed over IMF and SW than it did when binned by $K_p$. There are also some subtleties concerning the limiting values assumed for the fluxes toward the poles and toward the equator, which are different from the $K_p$ models and which will be enumerated in what follows.

Also, in the years following the release of the original $K_p$ electron model, the calculations have been repeated using a substantially larger data set. Improved maps of the electron energy and number flux, as functions of $K_p$, and of the conductivities have been thereby obtained. The previously published ion fluxes were derived from this same expanded data set. Therefore, the electron models of Hardy *et al*. [1987] and the ion models of Hardy *et al*. [1991] were inconsistent in the data base from which they were derived. These $K_p$ electron maps have been refit using the techniques developed for the IMF/SW models and are incorporated into the current model, thereby arriving at a self–consistent set of models. We recommend that the current formulation replace the electron Hardy *et al*. [1987] electron flux and conductivity model in all applications because the data set is more comprehensive and because the functional form is a somewhat better representation of the profiles in some cases. Also, the current models include average energy for both ions and electrons, which the previous models do not. The ion flux model presented here is identical to the Hardy *et al*. [1991] model.

The complete model, described here, includes electron and ion energy and number flux, electron and ion average energy, and Hall and Pedersen conductivities, all as functions of both $K_p$ and as functions of various combinations of IMF and Solar Wind Speed. Collectively, we call these the Air Force Statistical Auroral Models (AFSAM) [*Brautigam et al*., 1998]. The models themselves are functional representations of statistically determined averages, each "map" being a function of magnetic local time (MLT) and of corrected geomagnetic (CGM) latitude [*Bhavnani and Vancour*, 1991]. Since the development of AFSAM has proceeded in "fits and starts" over a period of some years, and since interim products have been released, it is perhaps helpful to review the chronology of this development, which is shown in Table 1. Note that the current model is intended to replace any currently in circulation.

8

| TABLE 1. Chronology of AFSAM Development | |
|---|---|
| Calculation of Average Electron Flux Kp Patterns | Hardy *et al.* [1985] |
| Calculation of Conductivities and Generation of the Original Electron Flux and Conductivity Kp Model | Hardy *et al.* [1987] |
| Calculation of Average Ion Flux Kp Patterns | Hardy *et al.* [1989] |
| Generation of the Ion Flux Kp Model | Hardy *et al.* [1991] |
| Calculation of Properties binned by IMF and SWS | Brautigam *et al.* [1991] |
| Calculation of Improved Electron $K_p$ Patterns | unpublished |
| Completion of AFSAM Model System | this work |

It is worth noting too, since this is the first publication concerning these models in quite some time, that up-to-date versions of all the functional fits are available through Dr. Don Brautigam, AFRL/VSBS, 29 Randolph Road, Hanscom AFB, MA 01731. In the interest of the current trend toward conciseness in published AF material, we will not reproduce all the coefficients of all the models, since these are available much more expediently through electronic means. We will also not attempt to show the behavior in every circumstance, but rather will present representative cases of each function. With the large amount of data contained here, such comparisons would perhaps be more confusing. Complete sets of plots, including color images, can be made available on an individual basis, should the need arise.

The primary purpose of this report is to document the process by which these models were generated and to provide users with some measure of the adequacy with which the functional fits represent the data itself. Data, here, means the discrete values of the auroral properties generated from the average spectra and any analysis here will be limited to issues concerning the functional representation of these data. Issues concerning the generation and analysis of the maps themselves have been examined in detail in earlier work [*Brautigam et al.* [1991], Hardy *et al.* [1985;1987;1991].

We begin with a brief description of the data set, which is necessary to appreciate the modeling task. This is followed by a description of the various auroral quantities represented in the model; integral energy flux, integral number flux and average energies, for both ions and electrons, and the Pedersen and Hall conductivities. Because the number of maps in this model is so large, we limit consideration to six which are representative of the total of 30 cases for IMF/SWS, or 7 for $K_p$, for each property. Finally, we will briefly describe the software through which the statistical maps of the averaged auroral quantities are analytically modeled.

## 2. The Data

The IMF/SWS maps were generated from a total of 33 million spectra constituting over 13,000 hours of observation by the SSJ/4 electron and ion detectors aboard DMSP/F6 and /F7 satellites. Time periods are 1983 January to 1987 July for /F6 and 1983 December to 1987 July for /F7. DMSP/F6 was in a dawn/dusk orbit while /F7 orbited in the noon/midnight plane. The resulting coverage was quite good, with a characteristic bite-out at local 1500 hours extending northward to only about 60° magnetic and a slightly larger bite-out at local 0230 hours which left the a gap between 60° and 70° of about 2 hours of local time. The detailed coverage is shown in Figure 1 of Brautigam *et al.* [1991]. Bite-outs, although not terribly severe in this data set, were dealt with by interpolation in various ways for various maps and details will be given in the next section.

| TABLE 2. Parameter Ranges and Coverage of the IMF/SWS Maps | | | | | | | |
|---|---|---|---|---|---|---|---|
| Map | # Hours | $B_z$ | $V_{sw}$ | Map | # Hours | $B_z$ | $V_{sw}$ |
| 1 | 290 | -4.5 | 346 | 16 | 653 | +0.7 | 484 |
| 2 | 405 | -2.2 | 346 | 17 | 421 | +2.1 | 487 |
| 3 | 780 | -0.7 | 345 | 18 | 348 | +4.7 | 486 |
| 4 | 811 | +0.7 | 345 | 19 | 197 | -4.7 | 569 |
| 5 | 501 | +2.1 | 347 | 20 | 255 | -2.3 | 573 |
| 6 | 360 | +4.5 | 349 | 21 | 427 | -0.7 | 572 |
| 7 | 441 | -4.9 | 408 | 22 | 502 | +0.7 | 573 |
| 8 | 532 | -2.2 | 409 | 23 | 410 | +2.1 | 571 |
| 9 | 923 | -0.8 | 408 | 24 | 284 | +4.4 | 572 |
| 10 | 1,007 | +0.7 | 409 | 25 | 71 | -4.4 | 668 |
| 11 | 697 | +2.1 | 408 | 26 | 149 | -2.2 | 675 |
| 12 | 562 | +4.6 | 407 | 27 | 256 | -0.8 | 679 |
| 13 | 311 | -5.0 | 485 | 28 | 368 | +0.7 | 679 |
| 14 | 332 | -2.2 | 485 | 29 | 261 | +2.2 | 675 |
| 15 | 553 | -0.7 | 484 | 30 | 156 | +4.3 | 677 |
|  |  | nT | km/s |  |  | nT | km/s |

Table 2, shows the correspondence of the maps to various ranges of IMF $B_z$ and $V_{sw}$. Note that the divisions are not precisely uniform, but represent quite well six different values of $B_z$ at five values of SWS. The values in the table represent the actual average values of the data points included in the various bins. Also shown is the total number of hours of data available for each map. One can readily appreciate the difficulty of preserving adequate statistics while providing a uniform range of $B_z$ and $V_{sw}$. This task was accomplished quite well by Brautigam *et al.* [1991], however, it should be apparent from the table that some of the maps comprise far fewer samples than others. This is an inevitable result of the process and was true for the $K_p$ models as well, with the higher $K_p$ maps constituting significantly less data than the lower ones.
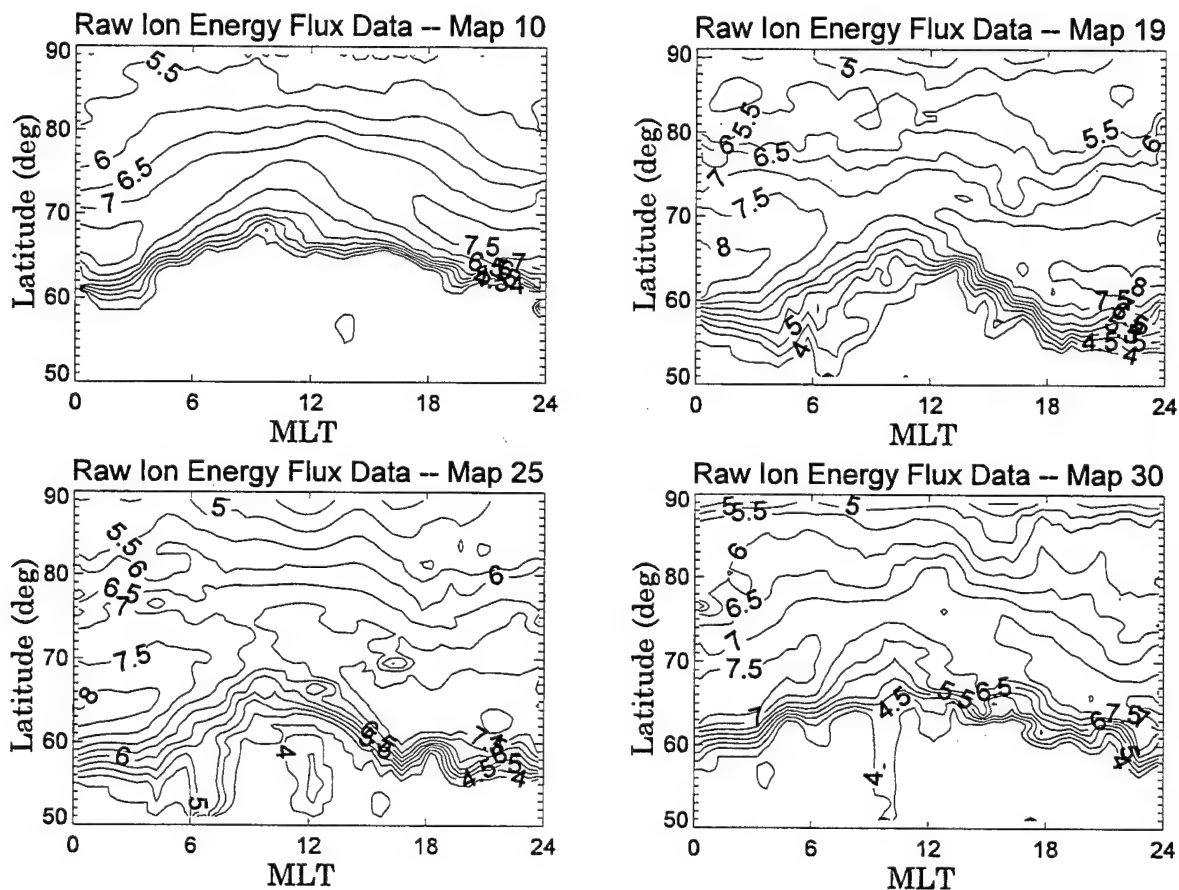


**Figure 1.** Contours of $\log_{10}$ Raw Ion Energy Flux (in keV-cm$^{-2}$-s$^{-1}$-Sr$^{-1}$) for the Most Populated Map (Map 10) and for the Three Least Populated Maps in the IMF/SWS Model.

Figure 1 shows contours of the ion energy flux from Map 10, the map with the best statistics, and the three maps with the worst statistics. The data in Figure 1 has been filled in over the bite-out regions and has been subjected to a 3x3 point smoothing in

magnetic local time ($x$ axis) and in corrected geomagnetic latitude ($y$ axis). We see that there are a few areas in the lesser populated maps where bins have not been adequately sampled, leading to spikes in the average quantities. We also see evidence of a few contaminated passes, leading to high flux values equatorward of the aurora. These spurious features will be removed in the fitting process. In spite of them, though, the patterns in the maps are quite clear, even for those maps with the poorest statistics. We might note that contour plots are an unflattering way to present this raw data and that color plots would emphasize the coherency of the maps, rather than bringing out the noise. We will elaborate on the processes carried out on maps with poorer statistics on a case-by-case basis. Here, we simply state that it has proven possible in all maps and for all quantities to produce smooth models which represent the binned data very well.

The $K_p$ versions of the maps contain fewer total spectra, about 25 million all together. However, since there are only seven different maps in this set, the statistics are roughly comparable. The data was accumulated over the full year of 1983 for F6 and the full year of 1994 for F7. Table 3 gives the range of $K_p$ represented as well as the number of hours in each bin.

| TABLE 3. Parameter Range and Coverage of the $K_p$ Maps | | | | | |
|---|---|---|---|---|---|
| Map | $K_p$ | Hours | Map | $K_p$ | Hours |
| 1 | 0,0+ | 225 | 5 | 4−,4,4+ | 1330 |
| 2 | 1−,1,1+ | 1020 | 6 | 5−,5,5+ | 610 |
| 3 | 2−,2,2+ | 1831 | 7 | ≥6 | 233 |
| 4 | 3−,3,3+ | 1885 | Total | --- | 7134 |

The raw data for the $K_p$ maps looks quite similar to that of the IMF/SWS maps. Representative cases of the electron energy flux are shown in Figure 2. Again, these maps have been filled in over the low latitude gaps caused by lack of DMSP coverage and have been run through a 3–point smoothing. We show, as before, the statistically most significant map, Map 4, along with the three statistically worst. As in the IMF/SWS maps, it is clear that the overall patterns are clear. However, there are some problems, especially in filling in the bite–out region below 75–degrees around 0300 MLT. Because of this, this region was filled in by hand, to be discussed in the next section. Figure 3 shows the corresponding average energy maps. Clearly, the average energy looks considerably different from the fluxes, although the problem with bite–out remains. The average energies were also hand edited and were fit to entirely different forms than were the fluxes.

Each map consists of 1,440 values of energy flux, number flux, average energy or conductivity spanning the corrected geomagnetic latitude range from 50° to 90°. There are 30 latitude bins with a spacing of 2° between 50° and 60° and between 80° and 90° with 1° spacing between 60° and 80°. The northern and southern aurora are combined, since there has been no evidence for significant differences. The magnetic local time (MLT) is divided into 48 even half-hour bins. The quantities themselves are computed from averaged ion and electron spectra which have been extrapolated to high energy, as described in Hardy *et al*. [1989]. The computation of the fluxes is outlined in Brautigam *et al*. [1991] and the computation of the conductivities in Hardy *et al*. [1987]. Average energies are computed here as the ratio of the energy flux to the number flux, as derived from the average spectra.
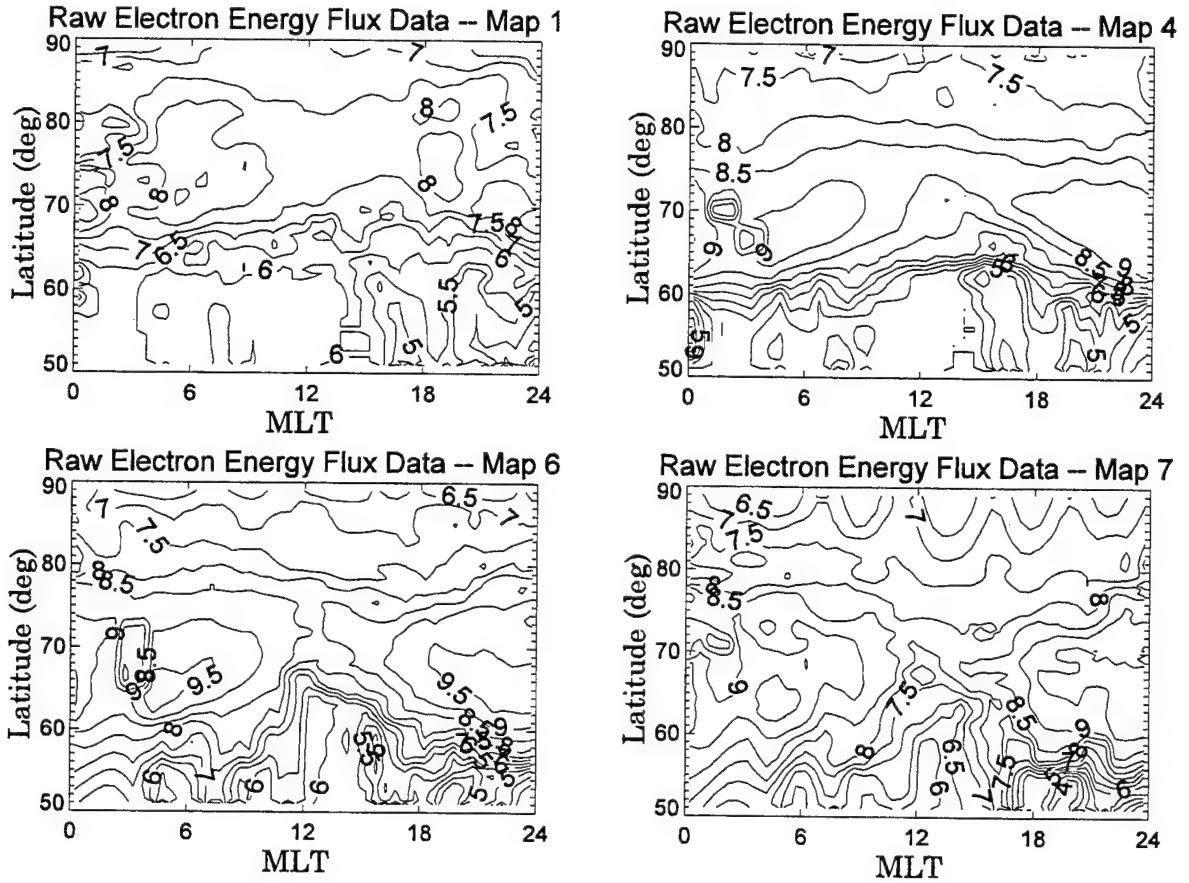


**Figure 2.** Contours of $\log_{10}$ Raw Electron Energy Flux (In keV–cm$^{-2}$–sr$^{-1}$) for the Most Populated $K_p$ Map and the Three Least Populated Ones, According to Total Number of Samples in the $K_p$ Division.

In all, three different analytical forms were used in the fitting, depending on the characteristics of the various properties. The first, used for the integral energy and number flux for the ions and electrons, fit the logarithm of the flux to an Epstein transition function with six coefficients for each map at each value of MLT. The coefficients of these fits represent characteristics of the latitude profile, so that they are

13

reasonably consistent between latitude cuts and therefore can be expanded in a Fourier series in MLT to arrive at a functional form for each map consisting of 78 coefficients. The conductivities are fit in much the same way, except that a four coefficient Epstein function is used due to the less complex latitudinal behavior of the conductivities. The average energies are fit to an altogether different functional form, a combination of a Fourier series and orthogonal polynomials. The difference is due to the different nature of the function as well as from the desire to produce a model with all points of relatively equal accuracy. For fluxes and conductivities, the model will be accurate in the active auroral region, but the model functions will fall to zero outside the aurora. We have included a measured "background" level in the model fluxes on the poleward side. Due to this behavior poleward and equatorward of the main aurora, it is not adequate to represent the average energy as the quotient of the energy and number fluxes, since this leads to large errors near the auroral boundaries. Before moving on to the fitting procedures, we describe some details of the processing done on the raw maps before the fitting could take place.
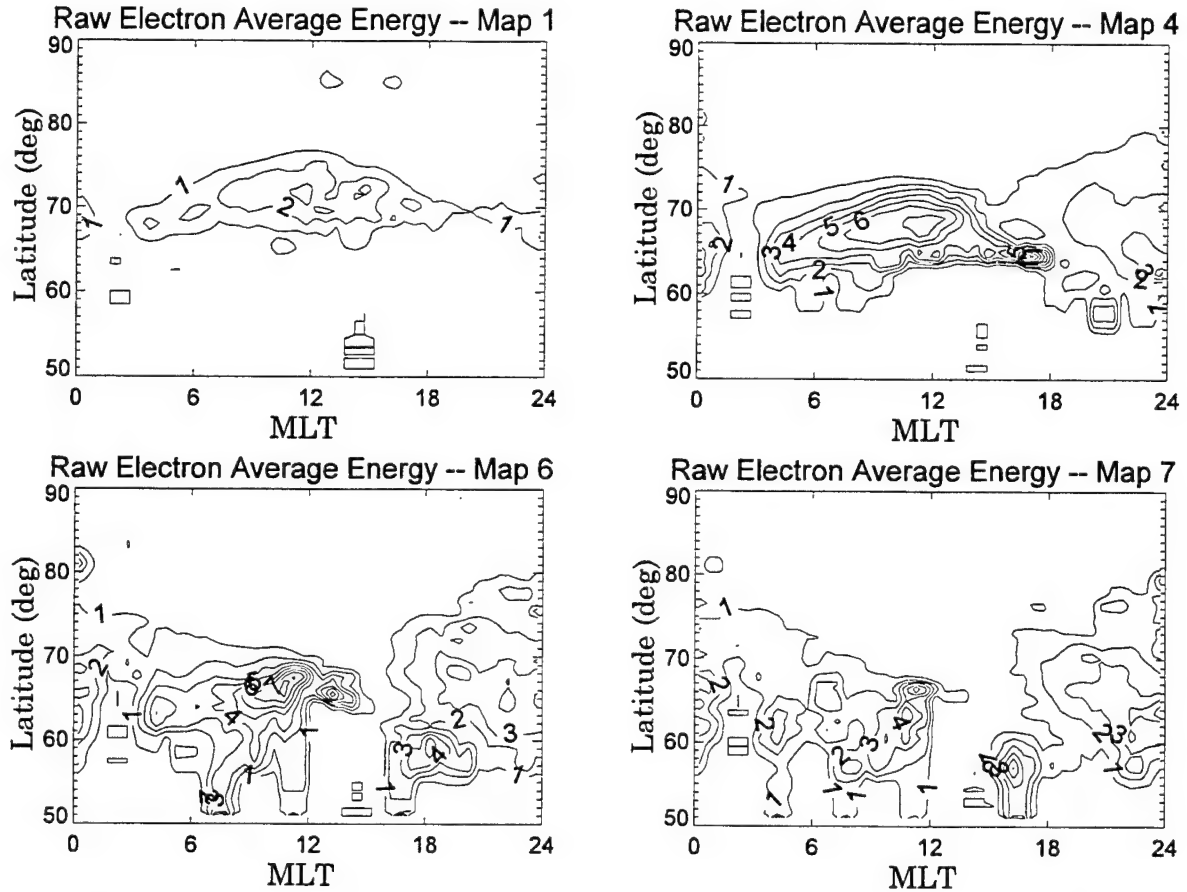


**Figure 3.** Average Energy from Four of the Maps in the $K_p$ Data Set. For these plots, a 3–point smoothing in CG latitude and MLT has been done, but the gaps due to limited coverage, most apparent around 0300 MLT, remain.

14

## 2.1. Data Preparation

There were three different steps taken on all of the maps to prepare them for fitting. These steps differed somewhat for different types of maps, but were carried out to some extent on all types. First, certain regions of the maps needed to be "filled in" since the DMSP coverage of the auroral region was not quite complete. To identify these regions, we have plotted in Figure 4 the number of counts in each CG Latitude and MLT bin for the four maps shown in Figure 1. In the processing, we rejected any CG Latitude and MLT bin with fewer than 100 total counts. Therefore, in Figure 4 we have simply blacked out these regions of the maps.
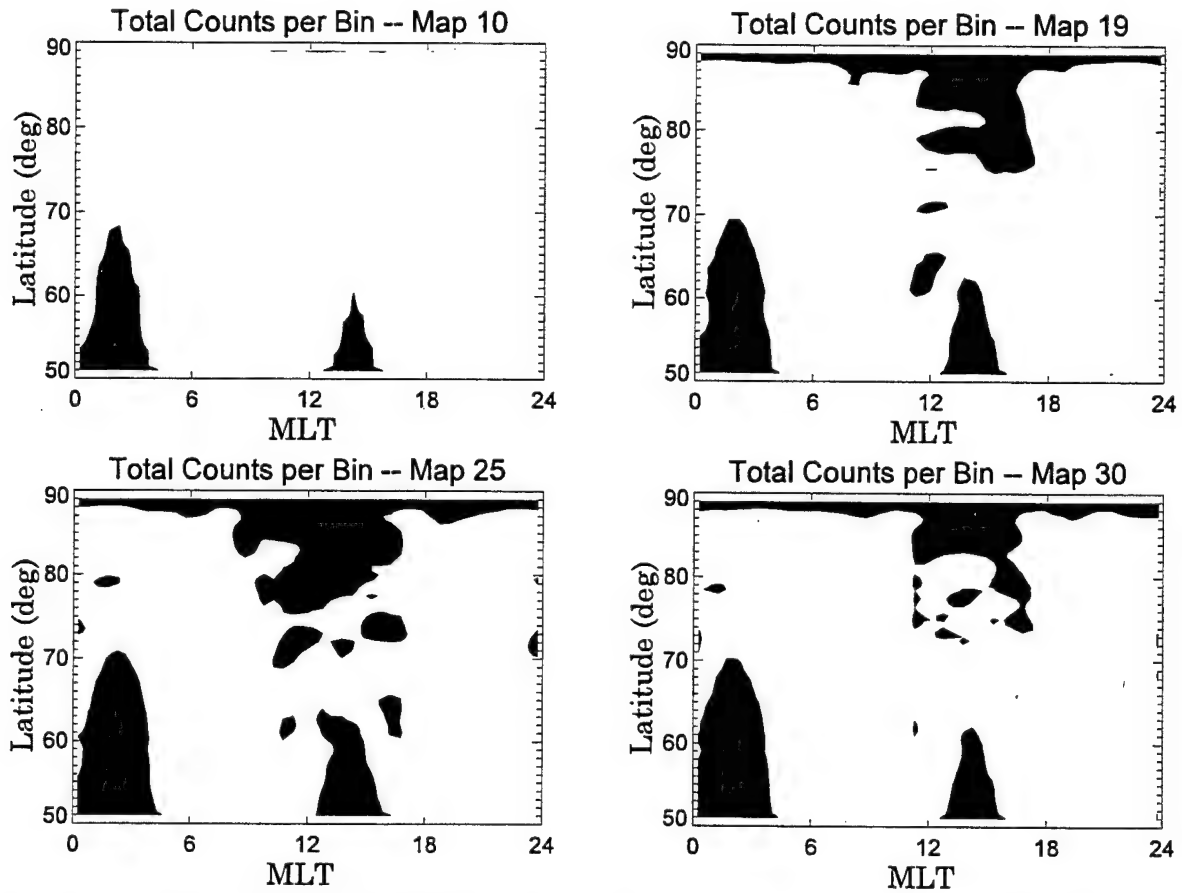


**Figure 4.** The Total Number of Counts per Bin in Four Maps of the IMF/SWS Model. Map 10 has the greatest number of total spectra and Map 25 has the least. The cutoff for using the data was taken as 100 counts. Regions with fewer than 100 spectra in each CL Latitude and MLT bin are blackened.

The regions of no coverage can be seen most clearly in Map 10 between 0000 and 0500 MLT, with a smaller region between 1300 and 1600 MLT. Since the $K_p$ maps have considerably better statistics (Table III) the bite–out regions for these maps are nearly

15

the same as those for Map 10. When a bin contained less than 100 counts, the values of the electron and ion energy and number flux were replaced in one of a few different ways. For the ion fluxes in the $K_p$ maps, this was done by interpolating over MLT from the average of a few points on either side of the bite–out region. For the IMF/SWS flux maps, both electrons and ions, we filled in the missing portions of the maps based on the nearest model map from the $K_p$ series produced earlier [*Hardy et al.*, 1987; 1991]. To find the closest correspondence, we computed the deviation of the values in each IMF/SWS flux map from each of the 7 $K_p$ maps corresponding to the IMF/SWS maps. We selected the $K_p$ map that best corresponded to the IMF/SWS map and replaced the flux values with less than 100 counts with the values from this $K_p$ map. Figure 5 gives an example of a filled in map for the IMF/SWS model ion energy and number flux.
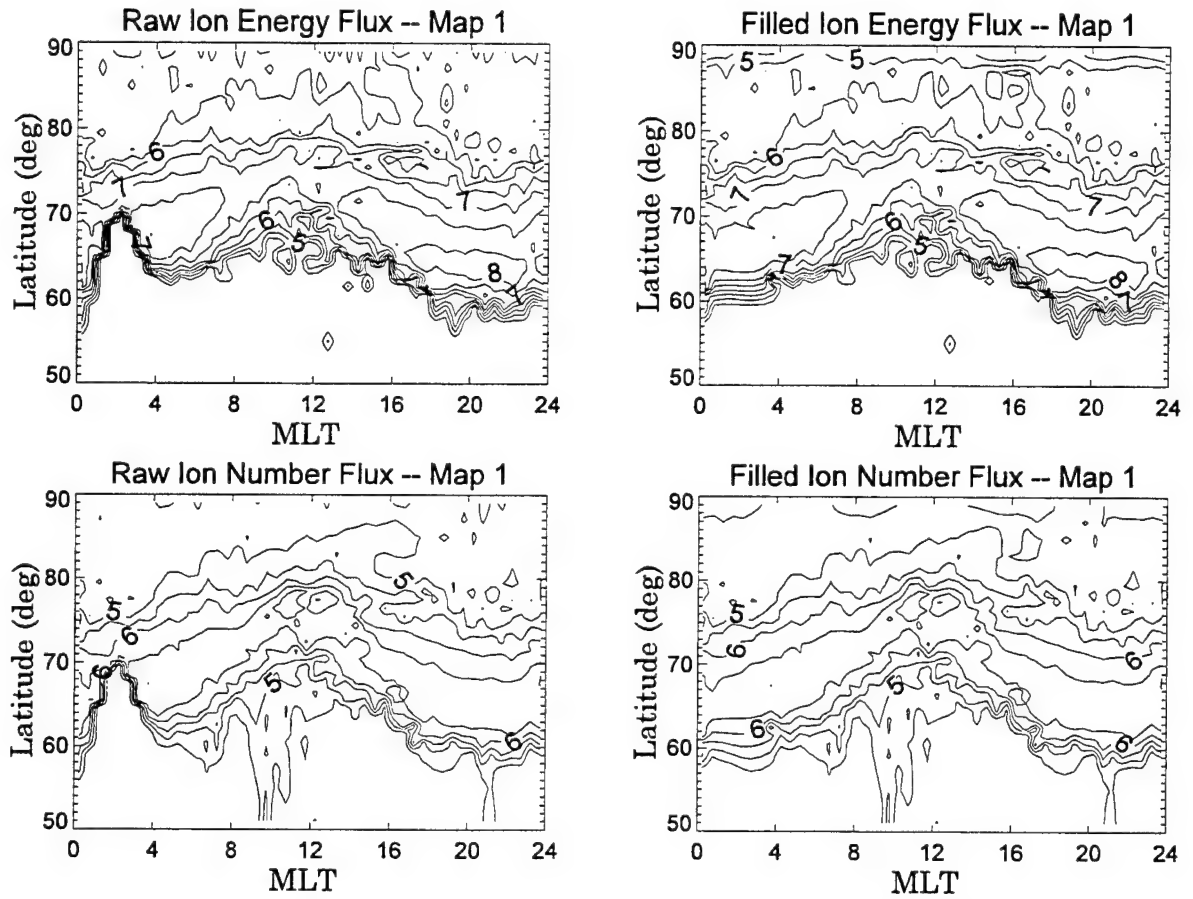


**Figure 5.** An Example of a Raw Data Map (Left Panels) and the Same Map after Filling in Based on the Closest Match to the $K_p$ Flux Models (right) for the Ion Energy Flux (top) and Number Flux (bottom).

The case shown in Figure 5 is quite representative of the results for all the maps, at least for the fluxes. The noon–time bite out region does not significantly affect the flux result, since it is primarily below the boundary of significant precipitation, around 60°

CG Latitude. The post–midnight bite out is in a region of high precipitation, but this is still not a major problem since it is clear from the surrounding data that the pattern extends smoothly through the bite out. This was true for all maps in the data base, as was verified by inspection of plots like Figure 5.

This process was also applied to the Hall and Pedersen conductivities in the IMF/SWS version of the maps. In this case, though, it was found that smoothing of the raw maps prior to filling in gave better results, perhaps because the range of variability in the value of the conductivities is larger, numerically, than for the fluxes. Figure 6 shows Map 1 of the IMF/SWS set for the conductivities.
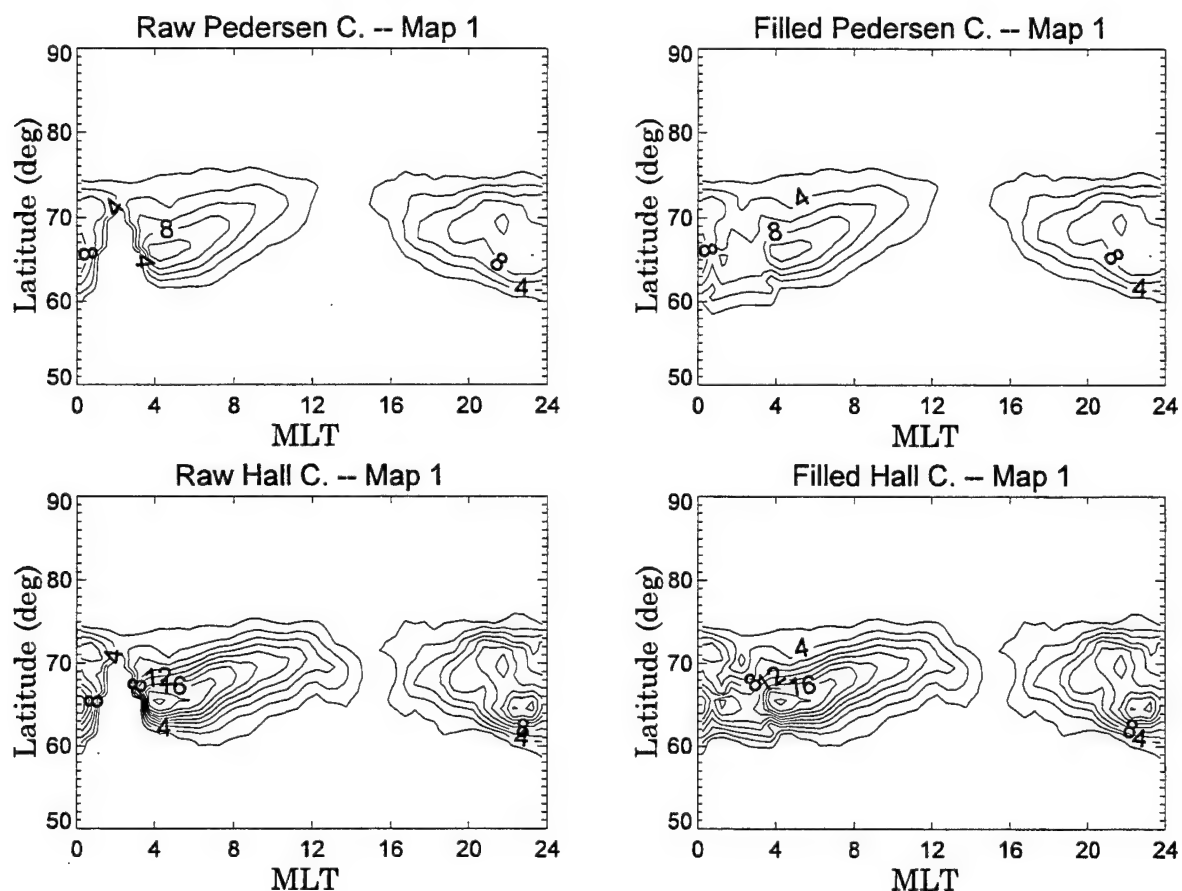


**Figure 6.** The Hall and Pedersen Conductivities for the First of the IMF/SWS Maps Smoothed (left panels) and the Same Maps after the Bite out Regions Were Filled.

It is useful to examine the conductivities, in any case, since these show different maxima as functions of CG Latitude and MLT from either the fluxes or the average energy. Figure 6 shows that the bite out cuts across most of the region of high conductivity in both maps. It is also apparent that the filling in process here does not lead to an entirely satisfactory result. This is not a serious limitation, though, because

17

the natural tendency of the fitting functions is to enforce a slow variation in MLT. Therefore, the minor problems in the filled regions will be corrected for the most part in the fitting. The same is true of the few regions which are not filled, but which exhibit peaks that are somewhat suspicious. One such region is around 62° and 2200 in the Pedersen conductivity in Figure 6. The fit function will give the final result a slowly varying peak CG Latitude as well as peak amplitude. This will become obvious when we discuss the fitting in the next section.

The $K_p$ electron fluxes, the $K_p$ conductivities, and the ion and electron average energies, for both the $K_p$ and the IMF/SWS maps, were filled in through visual inspection using an interactive program written in IDL. With this program, the entire map could be seen at once, with intensity shown by various colors. Places missing data, or places with obviously bad data points were replaced by selecting an appropriate value from other, good points within the map. To see why this was necessary, we show in Figure 7 the raw data from one of the IMF/SWS maps.
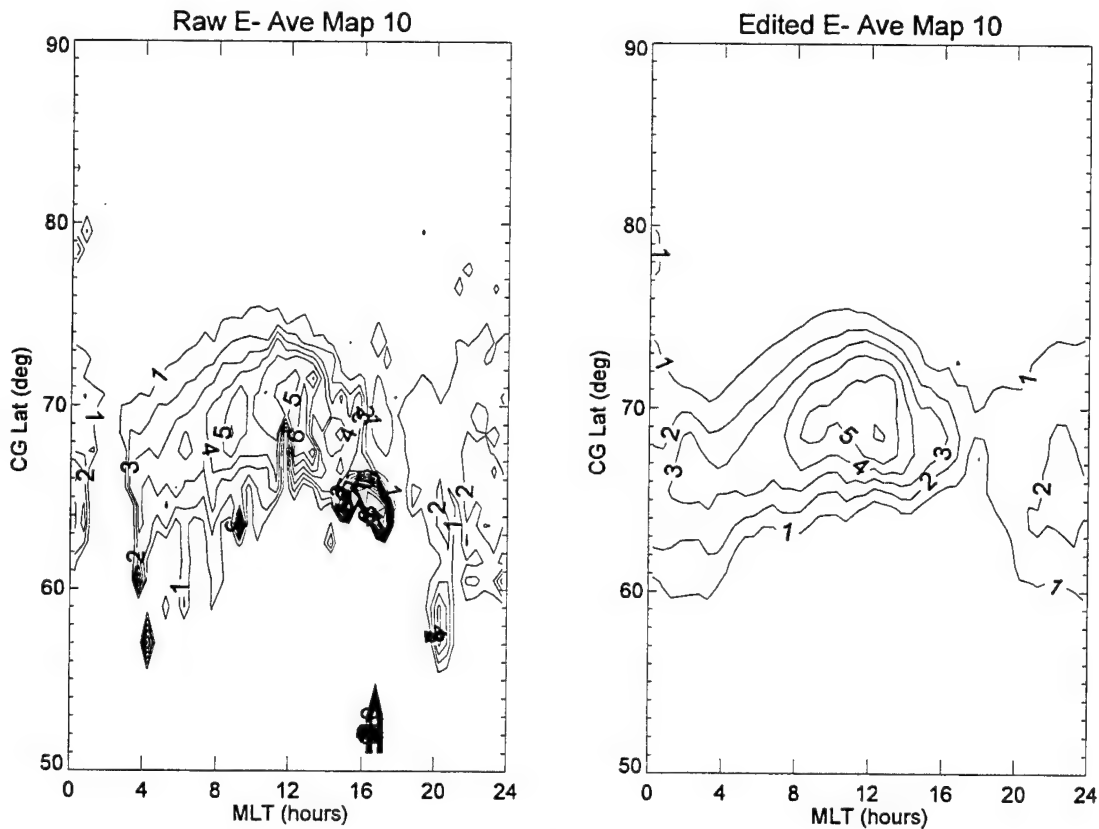


**Figure 7.** The Raw Electron Average Energy (left) from Imf/sws Map 10 and the Edited Version of the Same (right).

18

In addition to the bite out region, it is clear that there are a few regions of noise spikes. This is, in part, due to the nature of the average energy, being the ratio of two fluxes which themselves contain substantial statistical uncertainty. In part, too, it arises in the region of the noon–time bite out, which is the cause of the large values at 1600 MLT in Figure 7. Also, we see regions like the one at 2000 MLT, with high average energy values stretching to low latitudes. These may be from a few contaminated passes, but are apparent in most of the maps.

The most effective way to handle this turned out to be hand editing of all the maps. The case shown in Figure 7 (right) of the edited result is quite representative of the general case, with the end result being free of spurious data yet maintaining very well the patterns that were clearly apparent in the raw data. Having a clean data set prior to fitting is especially important for the average energies since, as we discuss later, these are fit to orthogonal series expansions rather than to functional forms constrained to peak at specific latitudes. This will become clearer in the next section. We should note, too, that the electron average energy maps were by far the most difficult to deal with. The ion average energies were much cleaner, perhaps because the peak tends to be at somewhat higher latitudes or because the ion fluxes naturally vary less. Having said this, it is still obvious that there is some degree of uncertainty, especially in the electron average energy, due to judgments made during the modeling process. Overall, though, the patterns produced by the fit are consistent and make physical sense. It is, again, much better to use the modeled average energies when these are needed, rather than use the ratios of the model fluxes, since the fluxes are not especially accurate away from the peaks.

Once the software for this was written, it was simply easier to use it in further fitting rather than resort to the "batch" filling in developed for the IMF/SWS maps. Therefore, the filling in and editing steps were combined for these quantities. The overall quality does not differ significantly, though. We should also note that a small amount of hand editing was carried out on all the maps. Hand editing was used primarily to remove obviously bad areas, but in no case do we believe this imparted features not obvious in the original data itself.

The final step before fitting was to smooth all the maps over a three–point window in both MLT and CG Latitude. For completeness, and because there are so many different quantities in this model, we present in Figures 8-19 raw, unsmoothed contours of all quantities in the IMF/SWS model, along with smoothed results for the statistically most accurate map, two with average statistics and the one with the fewest total spectra. For the $K_p$ maps we have shown only two, the most and least significant statistically. Note that the $K_p$ maps have better statistics than the IMF/SWS maps. Note, too, that the order of the IMF/SWS maps represents no particular physical progression. We note that contour plots are not the best way to assess the data and that color was used extensively in the processing and analysis.

19
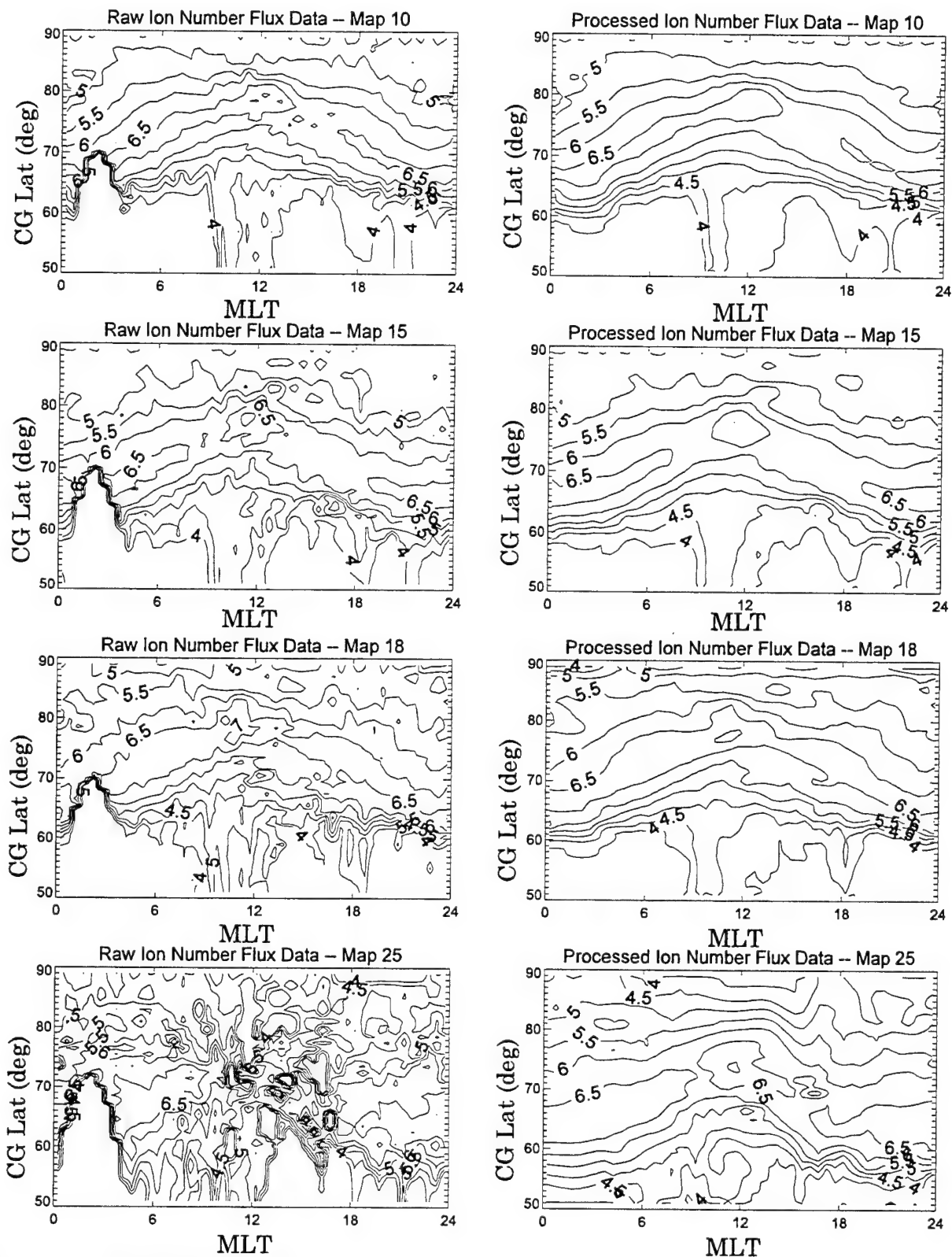
**Figure 8.** IMF/SWS Ion Number Flux Maps. Shown are contours $\log_{10}$ flux in ions/cm$^2$-sec-Sr for the "best" (top), average (middle 4 maps) and "worst" (bottom) statistics.
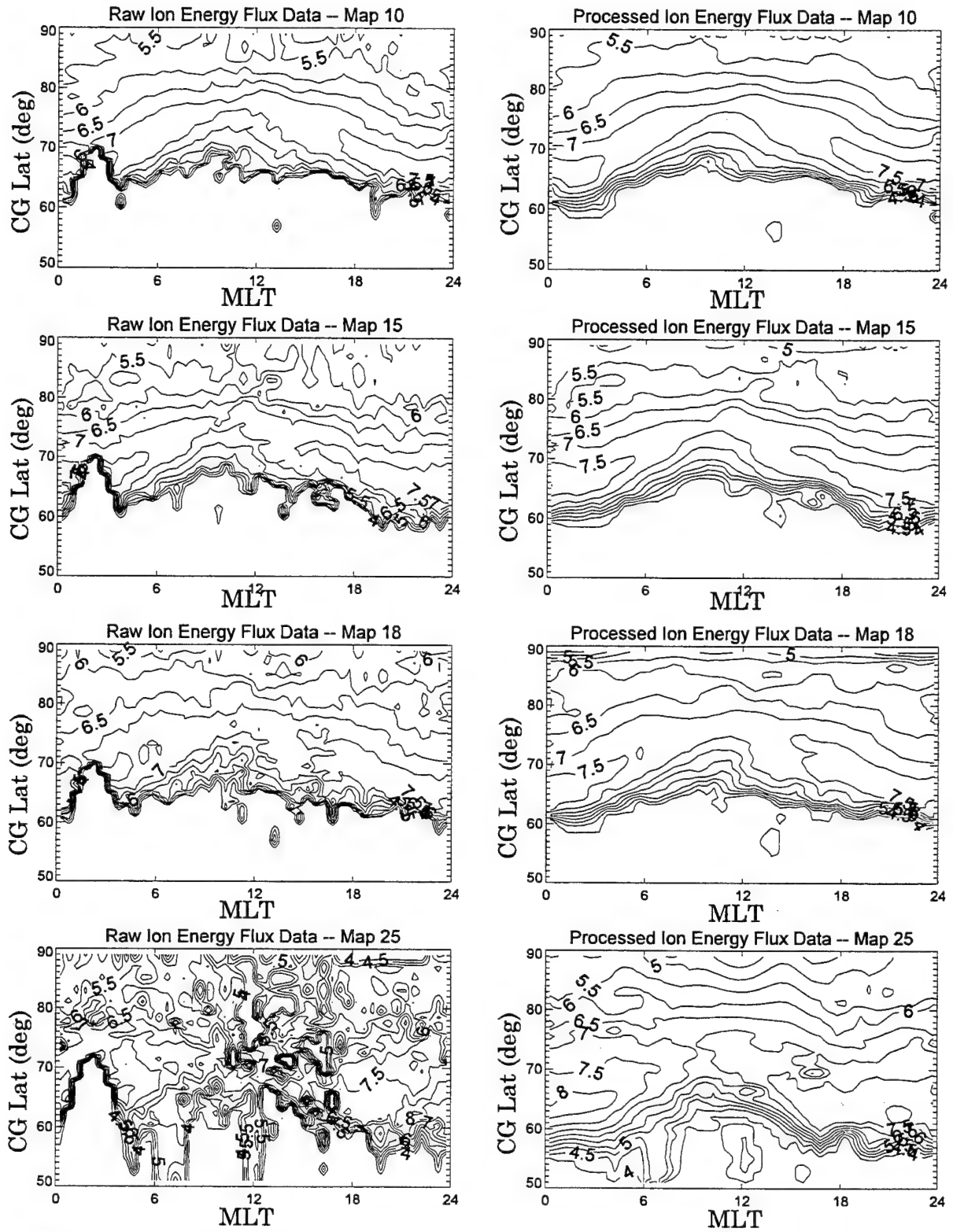
**Figure 9.** Same as Figure 8 Except for the Ion Energy Flux (in keV/cm²–s–Sr).

21
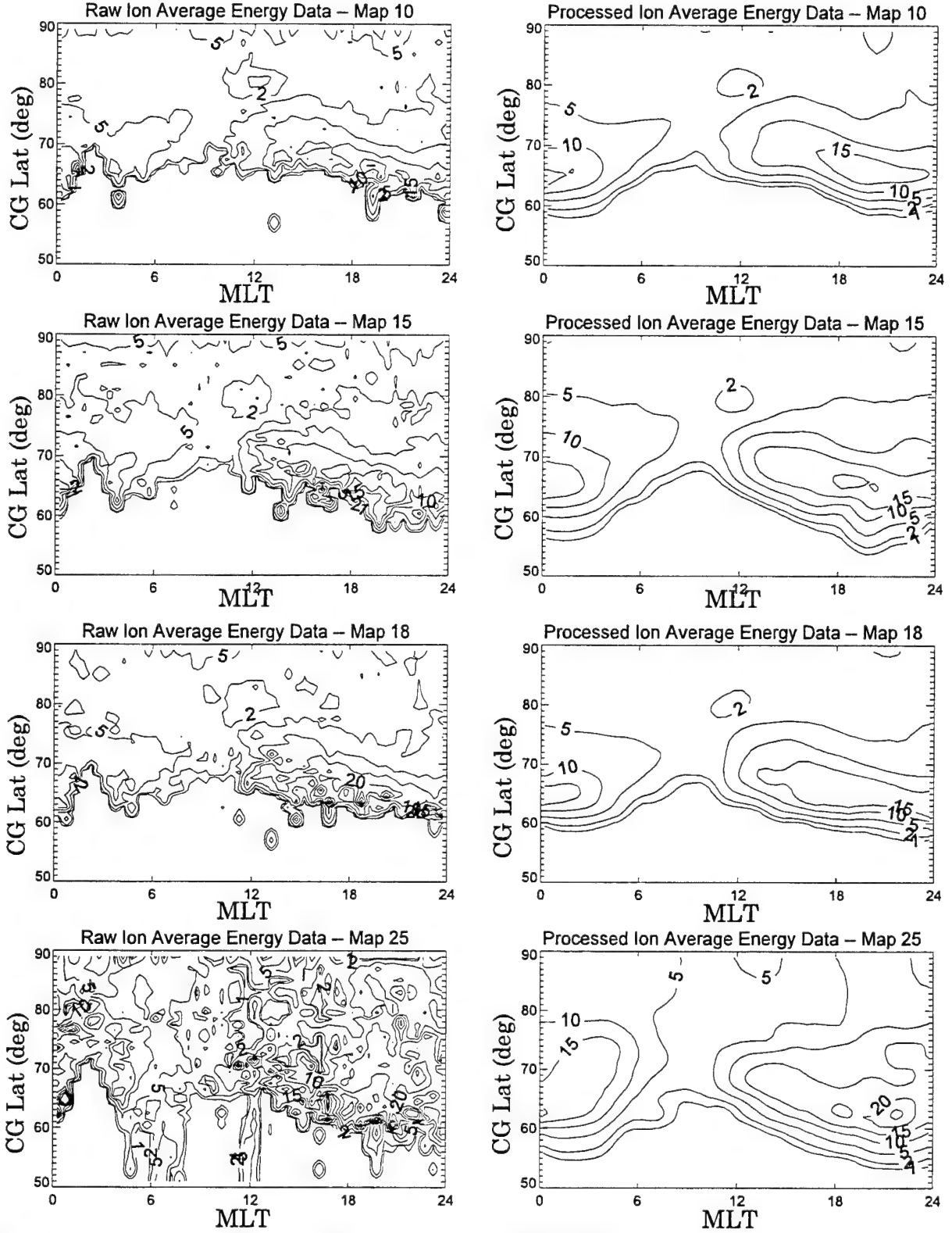
**Figure 10**. Same as Figure 9 Except for the IMF/SWS Ion Average Energy (in keV).
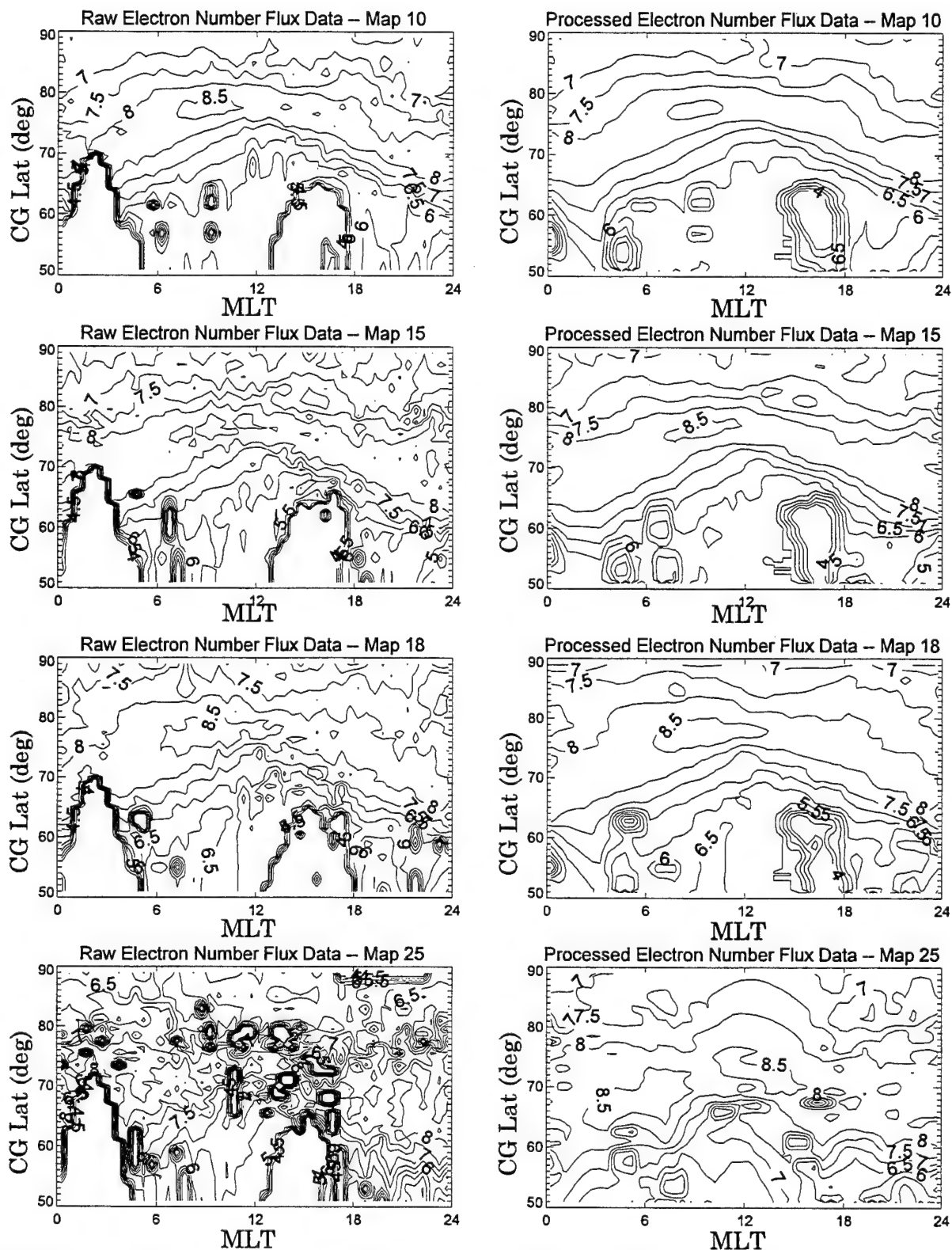
**Figure 11.** Same as Figure 10 Except for the Electron Number Flux (in electrons per cm²–sec–Sr).

23
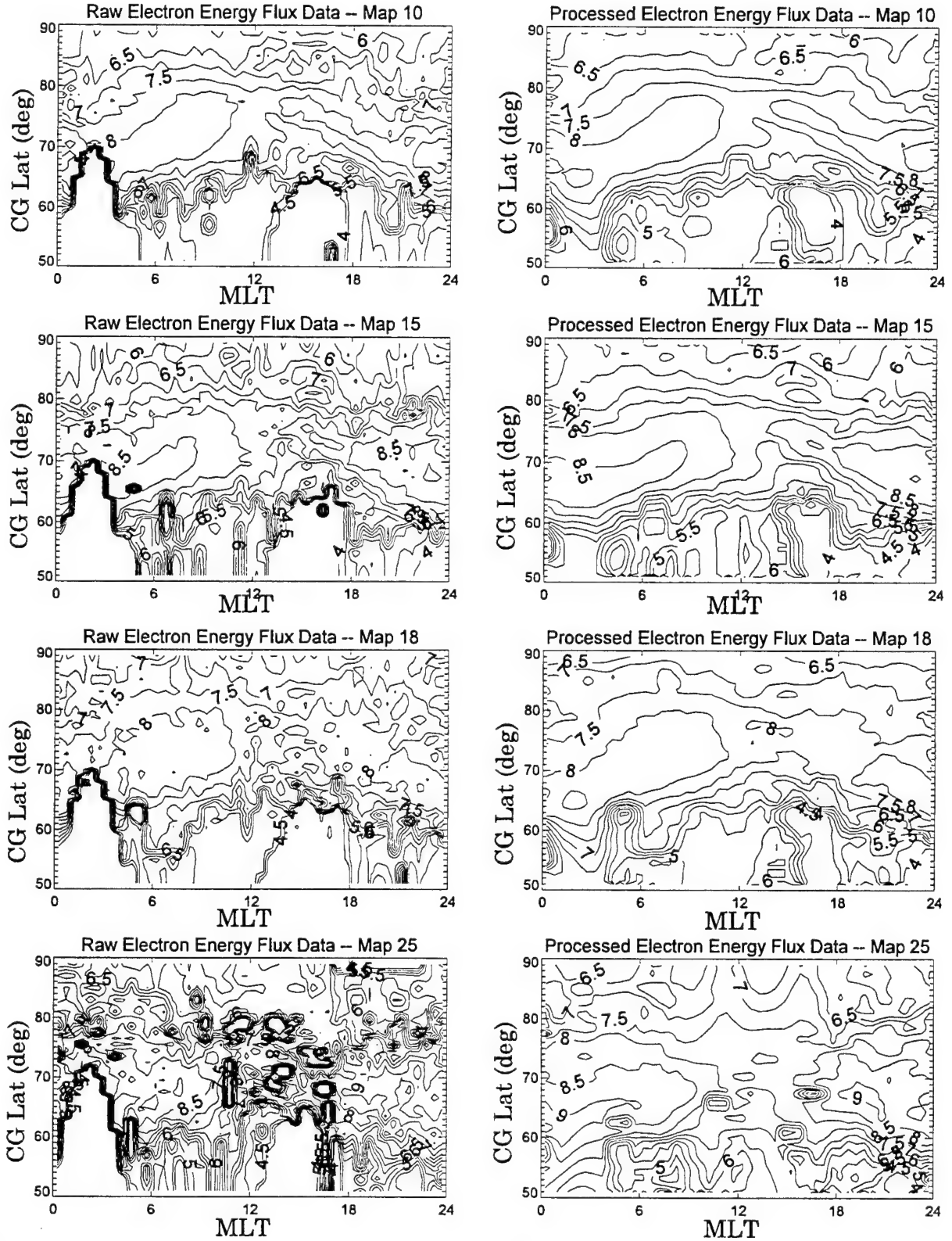
**Figure 12.** Same as Figure 11 Except for the Electron Energy Flux (in keV per cm²–sec–Sr).
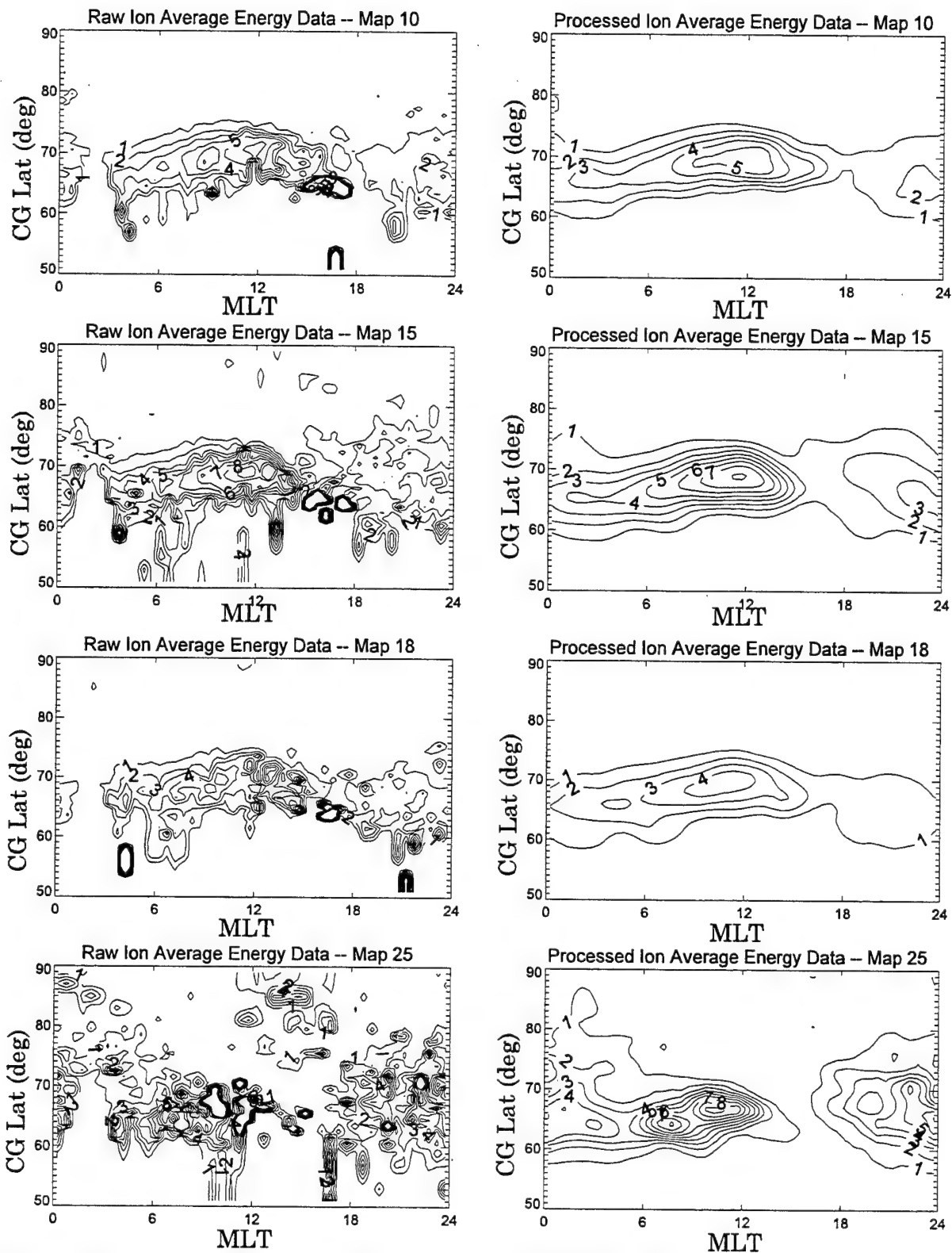
**Figure 13.** Same as Figure 12 Except for the IMF/SWS Electron Average Energy (in keV).

25
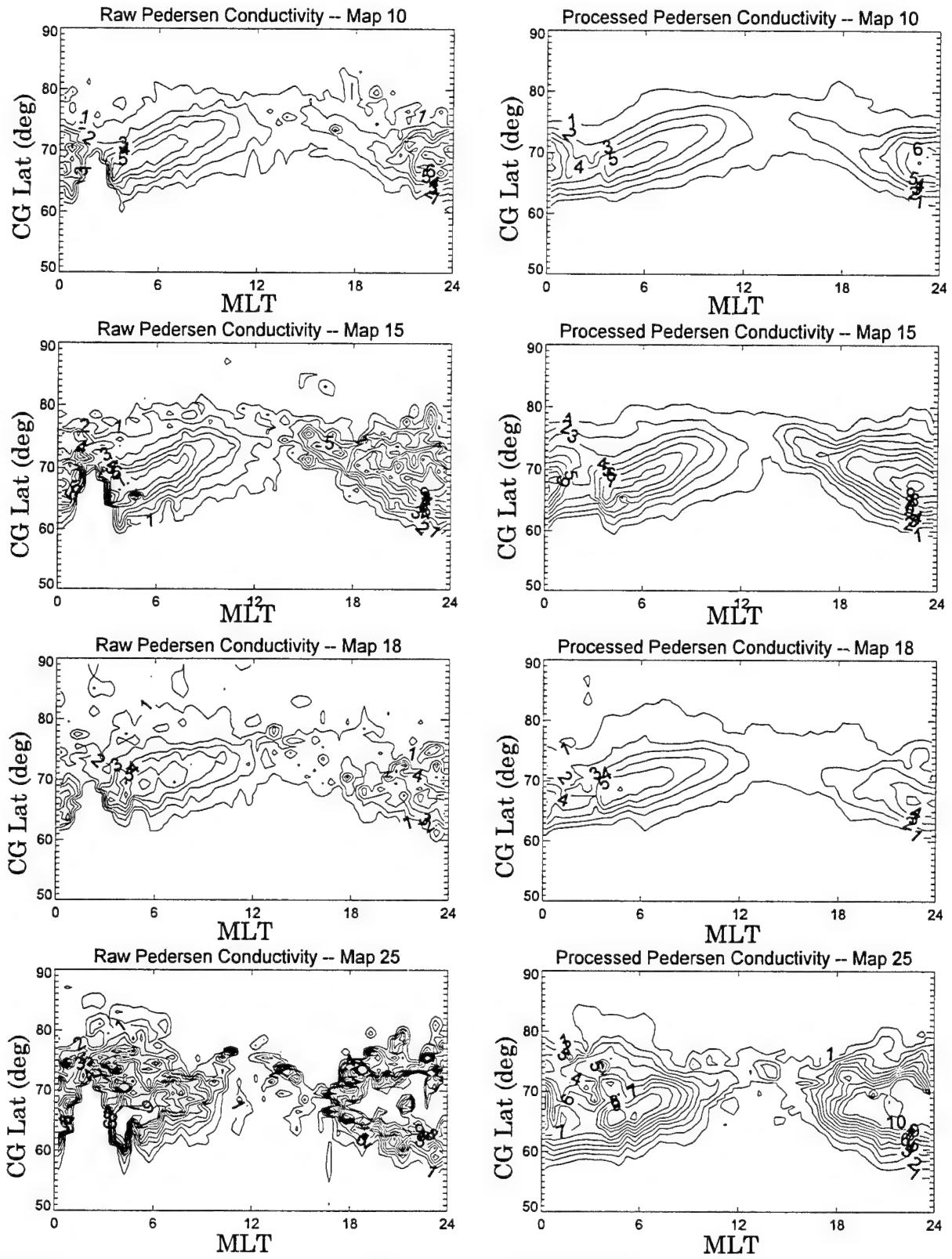
**Figure 14.** Same as Figure 13 Except for the IMF/SWS Pedersen Conductivity (in units of Mhos).
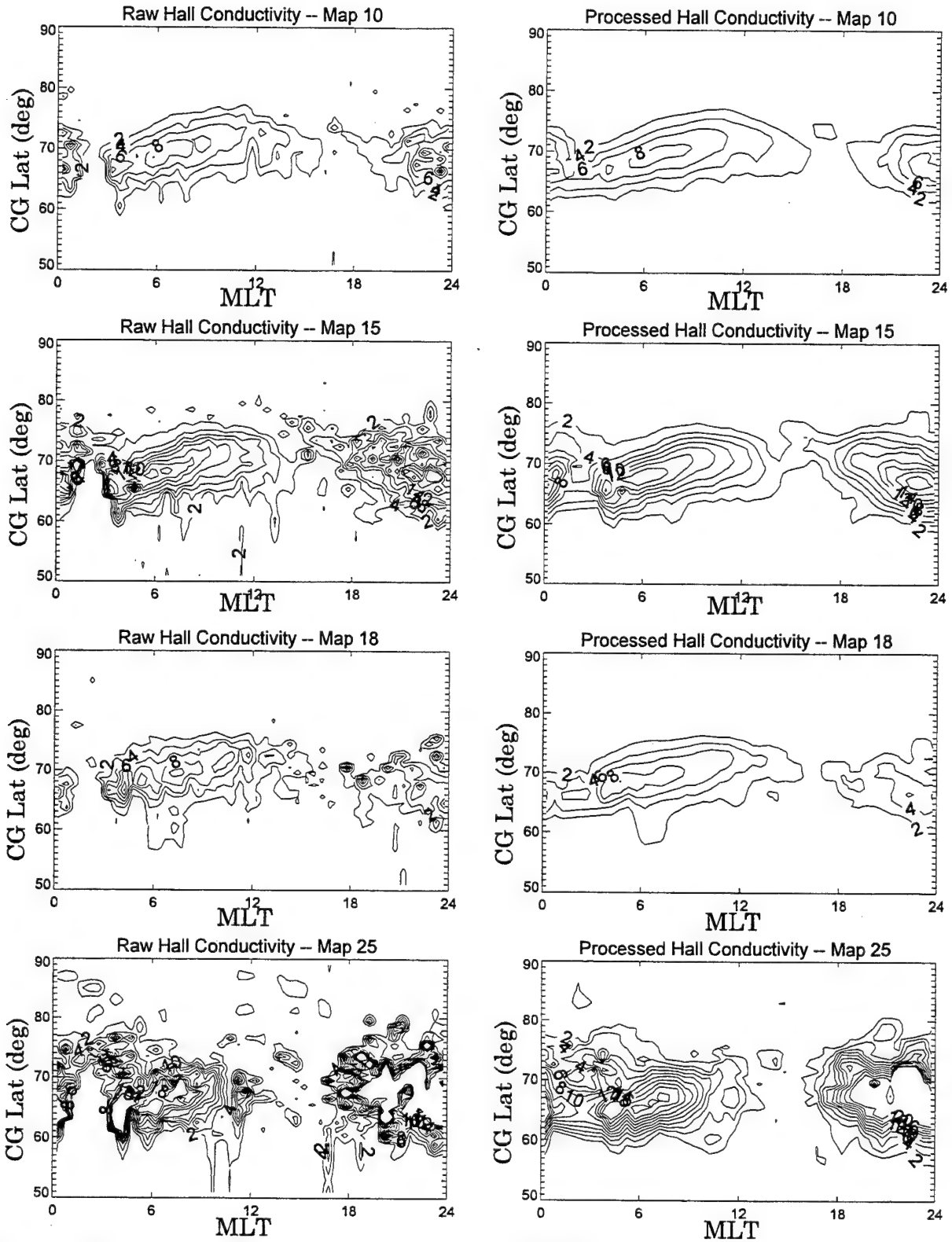
**Figure 15.** Same as Figure 14 Except for the IMF/SWS Hall Conductivity (in Mhos).
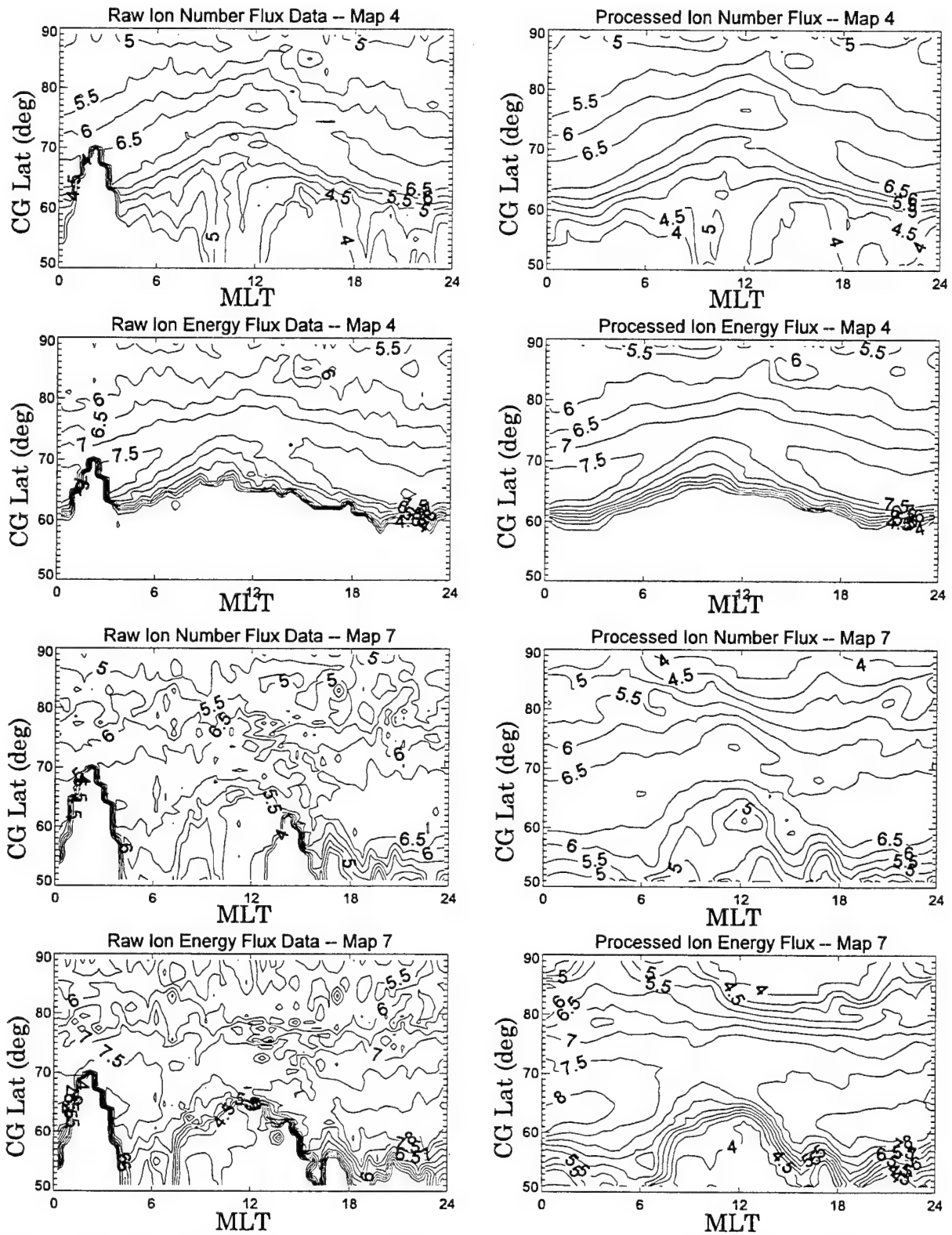
**Figure 16.** The $K_p$ Versions of the Most and Least Statistically Reliable Maps (Map 4 and Map 7 respectively) for the Ion Number Flux and the Ion Energy Flux.
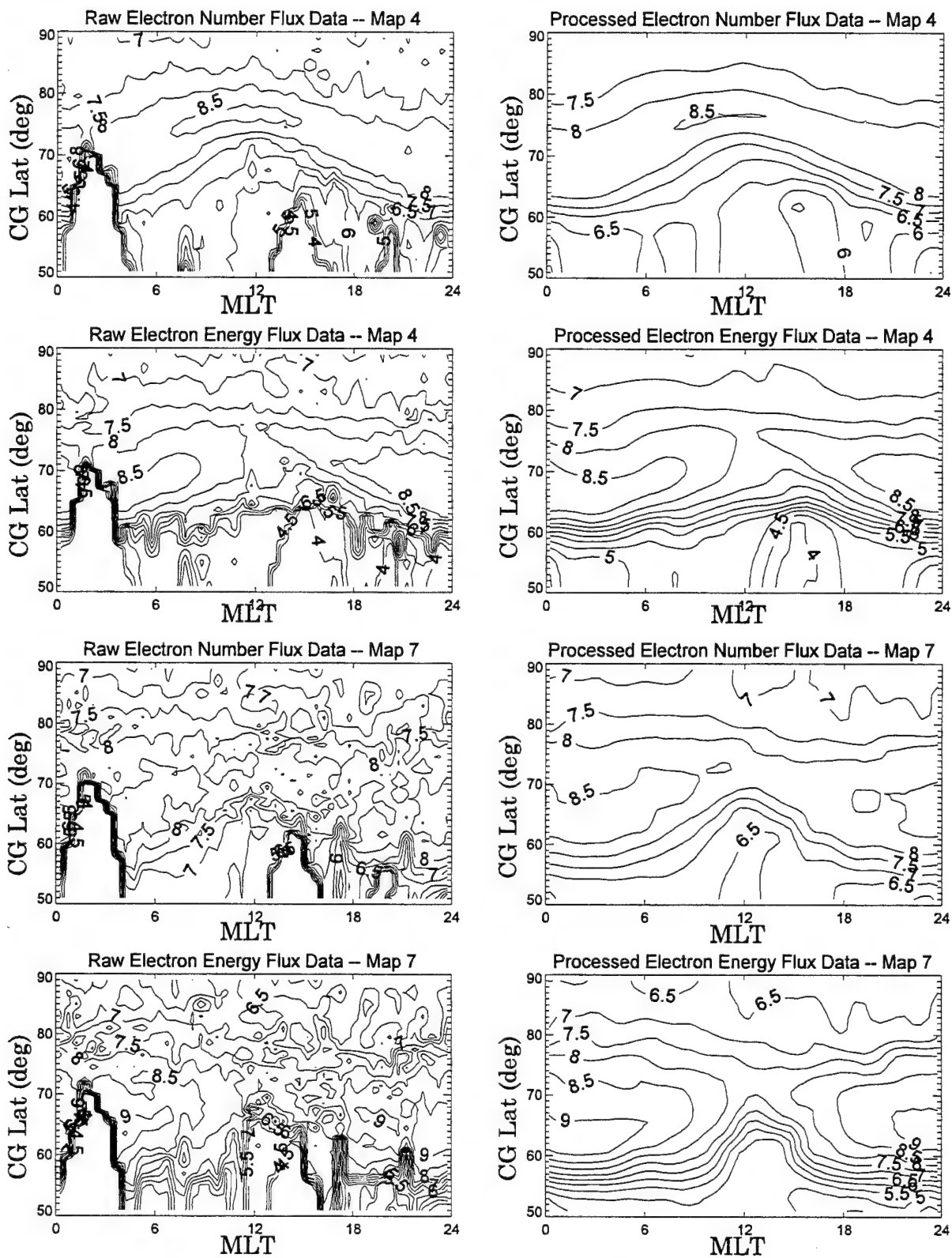
**Figure 17.** Same as Figure 16 Except for the Electron Number Flux and Electron Energy Flux.

29
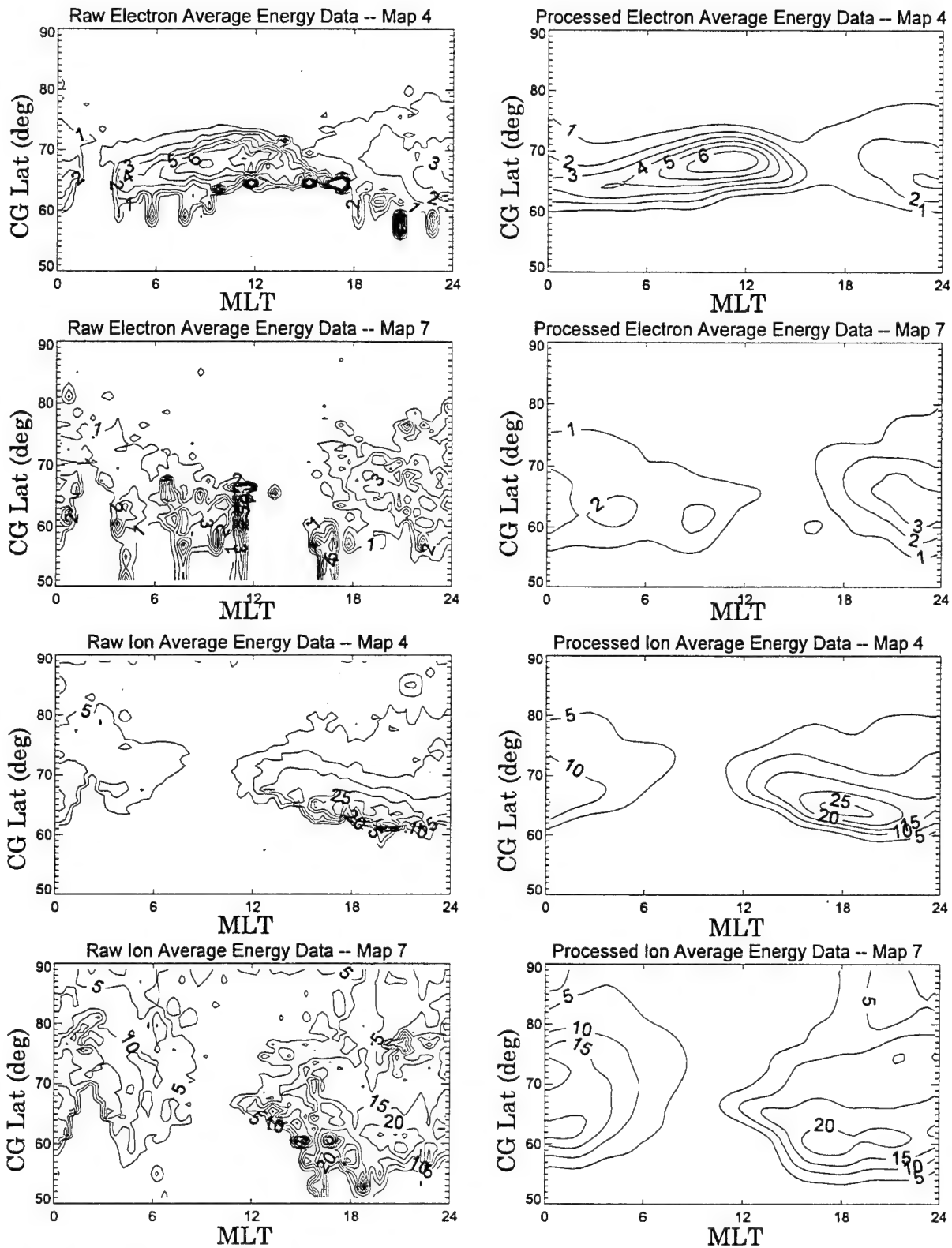
**Figure 18**. Same as Figure 17 Except for the $K_p$ Model Electron and Ion Average Energies (in keV).
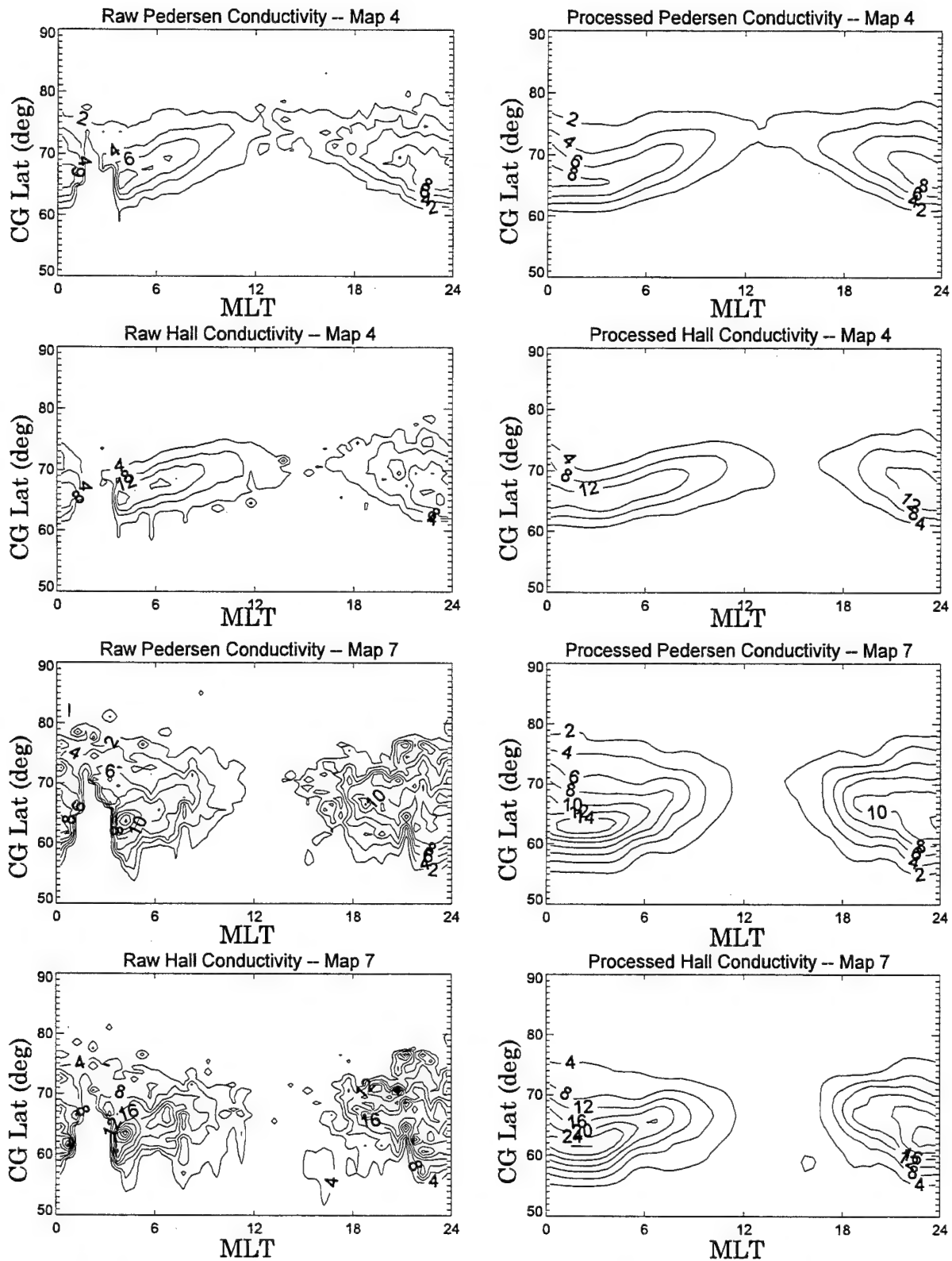
**Figure 19**. Same as Figure 18 Except for the $K_p$ Model Hall and Pedersen
Conductivities (in Mhos).

31

## 3. Functional Expansions

The substantial task of the processing of the DMSP data and generation of the statistical auroral models by binning and averaging the various properties had been completed by others before this work began. These models, along with analyses of the physical characteristics, has for the most part been already published. (See references in Table 1). The input for this modeling is therefore the raw, binned averages of the various properties. The task here is to represent these quantities by simple functional forms.

The idea here is that these functions can then be used in graphical displays and as input for further calculations relying on auroral properties, more easily than can the statistical maps. Furthermore, the fitting process, to a certain degree, smooths and cleans up the binned data, so that one can expect a smooth result as a function of the main variables, CG Latitude and MLT, in place of the statistical fluctuations present in the original binned maps. As opposed to the original maps, too, the functional results are valid throughout the auroral region, and generally equally valid throughout. Therefore, the user need not be too concerned about statistical inaccuracies in certain areas, when using the functional fits as opposed to the original maps. The major utility in this effort, then, is the creation of a convenient, as well as a smooth and verified, representation of the statistical aurora as derived from DMSP.

There are a total of three different functional forms used to represent the eight different quantities in the IMF/SWS and $K_p$ models. The ion and electron energy and number flux are represented by a six–coefficient function in CG Latitude. Since these coefficients represent characteristics of the latitude variation in the flux (and therefore the auroral oval) they are easily expanded in MLT through a Fourier series to give a model valid at any chosen CG Latitude and MLT. No attempt is made to model between $K_p$ values (or IMF/SWS combinations) and therefore, the model must be evaluated for a chosen map in either the $K_p$ or IMF/SWS series. Interpolation could be done, of course, after the quantities are evaluated for various maps.

The conductivities are modeled in much the same way, except that a simplified four–coefficient function is used to represent the CG Latitude variation. This is followed by a Fourier series in MLT. This form was chosen because the latitude variation of the conductivities appeared to be simpler than the variation of the fluxes. Because of ambiguities in the choice of the CG Latitude coefficients, fitting is more difficult if the functional form is substantially more complicated than the data indicates. For the fluxes, the chosen functions reproduce the data best when the fluxes are high. Far from the peaks, below some chosen "background" level, they do not correspond to the data at all. We have, however, chosen some background levels based on the data and incorporated them into the models.

32

For the average energies, though, we have attempted to fit the entire auroral region, albeit weighted substantially by the value of <E>. The justification here is in part because the average energy might be important in all regions, while the fluxes and conductivities are probably most important where their values are high. Also, the general shape of the average energy profiles were not as well represented by the latitude functions as were the fluxes and conductivities. Although the average energy does indeed show a single peak as a function of latitude, as is evident in Figure 18, the breadth of the peaks vary substantially with MLT as well as between individual maps. The average energies were more amenable to fits with orthogonal polynomial functions.

We begin the description of the fitting with the fluxes, for which identical forms were used for electrons and ions and for IMF/SWS and $K_p$ maps. Next, the fitting of the conductivities and finally the average energies are described. The examples shown in this section are not meant to be comprehensive in any way, but only representative of the general results. A more comprehensive survey of how well the fits reproduce the original data is given in Section 4. Because of the large number of maps in the model, though, even this survey is somewhat limited.

3.1. Fitting of the Fluxes

The first step in the fitting of the fluxes is to examine a single latitude profile at each individual MLT value for each map. The characteristic shape of $\log_{10}$ flux, as one increases in latitude, is a relatively flat "background" region, followed by an essentially linear increase, followed by a peak region of varying latitudinal extent, followed again by a linear decrease, finally reaching a different "background" value near the poles. A function which mimics this behavior quite well is the Epstein function, used extensively in atmospheric modeling. These functions can have any number of regions of slope change, or "break–points", but a two break–point version fits this situation well. Eq. (1) gives the functional form.

$$e(h) = r_0 + s_0(h - h_0) + (s_1 - s_2)\log_{10}\left(\frac{1 + e^{h-h_0}}{2}\right) +$$
$$(s_2 - s_1)\log_{10}\left(1 + \frac{e^{h-h_1}}{1 + e^{h_0-h_1}}\right) \tag{1}$$

In Eq. (1) $e(h)$ is the base$_{10}$ logarithm of the energy or number flux and $h$ is the corrected geomagnetic latitude. Although the function may appear complicated at first glance, the behavior is actually quite simple. This is demonstrated in Figure 20, which

shows the correspondence between the parameters and characteristics of the latitudinal variation of the fluxes.
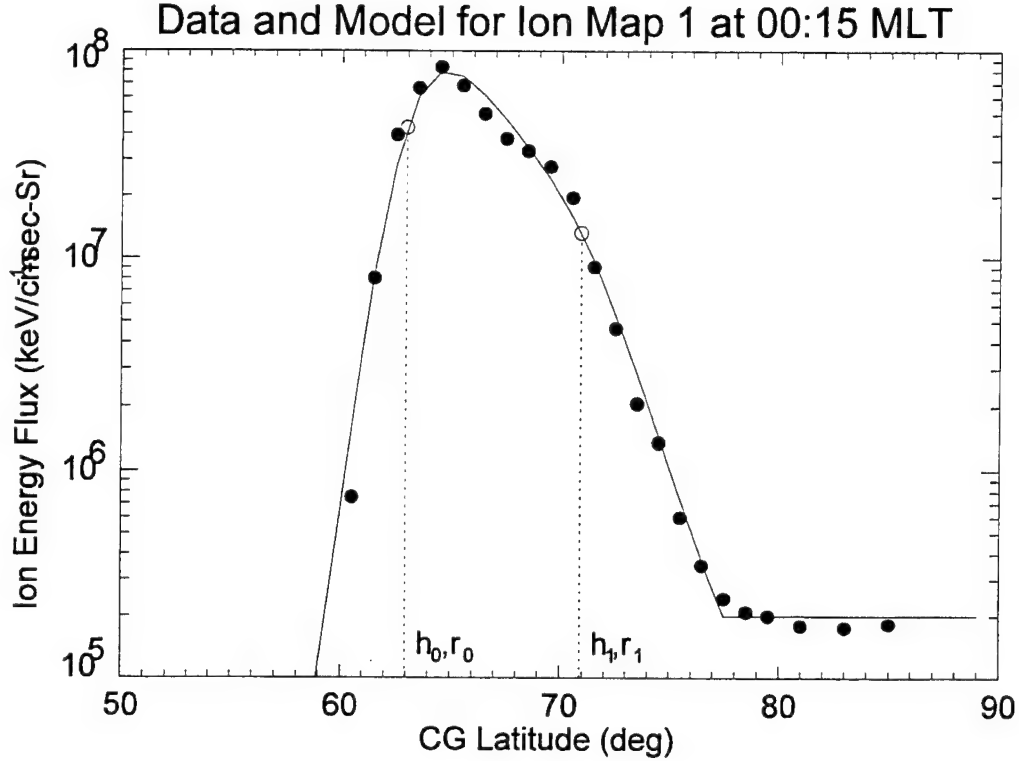


**Figure 20.** Relation Between the Latitudinal Profiles of the Fluxes and the Parameters of the Fit.

The values of $r$ and $h$ therefore fix the values of the functions at two chosen points. The other two parameters $s_0$ and $s_2$ give the slopes of the curves for $h < h_0$ and $h > h_1$ respectively. Eq(1) does not include $r_1$ explicitly. This is because, historically, Epstein functions were used to represent atmospheric density which was specified by a fixed value $r_0$ at a single altitude and by a series of slopes $s_0$, $s_1$, *etc.*, with these slopes changing over specific altitude ranges. We have modified the form of the functions by forcing $e(h)$ to be $r_1$ at $h_1$, which can be achieved by choosing $s_1$ such that

$$s_1 = \frac{r_1 - r_0 - s_0(h_1 - h_0) + s_0 b_1 - s_2 b_2}{b_1 - b_2} \tag{2}$$

with
$$b_1 = \log_{10} \frac{1 + e^{h_1 - h_0}}{2} \qquad b_2 = \log_{10} \frac{2}{1 + e^{h_0 - h_1}} \tag{3}$$

34

The choice of $h_1$ as a parameter makes the latitudinal dependance reasonably easy to fit by just choosing two points along a latitude profile. The decision to use a six parameter Epstein function rather than a four parameter version as in Hardy *et al.* [1987] was dictated by the appearance of the latitude profiles. This is evidenced in Figure 20 where we see that the cut appears to be quite asymmetrical with a pronounced shoulder on the high latitude side. The abruptness of the slope change can be controlled by adding a multiplicative factor to the exponential terms, however, we have found that this is unnecessary in this application.

The task in fitting, then, is to chose the six coefficients so that the Epstein functions best reproduce the latitude profiles of the data at each MLT. There are two problems that arise, though. Since the coefficients can be expected to vary relatively smoothly from MLT to MLT bin, one wishes to chose them consistently throughout a map. This is not particularly difficult for the case shown in Figure 20. However, there are many cases when the latitude profile is smooth, without the "shoulder" of the profile in Figure 20. One such case is shown in Figure 21.
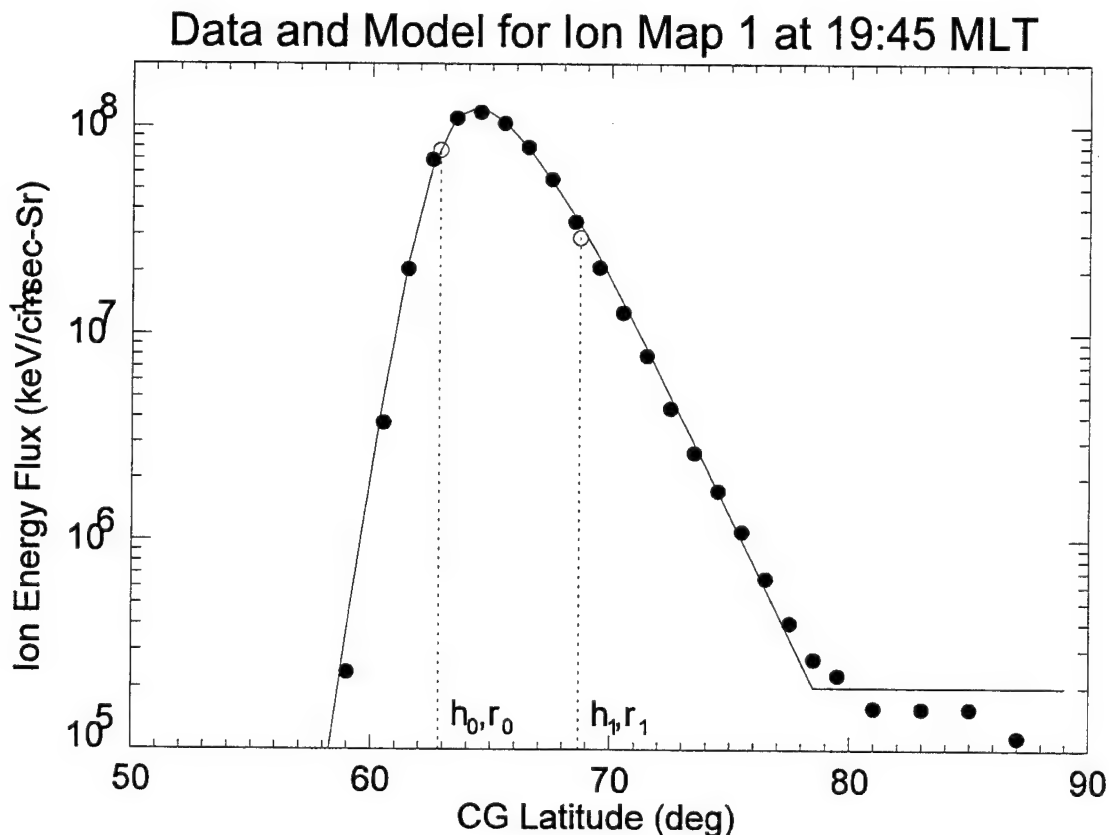


**Figure 21.** Same as Figure 20 but for 19:45 MLT.

The nature of the Epstein functions is such that the second break–point ($h_1$) in the profile in Figure 21 could have been placed more or less anywhere above 65° without changing the "goodness" of the fit. In this sense, then, the problem is under-determined. Since we wish to eventually derive a functional form in MLT to represent the latitude profile coefficients, and thus reduce the number of coefficients in the total model, we need to select the coefficients carefully, especially in cases like Figure 21, so as to preserve some consistency between one MLT and the next.
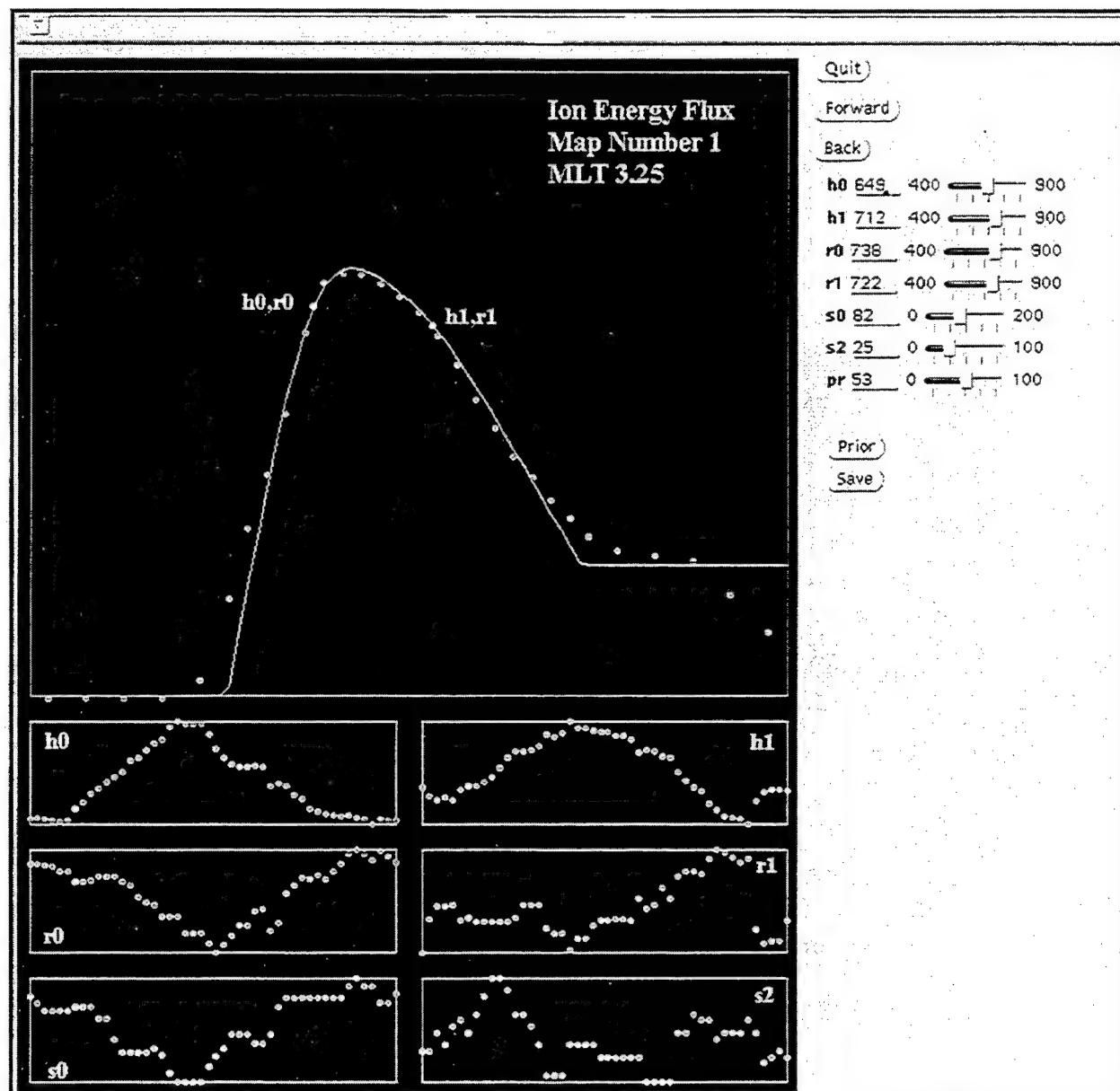


**Figure 22.** The Fitting Tool Used to Generate the Latitudinal Coefficients for the Electron and Ion Flux Models, and for the Conductivities.

In the case of the $K_p$ Ion Flux Model [*Hardy et al.*, 1991] the selection of coefficients was done by hand, with periodic plotting of the results along with several rounds of adjustments. This was a tractable problem because there were only 14 maps in all. When we attempted to do the same thing for the 120 IMF/SWS maps, integral energy and number flux for electrons and ions, along with 14 more for the $K_p$ electron fluxes, it became clear that a better method was needed to choose latitude coefficients. An interactive fitter was therefore developed, as is shown in Figure 22.

The idea behind the process is that one displays each latitude profile (top panel) along with the choices for the two break points. Note that the locations of the two points give four of six parameters needed for Eq(1), the latitudes and functional values. By clicking on the screen, the optimum values can be selected to reproduce the data points. The slopes are adjusted by the sliders on the right hand side of the panel (breakpoints can also be adjusted in this way).

To ensure a consistent choice of coefficients from one MLT to the next, the fitting is usually carried out by first copying the coefficients from the previous MLT bin (through the "Prior" button in Figure 22) then adjusting them as needed for the relatively minor changes in the shape. The six panels in the lower half of the screen show the MLT variations in the six fit parameters. In the case shown in Figure 22, one pass has already been made through this map and therefore the six coefficients are already more or less uniform functions of MLT. The trick is to choose the coefficients so that the MLT variability can be well represented by a few coefficients of a Fourier series in MLT, thereby reducing the total number of coefficients in the model and also providing continuity in MLT. We discuss this later on in this section.

A second problem that arises in the choice of coefficients is the extrapolation through the bite–out areas. We have already shown in Section 2 how various means were used to fill in these areas of no data. However, as is probably evident from several of the figures, there are cases in which these methods gave obvious problems. In general, the first few MLT divisions of each map had good data coverage. By using the interactive fitting technique, all the while keeping watch on the variations in the coefficients with MLT, we were able to extrapolate more satisfactorily over the bite–out regions, thus improving the processed maps from Section 2. This should be kept in mind when we compare the model to the processed data, which may differ in the bite–out regions.

The Epstein functions were fit by eye to individual latitude profiles. The most important aspect of the function for this application, however, is that the numerical values of the coefficients might be expected to be consistent from one profile to the next, as one increases the magnetic local time. This means that the coefficients derived at each latitude can themselves be expanded in the magnetic local time domain. We do this through a Fourier series for a specific coefficient A(MLT) with A being one of the two slopes $s$, heights $h$ or set-point values $r$.

$$A(T) = \frac{c_0}{2} + \sum_{i=1}^{6} c_i \cos(T) + \sum_{i=1}^{6} s_i \sin(T) \qquad (4)$$

where $T = \pi\, h\, /12$ and $h$ is the MLT in hours. The order of the fit was chosen large enough so that the features of the auroral maps would be retained but not so high that spurious noise would be included in the model. The agreement between the model latitude profiles and the smoothed data, as seen previously in Figures 20 and 21, was really quite good overall, however, this agreement is only obtained after careful fitting. It was the intention, then, that the expansion in MLT not degrade that agreement. Figure 23 compares a typical set of latitude coefficients with the results of the Fourier expansion. Clearly, the series well reproduces the latitude variations in the coefficients, and often smooths some of the noise.
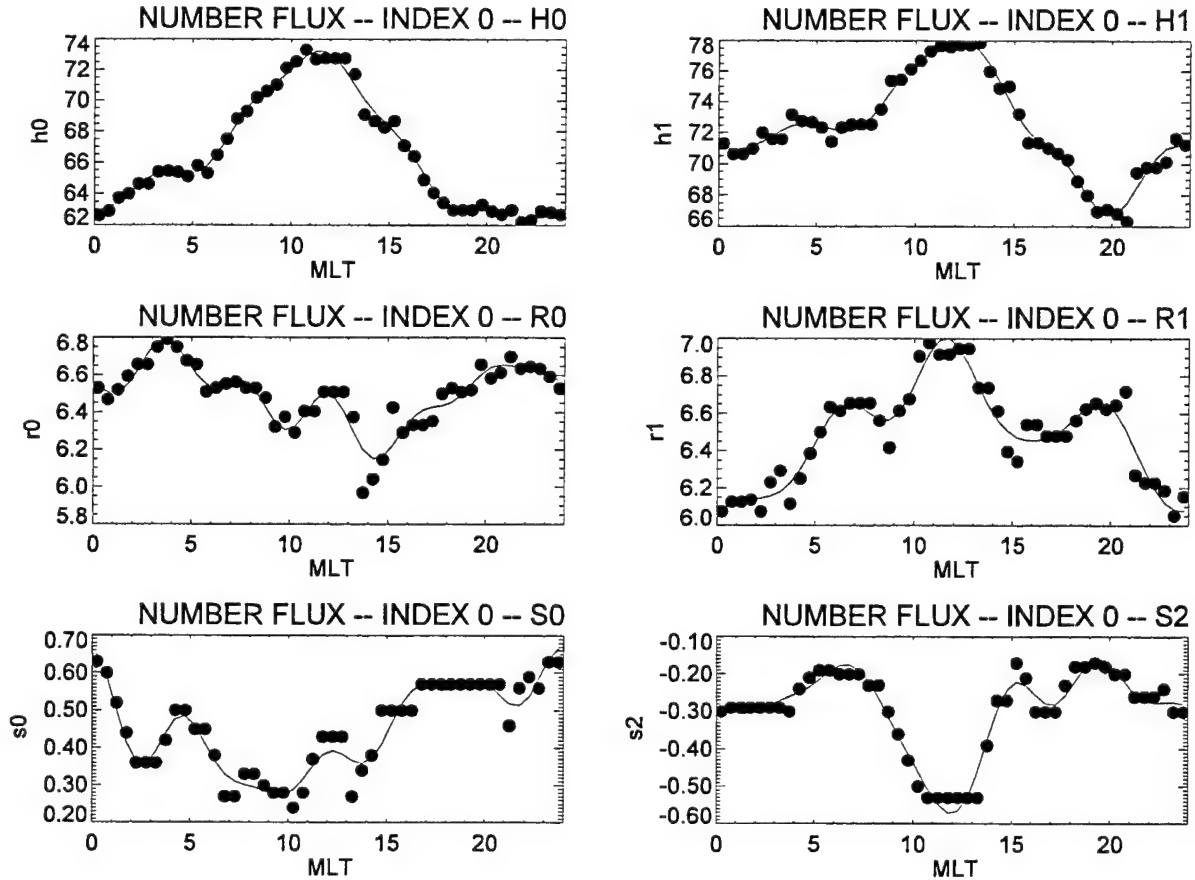


**Figure 23**. Coefficients Selected from the Interactive Fitting (closed dots) and Results of the Fourier Expansion (solid line) for the First Ion Number Flux Map of the IMF/SWS Models.

38

This, then, completes the modeling of the fluxes. The models consist of an array containing 13 Fourier coefficients for each of the six parameters in the Epstein function. There is one set for each case of energy and number flux, for both ions and electrons, for each of the 30 maps of the IMF/SWS model and the 7 maps of the $K_p$ model. In the case of the $K_p$ electron fluxes, 17 coefficients were used because the MLT dependence seemed to be more strongly varying, that is, more coefficients were needed to achieve equally good representations of the MLT variation of the selected latitude coefficients.

To evaluate a particular map, one first computes the values of the six coefficients for a chosen MLT from Eq. (4). Eqs. (1) through (3) are then used to find the value of the property at the chosen latitude. As noted previously, although the model allows for calculations at arbitrary CG Latitude (above 50°) and MLT, it does not interpolate between maps. Therefore, quantities must be generated at specific parameter ranges in either Table 2 or Table 3. Interpolation can, of course, be done afterwards.

We noted previously that the flux models were valid whenever the flux remained above a "background" level. It is obviously the case that the two–break Epstein functions will trail off to very small values either toward the poles or toward low latitudes. We have incorporated "backgrounds" into the models and into the software. For all but the Ion Fluxes from the $K_p$ maps, we have determined a background level for each of the maps. This level can be seen toward high latitudes in Figures 20 through 22. An average value was determined for each map and in the software, the poleward flux value is set to this background value whenever the Epstein function would result in a lower value of the flux. On the equatorward side, we have chosen not to limit the value but rather to allow the flux to decrease unchecked. This is because, while the poleward background probably has some physical meaning and is adequately reproduced from the data, the equatorward background may be more instrumental in origin. In any case, the equatorward background level in the data is substantially lower. For the $K_p$ Ion Fluxes, a functional form is used for *both* a poleward and equatorward limit, one each for each $K_p$ map. This is functionally identical to the poleward limits of the other maps. These were also based on the data, however, the equatorward limit is again probably more instrumental than physical and may easily be disabled by the user, if desired, for consistency between the models.

Figures 24 through 29 compare the smoothed and edited maps resulting from the procedures described in Section 2, with the regenerated fits. These examples are the same as were given in Section 2, that is, the statistically "best", "worst" and "average" maps. Note that in some cases, bad regions arising from one or two spurious points in the raw data have been corrected in the fits. Also, the "trails," which we believe might have arisen from contaminated passes, have been corrected in the model. There is some oscillation in the slope of the equatorward boundary, necessary to achieve good fits near the peaks. Overall, though, the model reproduces the data very well.

39
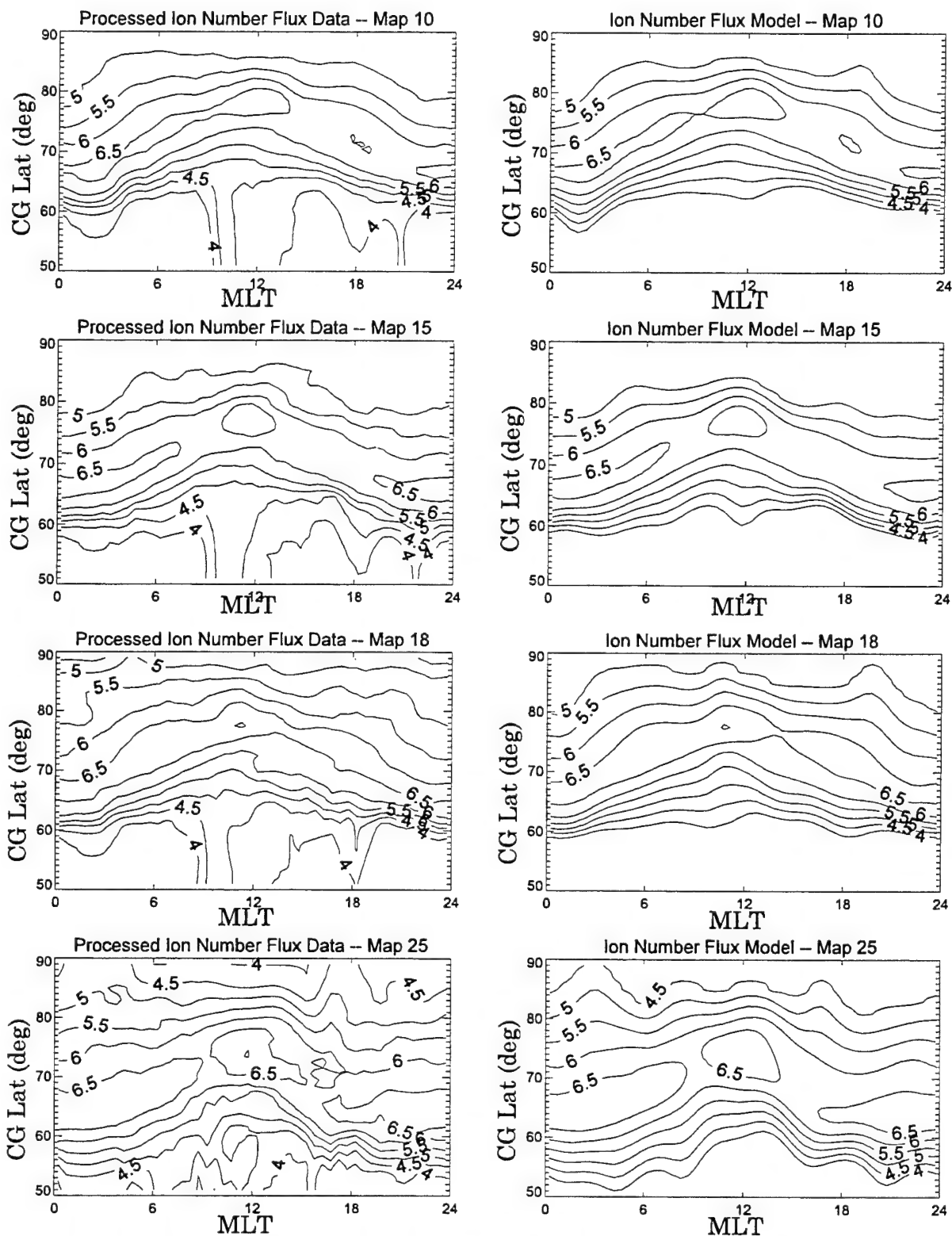
**Figure 24**. Comparisons of the Smoothed and Processed Data (left) with the Results of the Model (right) for IMF/SWS Ion Number Flux Maps of Varying Statistical Reliability (units of ions/cm²–sec–Sr) (best at top and worst at bottom).
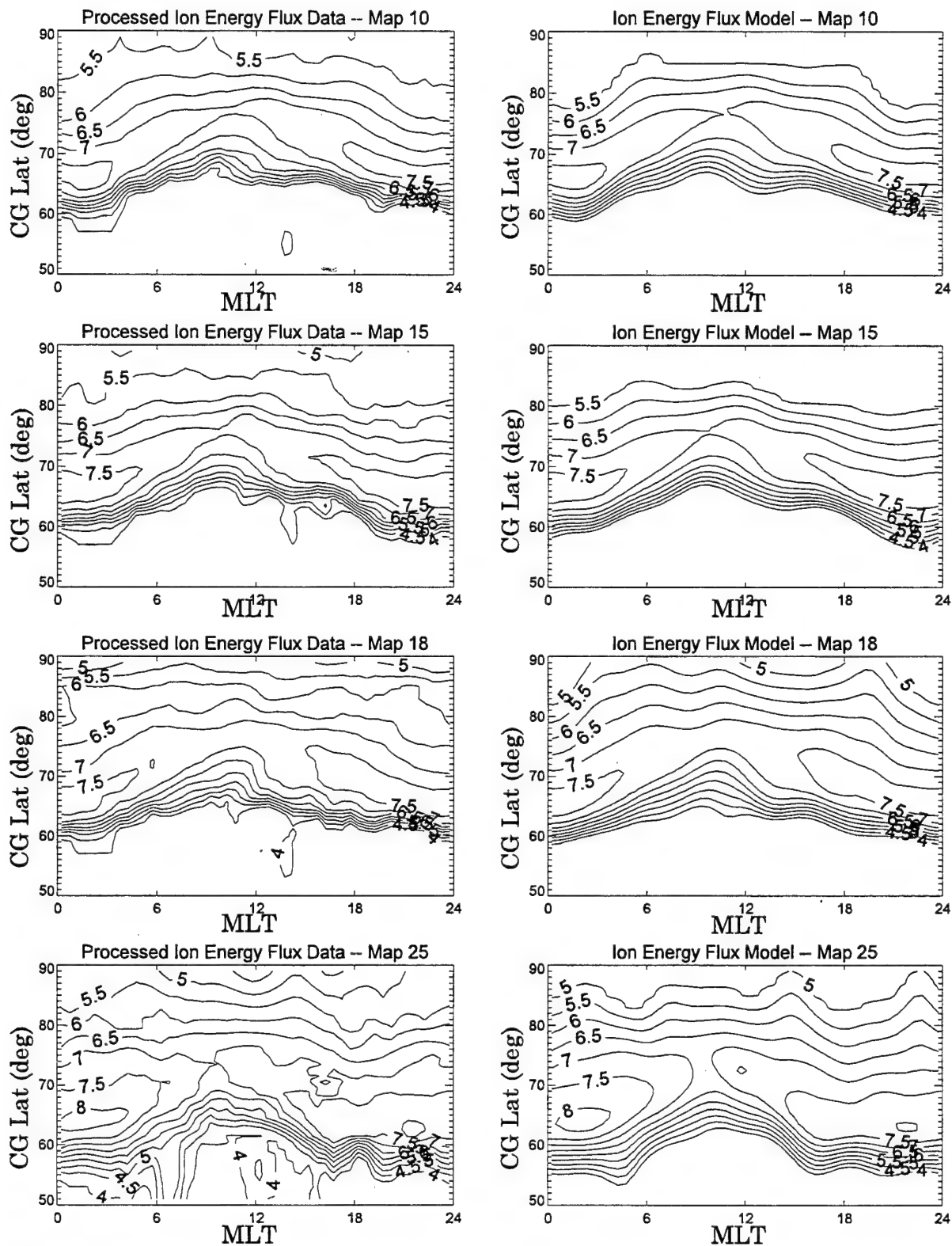
**Figure 25.** Same as Figure 24 Except for the Ion Energy Flux (keV/cm²–sec–Sr).
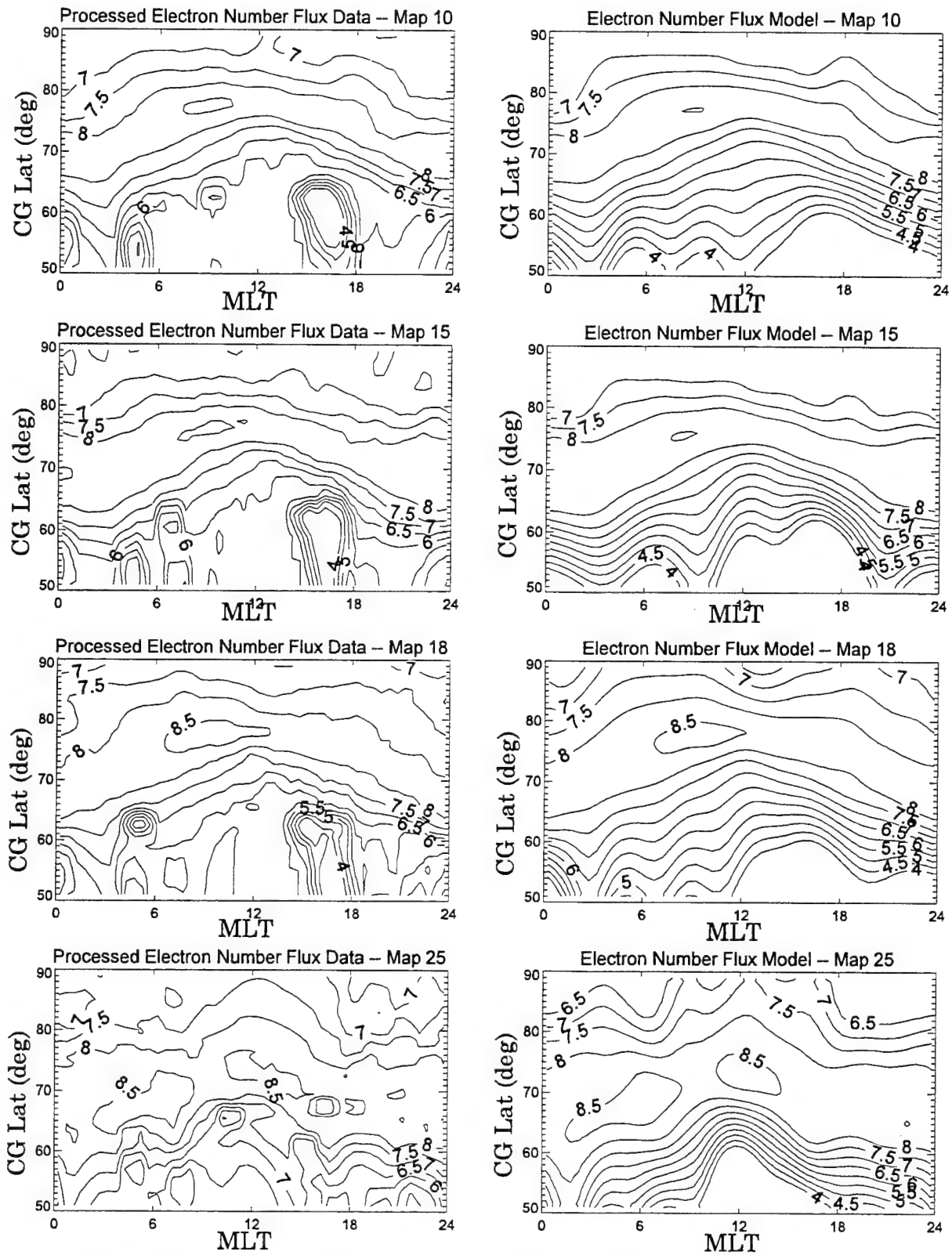
**Figure 26.** Same as Figure 25 Except for the Electron Number Flux (electrons/cm²–sec–Sr).

42
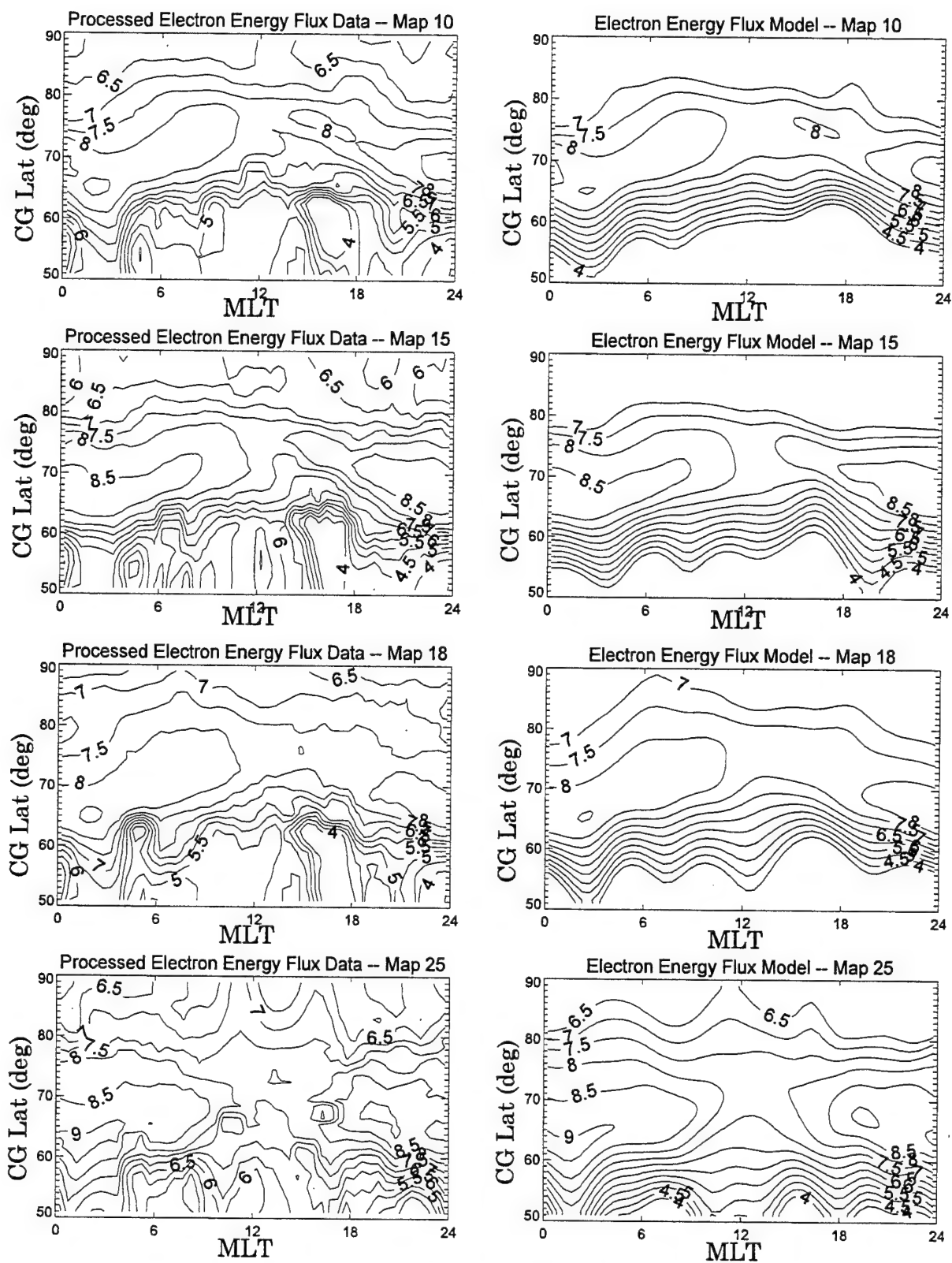
**Figure 27.** Same as Figure 26 Except for the Electron Energy Flux
(keV/cm$^2$–sec–Sr).

43
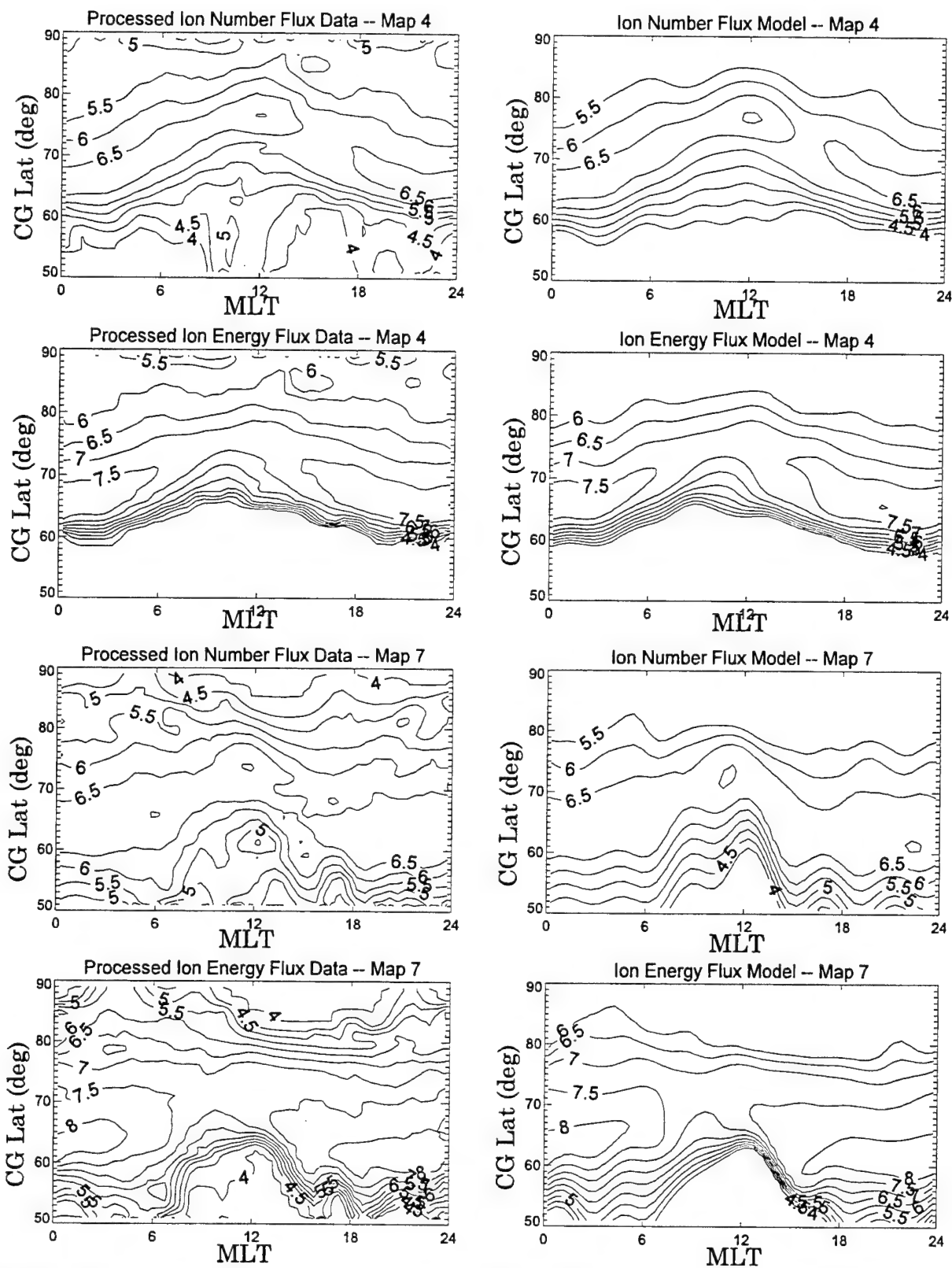
**Figure 28.** Comparisons of the Smoothed Data (left) and the Results of Modeling (right) for the "Best" and "Worst" Map Statistically, for the $K_p$ Version of the Ion Number Flux and Ion Energy Flux.

44
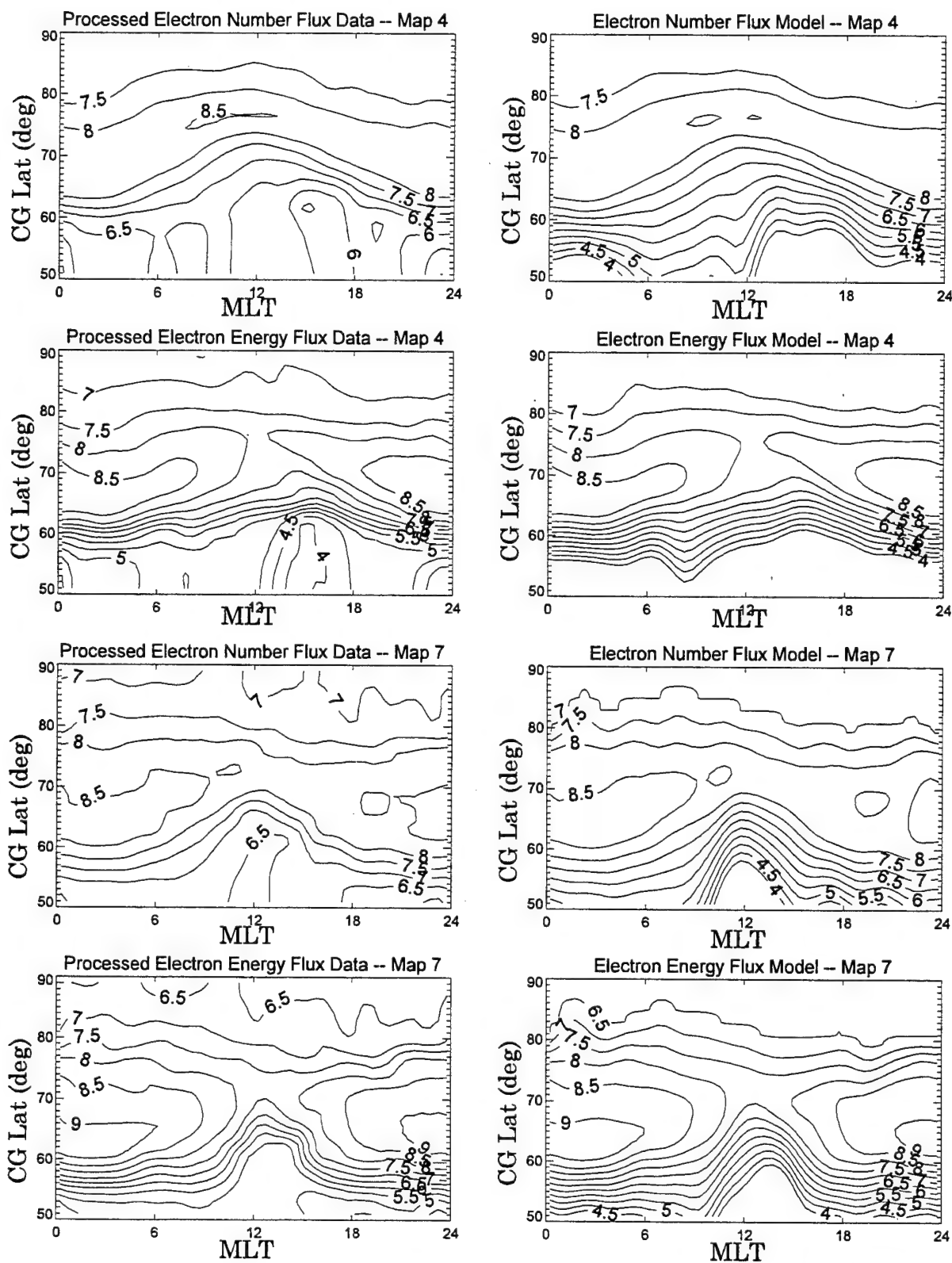
**Figure 29.** Same as Figure 28 Except for the $K_p$ Electron Number and Energy Flux.

## 3.2. Fitting of the Conductivities

The conductivities are fit in the same way as the fluxes with two exceptions. First, the functional form used for the CG Latitude dependence is an Epstein function with a single breakpoint. This simpler form was used because the conductivities generally have a sharp rather than a broad peak and do not exhibit the "shoulders" that were often seen in the fluxes. Eq. (5) gives the functional form used.

$$\sigma(h) = r_0 + s_1(h - h_0) + (s_2 - s_1)\log_{10}\left(\frac{1-(s_1/s_2)\sigma^{h-h_0}}{1-s_1/s_2}\right) \tag{5}$$

Here, $\sigma$ is the conductivity as a function of the CG Latitude $h$ (in degrees). The value of the conductivity at the peak, $h_0$ is given by $r_0$ and the slopes on either side are $s_1$ and $s_2$. The second difference is that the conductivities and not the $\log_{10}$ are fit.
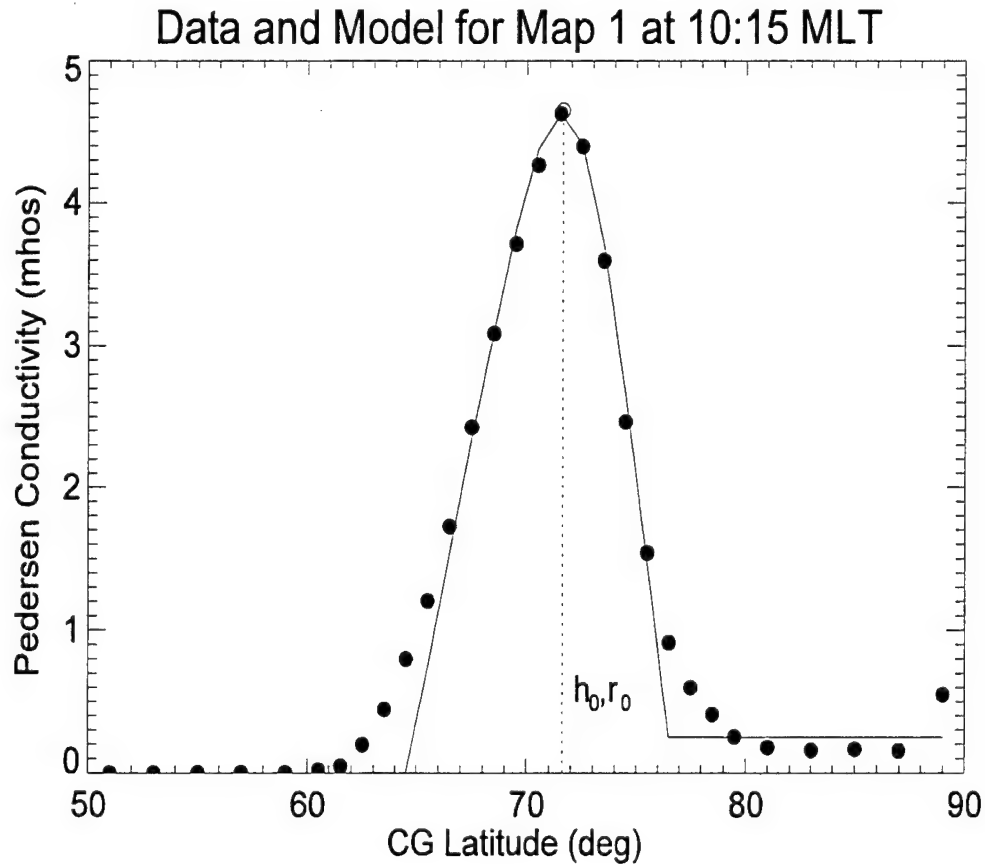


**Figure 30.** An Example of a CG Latitude Profile of the Conductivities.

Figure 30 shows a typical latitude profile of the conductivities along with the model result. Here, the coefficients of the Epstein functions have an even clearer meaning, with the breakpoint occurring precisely at the peak. Not surprisingly, these coefficients are even easier to choose than those for the fluxes and, accordingly, are very well constrained by the data. Figure 31 shows a typical MLT fit, which is done with the same Fourier function we saw in Eq. (4).
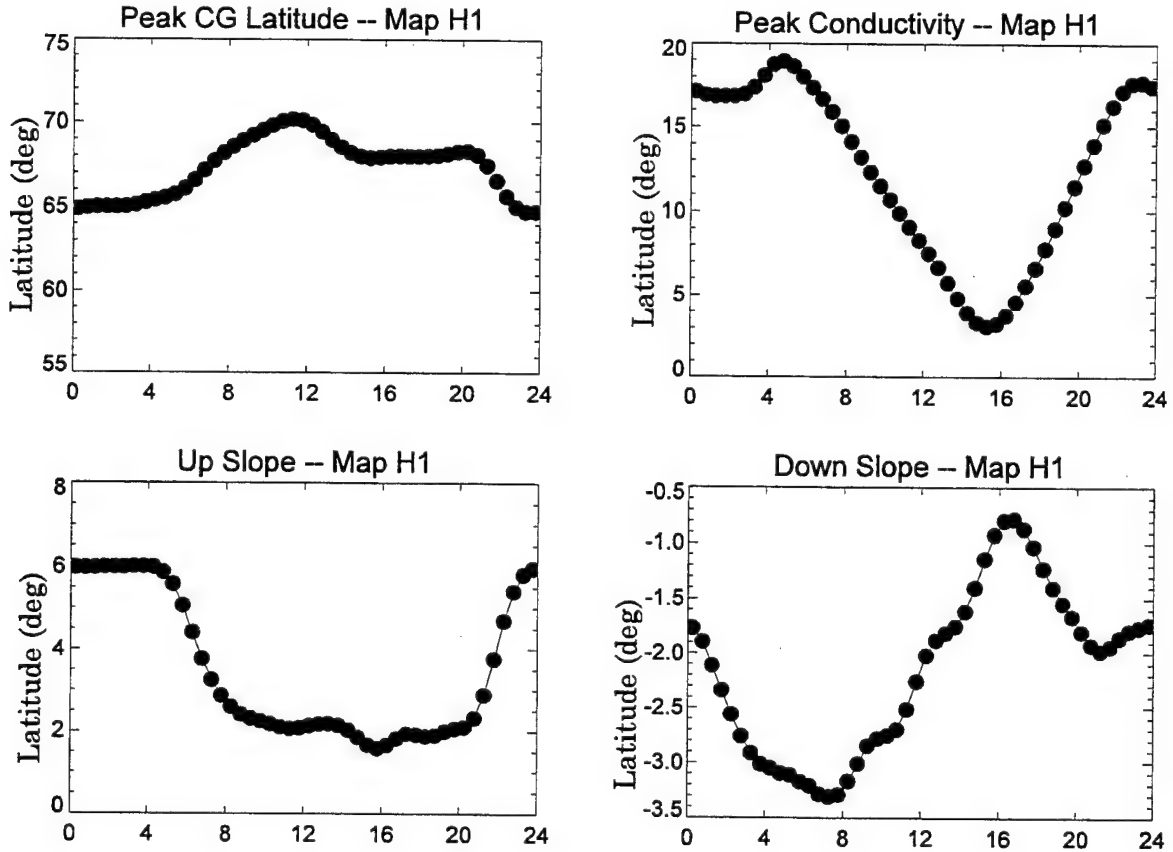


**Figure 31.** Comparisons Between the Coefficients Selected for the Latitude Profiles for the Pedersen Conductivity IMF/SWS Map 1 (Dots) and the Fourier Series Fit to the Same.

We note that for the conductivities, a 13–term Fourier expansion was used for both the IMF/SWS and the $K_p$ maps. For the background levels, we have selected a threshold of 0.25 for both the poleward limit and a value of zero for the equatorward limit. That the conductivities go to zero below the oval is clear from the data. The poleward limit is also based on the data, although differences between one map and the other in the polar cap were not sufficient to warrant different values for individual maps.

The following plots show the comparisons between the smoothed data and the model results for the usual cases. As before, we see that the interactive fitting and Fourier expansion has corrected some difficulties in the original data set.

47
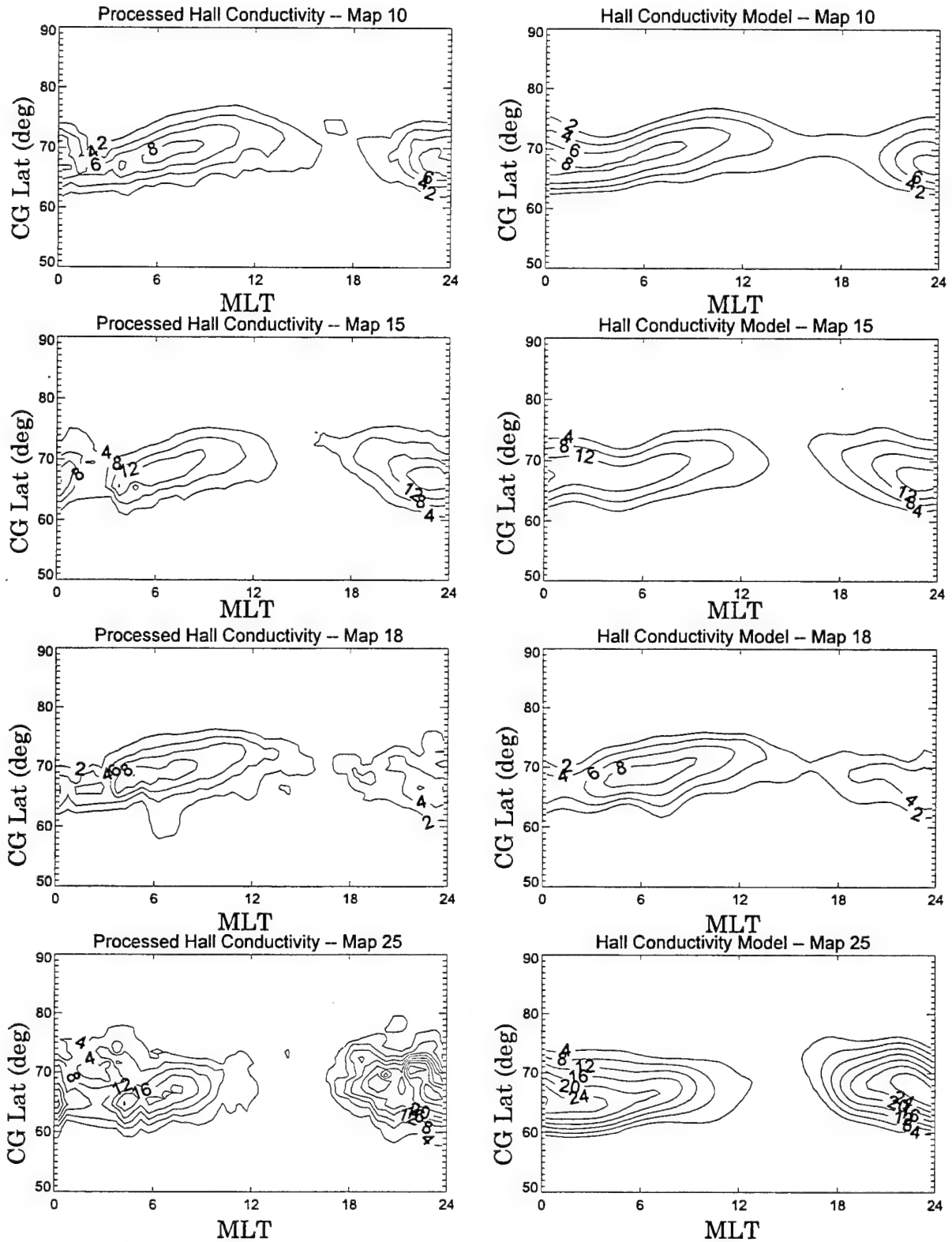
**Figure 32.** Comparisons of the Edited and Smoothed IMF/SWS Hall Conductivities (in mohs) and the Results of the Model for the Same. Note that the expansion has effectively smoothed over the bite–out region around 0300 MLT.
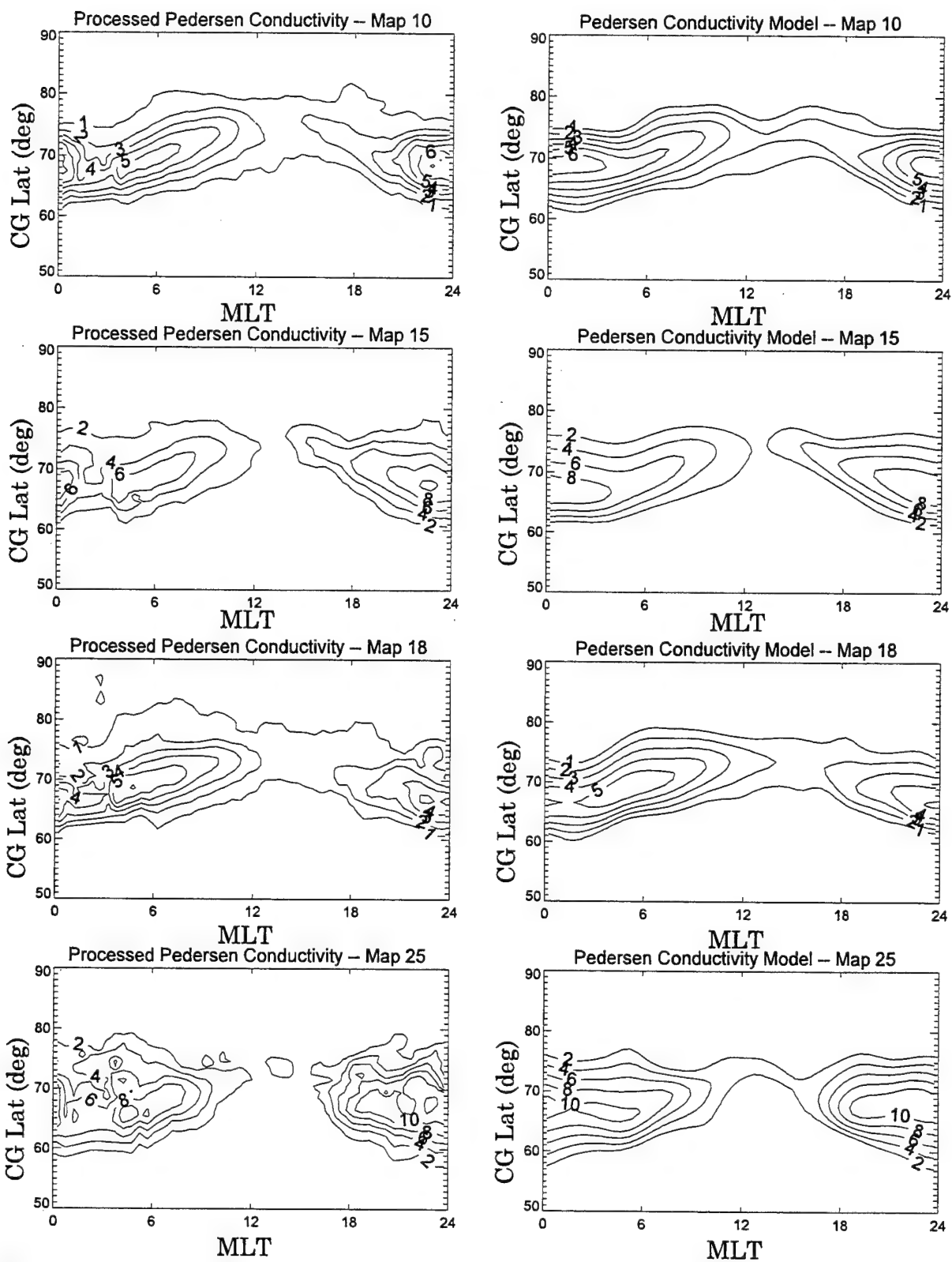
**Figure 33.** Same as Figure 32 Except for the Pedersen Conductivities of the IMF/SWS Maps.

49

**Figure 34.** Comparisons Between Smoothed Data and Model for the Conductivities from the $K_p$ Maps (in mhos).

## 3.3. Fitting of the Average Energies

The ion and electron average energies are derived directly from the energy and number flux. They were not amenable to fitting with the same types of functions used for the fluxes or the conductivities. Figure 35 shows the ion average energy CG Latitude profiles at MLT noon and midnight for four of the IMF/SWS maps.
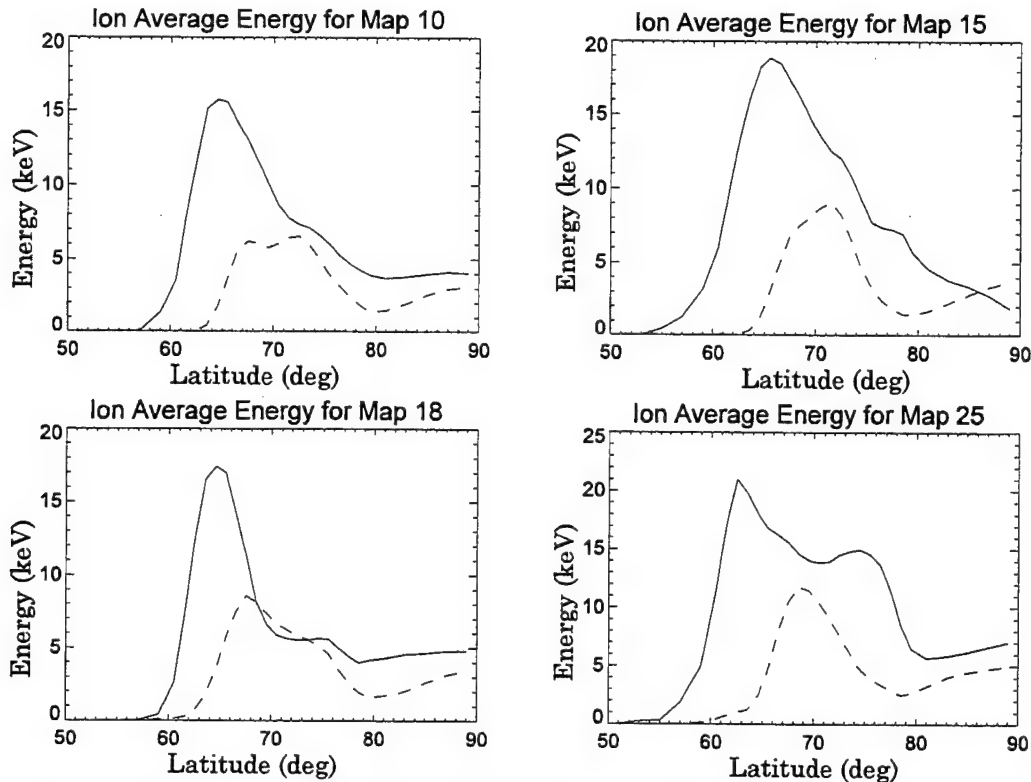


**Figure 35.** CG Latitude Profiles at MLT Midnight (solid line) and MLT Noon (dashed line) from Four of the IMF/SWS Ion Average Energy Maps. Average energy in keV.

The latitude profiles tend to be somewhat broader than those of the fluxes. Although there is a definite maximum, which is also obvious from the contour plots in Figure10, there is often a very prominent secondary maximum within the auroral oval. Also, especially for the ions, there appears to be a local minimum around 80° CG Latitude and noon MLT. This results from contributions from a second population of low energy ions from the magnetosheath.

Looking back at the Ion Flux contours, we can see that the cusp ions, at MLT noon, arise near the peak of the number flux. However, Figure 35 shows that the peak of the average energy is substantially lower in latitude than the peak of either of the fluxes.

It is clear that a model of the average energy needs to reproduce in some detail the behavior both at the average energy peaks in CG Latitude and higher up in the polar cap, where average energies are often significant. It is also clear that the Epstein functions, at least without the addition of one or more new breakpoints, would not cleanly represent the CG Latitude behavior of the average energy. Adding breakpoints beyond two would both increase the size of the model and probably make the fitting process too difficult.
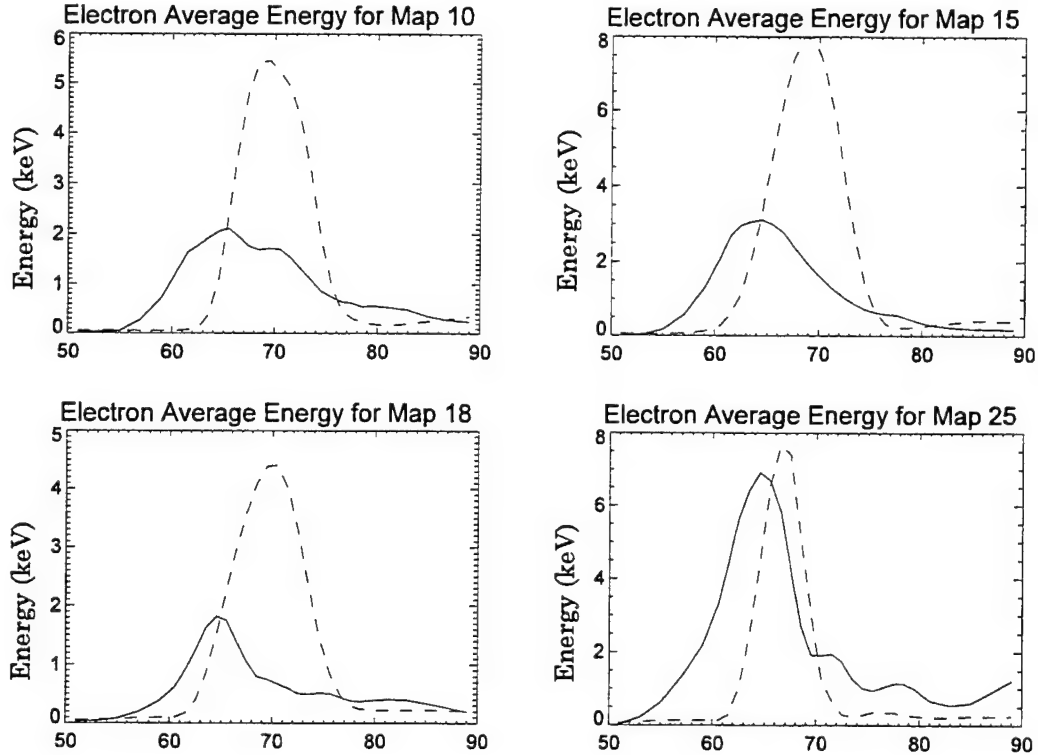


**Figure 36.** Same as Figure 35 Except for the IMF/SWS Electron Average Energy.

Figure 36 shows the corresponding plot for the electron average energy. While these are perhaps a little more like the fluxes in the general appearance, the peaks are more Gaussian in shape than the fluxes. Even these would not be fit well by the Epstein functions.

We have, of course, considered the possibility of simply modeling the average energies with the ratio of energy flux to number flux, as derived from the model. Figure 37 shows a few cases for the ion fluxes, and shows well the problems that arise. The general result is that the average energies are quite well recovered in the peak regions. There are, however, significant problems off the peak, especially near the equatorward boundary.
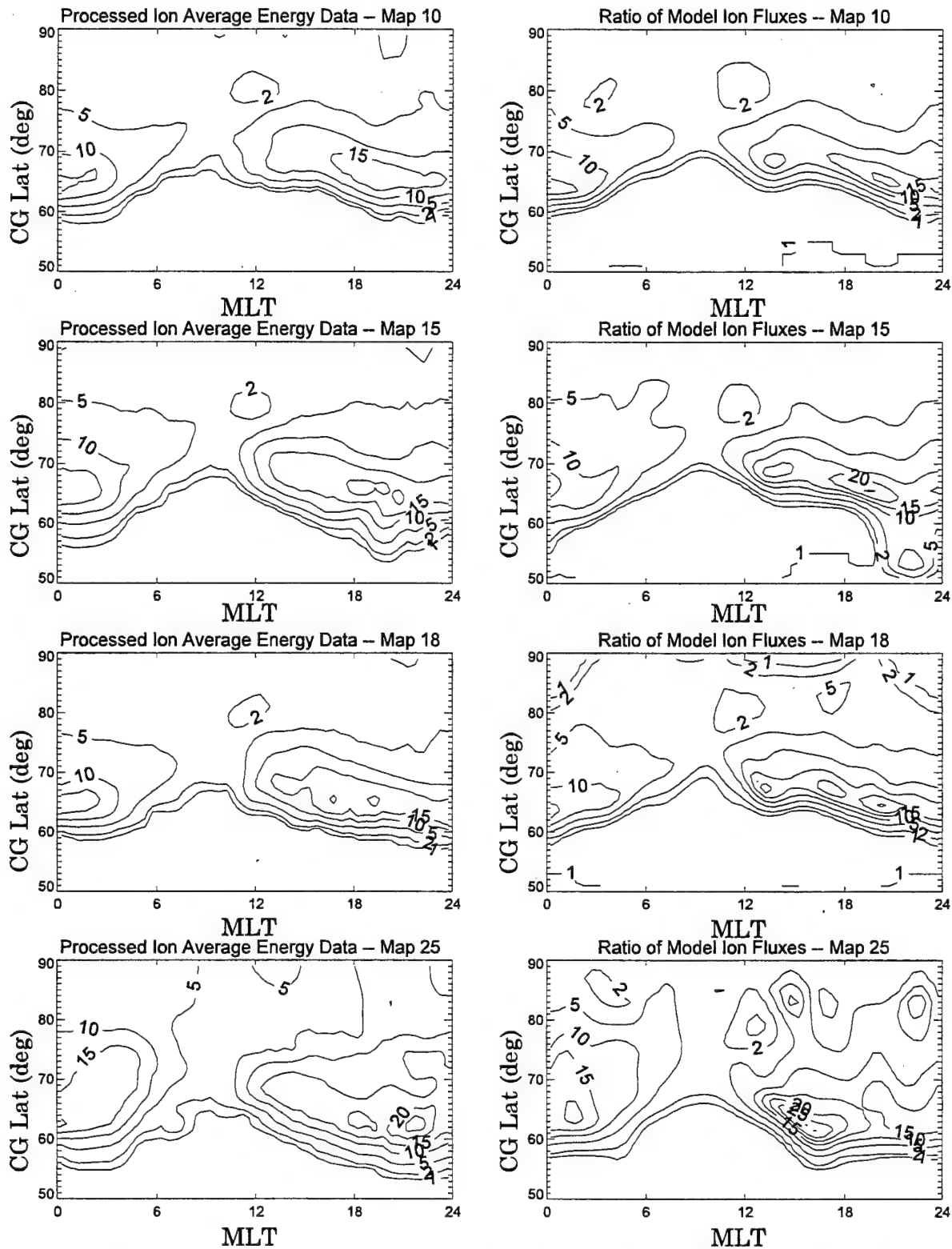
**Figure 37.** Comparison of the Smoothed Ion Average Energy from the IMF/SWS Maps (left) with What One Would Obtain by Simply Dividing the Model Ion Energy Flux by the Model Ion Number Flux (right).

This is not entirely unexpected because the fluxes are fit on a $\log_{10}$ scale, with the greatest attention paid to the peak region. We noted before that the peak of the average energy appeared to be several degrees lower than the peak of either the number or energy flux. In any case, to adequately model the average energies, we sought a different sort of functional form altogether.

We are in search of a functional form that will be completely general in latitude behavior, that is, one which is not biased in any way toward an assumed behavior. Since we require, too, a functional form which is amenable to numerical fitting, the use of orthogonal polynomials to represent the average energies as a function of latitude seems a reasonable choice. Often, as in the case of the Earth's internal magnetic field, the spherical harmonic expansion is used. This amounts to a combination of Legendre polynomials to represent the (here geographic) latitude variation and a Fourier series for the variability in longitude. These functions, however, have the disadvantage that they are constrained to go to a single value at the poles. Although this is reasonable for one end of our data set, at 90° CG Latitude, the use of Legendre functions would require some arbitrary extrapolation of our data set below the lower CG Latitude limit of 50°. Also, since in our case, northern and southern "hemispheres" are identical, half of the Legendre functions would have zero coefficients.

Another set of orthogonal polynomials which are used extensively in fitting and data smoothing applications are the Chebyshev polynomials. An attractive feature of these is that they generally lead to better conditioned matrices for least squares analysis than do simple power series, from which they are derived. The Chebyshev polynomials satisfy the differential equation

$$(1 - x^2)\frac{d^2 g_k}{dx^2} - x\frac{dg_k}{dx} + k^2 g_k = 0 \tag{6}$$

and the polynomials can be generated from a recursion relation, assuming the first two polynomials are known.

$$g_{k+1}(x) = 2xg_k(x) - g_{k-1}(x) \tag{7}$$

This relation is very convenient for coding both the fitting routines and the routines used to regenerate the model from the fit coefficients. The polynomials themselves are sums of powers of $x$ and the first few of them are given below.

$$g_0(x) = 1$$
$$g_1(x) = x$$
$$g_2(x) = 2x^2 - 1 \tag{8}$$
$$g_3(x) = 4x^3 - 3x$$

The Chebyshev polynomials are orthogonal on the interval [-1,1] and therefore, $x$ in this application is defined as

$$x' = 2(CGLat - 50)/40 - 1 \tag{9}$$

In these data sets, there are more points at CG Latitudes near the auroral oval than either above the poleward edge or below the equatorward edge. This will naturally weight the fitting more heavily near the auroral region. It has proven beneficial, though, to add an extra weight to the region of the oval by redefining $x$ as follows:

$$x = SIGN(x')ABS(x')^{\frac{2}{3}} \tag{10}$$

This effectively stretches the region around the oval and compresses the region on either side of it. The factor of two–thirds was determined to be the most effective in reproducing the map values in the peak region.

The functional form combines L Chebyshev polynomials with 2M+1 Fourier coefficients to give the following dependence anywhere in the polar region.

$$A = \sum_{i=0}^{L-1} a_i y_i(x) + \sum_{i=0}^{L-1} \sum_{j=1}^{M} b_{ij} y_i(x)\sin(\frac{j\pi MLT}{12}) + \sum_{i=0}^{L-1} \sum_{j=1}^{M} c_{ij} y_i(x)\cos(\frac{j\pi MLT}{12}) \tag{11}$$

with A the *natural logarithm* of the average energy. And so there are L(2M+1) coefficients in all, for each map in the series. The values of L and M were chosen to be 10 and 6 respectively, so each map in the model is contained in 130 coefficients, ten Chebyshev polynomials along with a 6th order Fourier fit. These numbers were, again, determined by optimizing the resulting fits.

To compute the coefficients in Eq. (11) we need only to perform a single least squares reduction of the data, once the number of coefficients is set. We minimize the sum of the squares of the difference between Eq. (11) and the data at each valid data point.

$$R = \sum_k [A(x_k, MLT_k) - F_k]^2 \tag{12}$$

where $F_k$ is the value of the logarithm of the average energy at one of the points $k$ in the map. Differentiation of Eq. (12) with respect to each of the coefficients in Eq. (11) gives us a series of L(2M+1) linear equations that can be solved directly for the coefficients $a_i$, $b_{ij}$ and $c_{ij}$. The mathematical problem can be cast in a generalized form suitable for solving as a linear set of equations by considering the vector

$$B_1 = \left\lfloor y_0(x_k) ; y_1(x_k) ; \ldots y_{L-1}(x_k); \right| \tag{13}$$

and a second vector

$$B_2 = [y_0(x_k)\sin(\frac{\pi\, MLT_k}{12}) ; y_1(x_k)\sin(\frac{\pi\, MLT_k}{12}) ; \ldots y_{L-1}(x_k)\sin(\frac{\pi\, MLT_k}{12}) ;$$
$$y_0(x_k)\sin(\frac{2\pi\, MLT_k}{12}) ; \ldots y_{L-1}(x_k)\sin(\frac{Mpi\, MLT_k}{12})] \tag{14}$$

and a third vector $B_3$ identical to Eq. (14) except with cos() replacing sin(). If we make a new vector B from

$$B = [B_1 ; B_2 ; B_3] \tag{15}$$

we can now compute the matrix of the system of linear equations solving the least squares problem from

$$M_{ij} = \sum_k b_i(x_k, MLT_k)\, b_j(x_k, MLT_k) \tag{16}$$

with the sum over all points in the map in use for the fitting. We then make another vector m from

$$m_l = \sum_k F(x_k, MLT_k)\, b(x_k, MLT_k) \tag{17}$$

And the product of M and m yields the least squares coefficients.

The procedure so far has implicitly provided some weighting toward the peak, first by using the natural logarithm and then by spreading out the peak region through Eq. (10). We have also increased the weighting of the peak values in the fitting by weighting them according to the fraction of peak value. The highest average energies are weighted five times more heavily than the lowest. Again, these numbers were determined based on trial and error, judging from the agreement between data and fit.
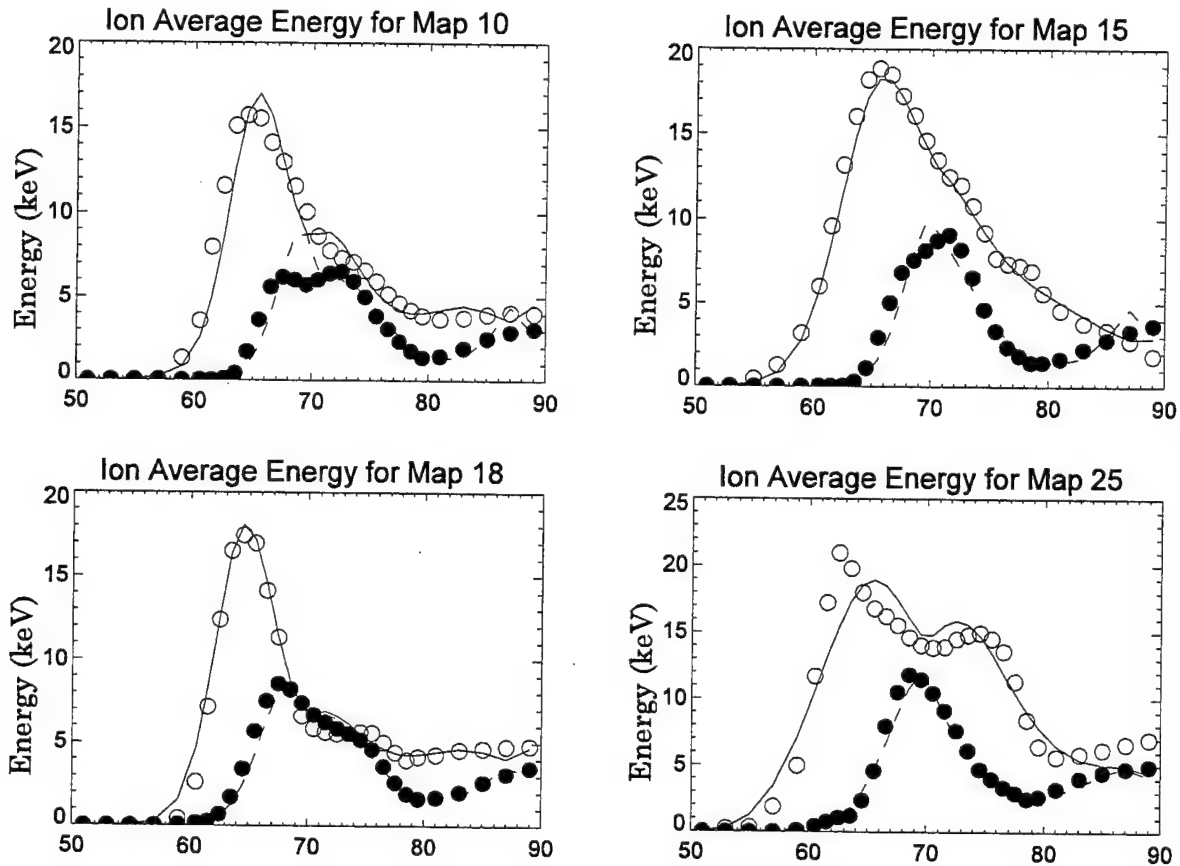


**Figure 38.** Comparison of CG Latitude Profiles of the Processed IMF/SWS Ion Energy Flux (circles) With Results of Modeling With the Chebyshev/fourier Expansion (Lines) for Four Maps at MLT Noon (filled circles) and Midnight (open circles).

Figure 38 shows latitude profiles from four maps, comparing the modeling results with the original data. For the most part, the peak values of the average energy have been preserved well in the fit. The values toward the equator fall off to zero, in both model and data, and the values of the flux in the polar cap are represented about as well as those near the peak. We have also been able to preserve the minimum near the cusp. Keep in mind that these functions have 130 coefficients, compared to 78 for the fluxes and conductivites. Because of the more complicated behavior, as well as the greater latitudinal extent over which the average energy model is valid, the representation

57

seems quite adequate. It is important to note that some of the behavior in the latitude profiles of the data is spurious and does not persist from MLT to MLT. The functions have smoothed over this sort of thing, which is not apparent in Figure 38 but is clearer in contour plots shown later.
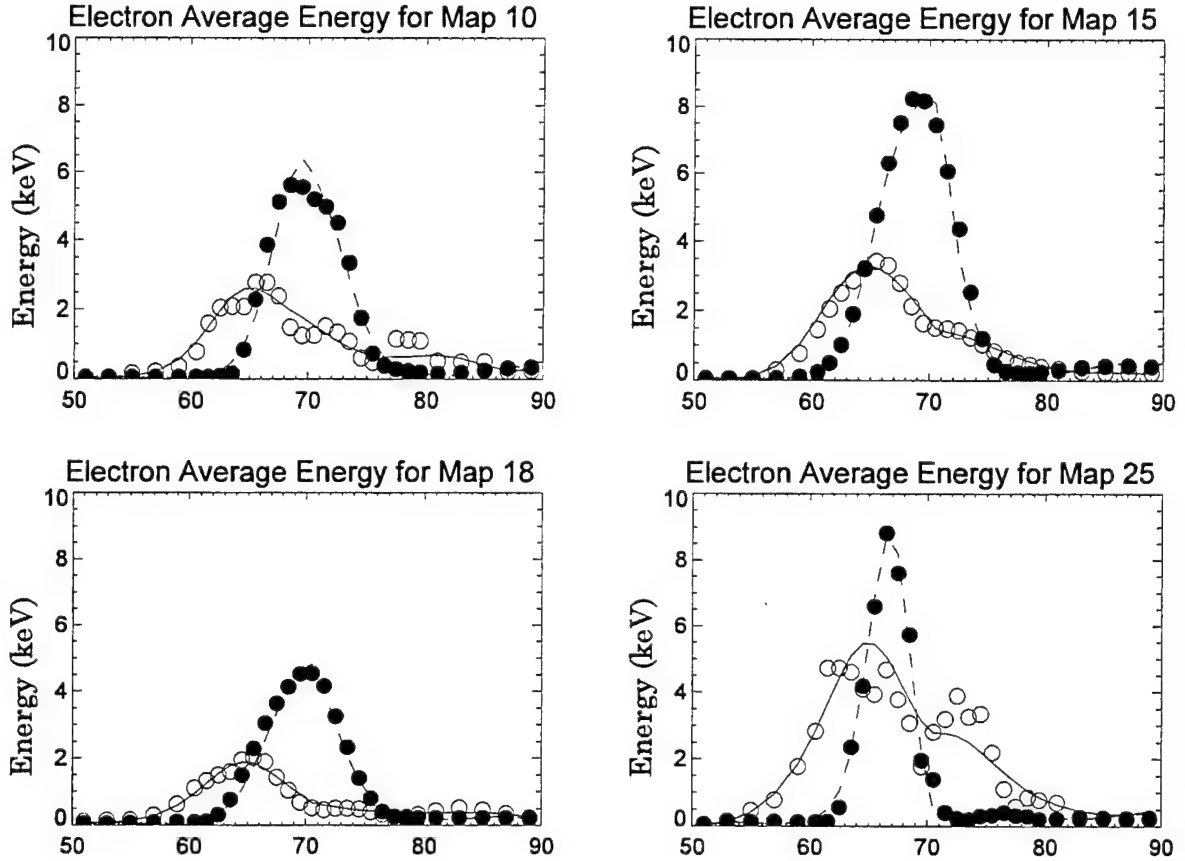


**Figure 39.** Same as Figure 38 Except for the Electron Average Energy From the IMF/SWS maps.

Figure 39 shows the same thing for the electrons. The Chebyshev/Fourier expansion does, perhaps, even better here than for the ions, since the shapes are more Gaussian and regular. The need to consider that the fitting actually reduces the noise in the data and, therefore, should not be judged completely by agreement between the maps and the functions, is especially apparent for Map 25, with the fewest data points.

The following figures show contour plots of the average energy from both the IMF/SWS maps and the $K_p$ maps, comparing the original data with the model fits. In the next section, we present a brief look at the agreement between model and data as judged by errors between the two. While this is by no means a complete analysis, it does at least allow us to compare our results here with those of earlier models, where similar histograms have been presented.

58
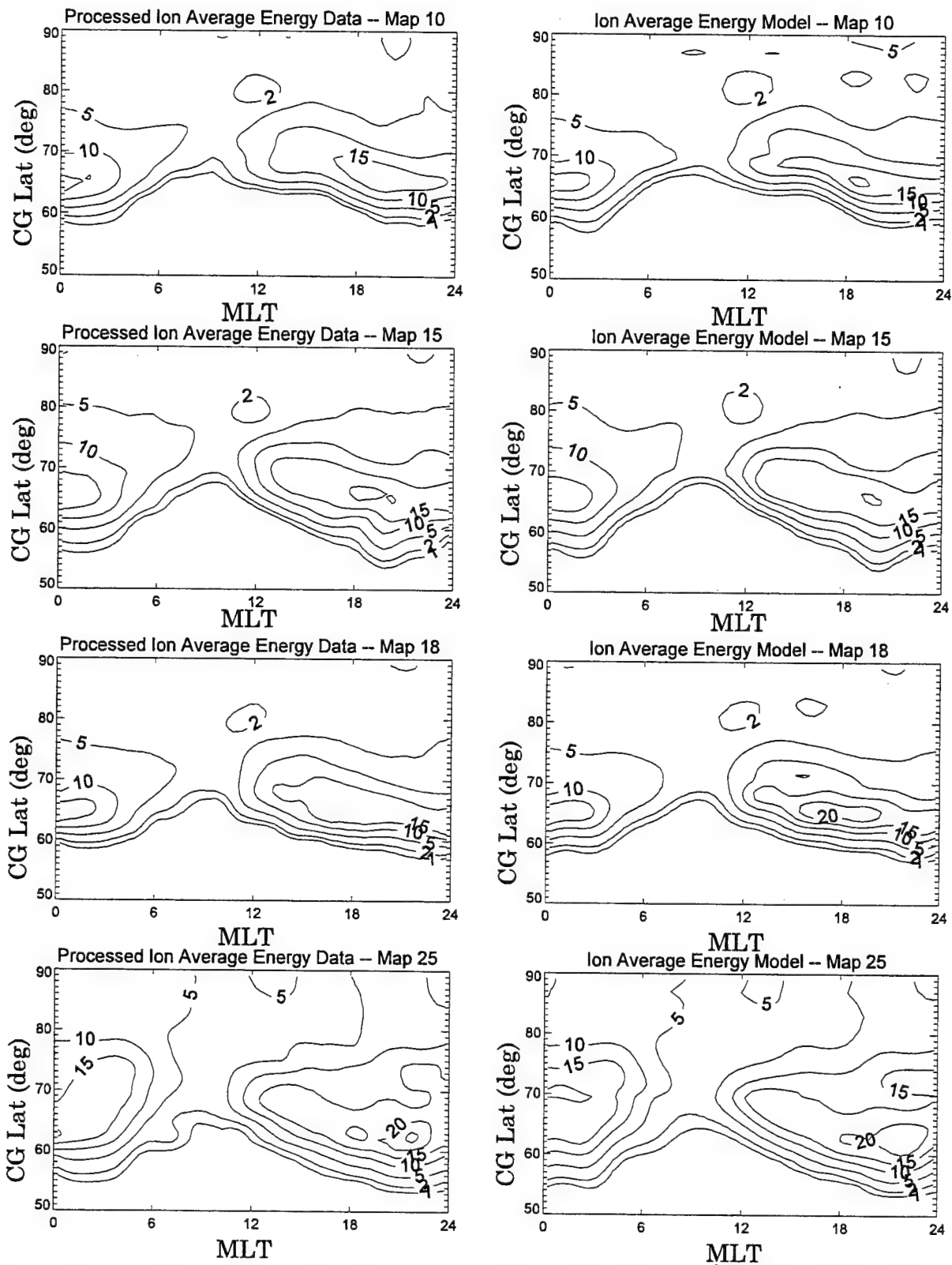
**Figure 40.** Comparison of the Smoothed Ion Average Energy from the IMF/SWS Maps (left) with the Results of Modeling with the Chebyshev/Fourier Expansion (right).

59
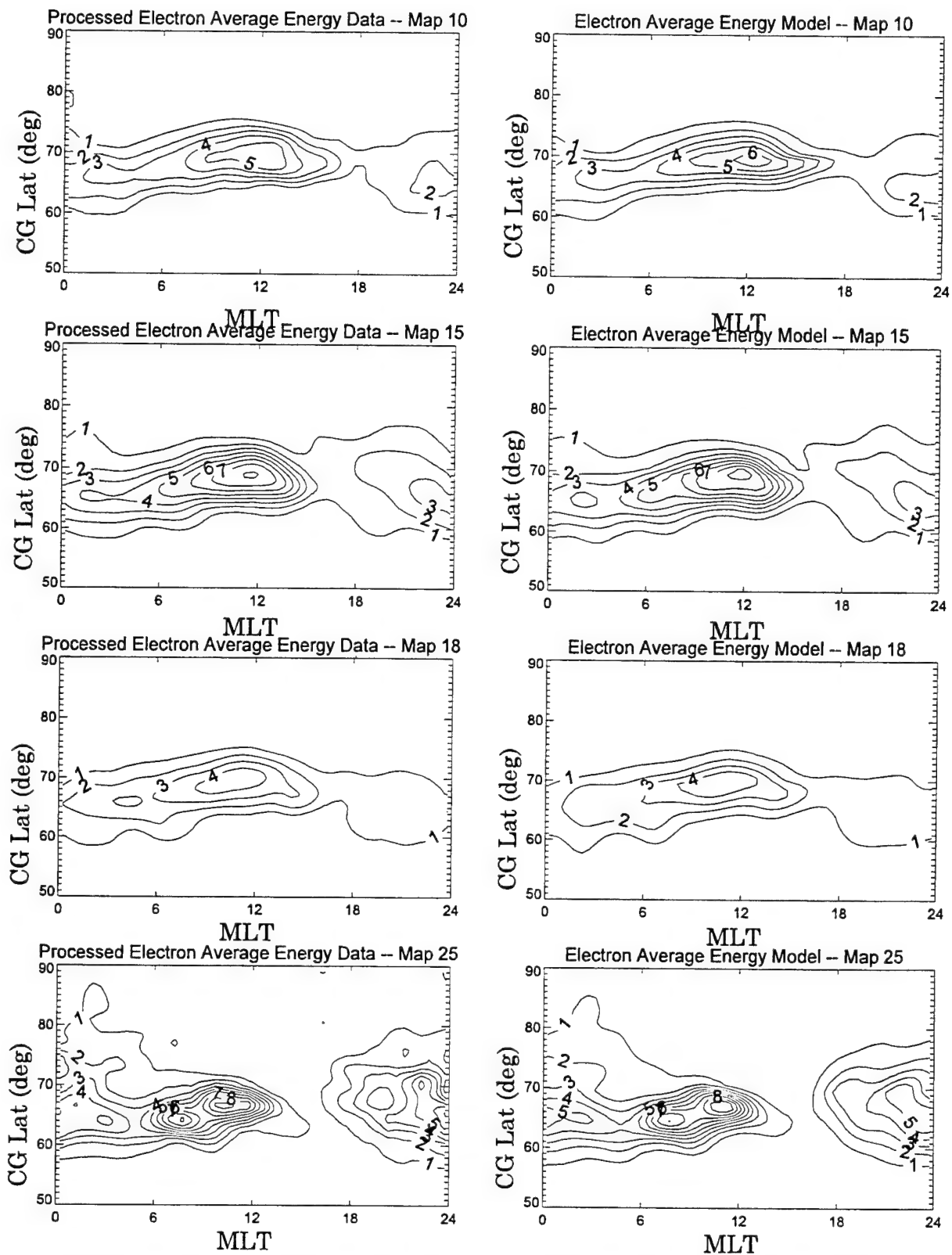
**Figure 41.** Same as Figure 40 Except for the IMF/SWS Electron Average Energy.

60
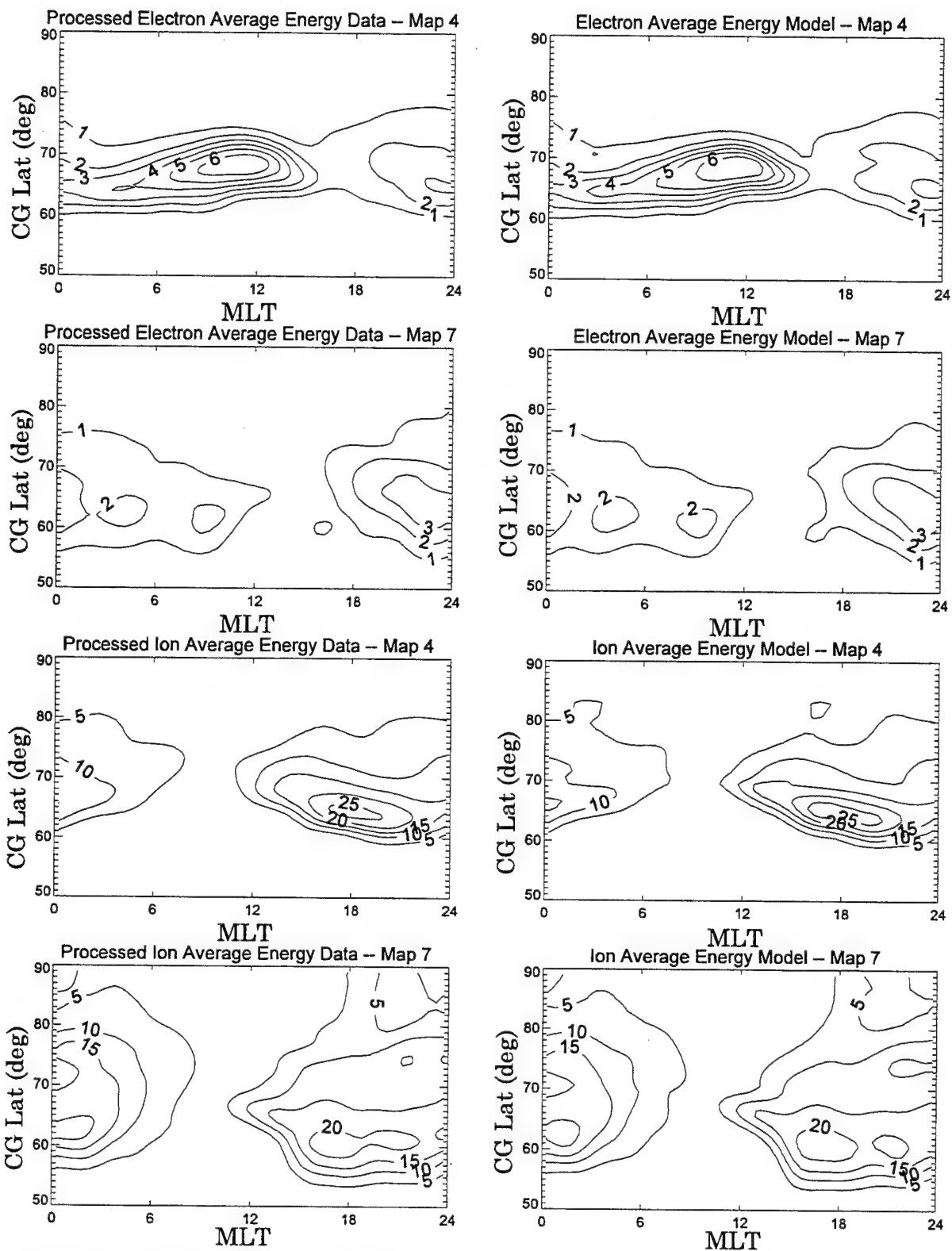
**Figure 42.** Same as Figure 41 Except for the $K_p$ Versions of the Ion and Electron Average Energy.

## 4. Quantitative Analysis of the Fits

In previous comparisons between the data maps and the results of the functional fitting, we have relied primarily on contour plots. These are valuable in assessing the "goodness" of the fits, but a more quantitative measure is also desirable. This is especially so because these fits ought to be compared to those published previously, to show that they are as good or better. The previous models were published in Hardy et al. [1987] concerning the electron fluxes and conductivities and in Hardy et al. [1991] concerning the ion fluxes. We recall that both these involved only $K_p$ maps and that the ion model for $K_p$ here is identical to that in Hardy et al. [1991] with the addition of the average energies to the modeling.

We begin by reproducing the ion flux error histograms from Hardy et al. [1991], which are shown for a representative $K_p$ map in Figure 43. Note that the histograms represent errors between the "smoothed and filled" data and the model. Also, in the case of the ion fluxes, the histograms are made from the flux values themselves, rather than from $\log_{10}F$, which was the quantity actually fit by the Epstein functions.

Hardy et al. [1991] report Full Width Half Maximum (FWHM) Values for $K_p$ Maps 1 and 7 (called Maps 0 and 6 in that report) of the error distributions. These represent the average and least reliable maps, statistically, and therefore provide a good measure for comparisons here, since we have been considering these extreme cases all along. We will use one–half the FWHM value, which is equivalent to the RMS deviation. These are quoted in Table 4.



**Figure 43.** Histograms of Deviations Between Model and Data for Ion Fluxes, Reported in Hardy et al. [1991].

For comparisons with the previously reported quality of the fits, we compute similar histograms along with RMS deviation defined by

$$RMS = \frac{\sqrt{\sum_i (\delta_i - \langle \delta_i \rangle)^2}}{\sqrt{2}\,N} \qquad (18)$$

62

with the $\delta_i$ indicating the ratio of the deviation of the model from the data, divided by the value of the model for one of the grid points (in CG Latitude and MLT) in one of the maps, that is,

$$\delta_i = \frac{Q_i(smoothed\ data) - Q_i(model)}{Q_i(model)} \qquad (19)$$

Hardy et al. [1987] also give the same sort of statistics for the electron properties, fluxes and conductivities, from the previously published electron model, again as a function of $K_p$. These are shown in Figure 44. The captions in this scanned reproduction are difficult to read, but the properties are, clockwise from the upper left, the Pedersen conductivity, the Hall conductivity, the Electron Energy Flux and the Electron Number Flux. Again, Hardy et al. [1987] give FWHM values for Map 3 and Map 6, which although not at the statistical extremes, are adequate for comparisons here. These are also quoted in Table 4.
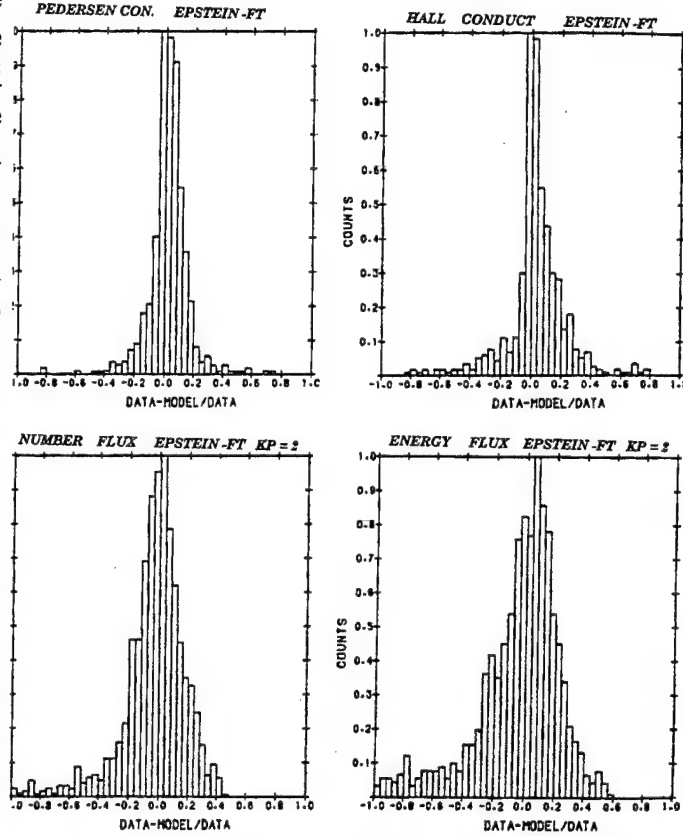


**Figure 44.** Histograms of the Deviations of the Data from the Modeling Results for Four of the Electron Properties Reported by Hardy et al. [1987].

We should remember that the functional forms used in the two prior studies to fit the ion fluxes and the conductivities were identical to those used here, two breakpoint and one breakpoint Epstein functions, respectively. In the previous study, we used a one breakpoint function for the electron fluxes, but in the revised fitting, a two breakpoint function was used. Also, the data set for the $K_p$ electrons was considerably more extensive here than in Hardy et al. [1987]. In the previous studies, average energy models were not accomplished.

In comparing model and data, we take into account the fact that the fluxes are not intended to be especially good far away in CG Latitude from the peak flux. Also, Eq. (19) would produce large and somewhat meaningless values when the flux, or any other quantity, became very small. We therefore limit the data in the histogram to those data points for which the model value is greater than a threshold, roughly equal to the background value in the polar region. These are indicated in Table 4 as well.

| TABLE 4. Error Levels in Original $K_p$ Model of Auroral Properties | | | |
|---|---|---|---|
| Quantity | Map 0 RMS | Map 6 RMS | Threshold |
| Ion Number Flux | 0.22 | 0.22 | $1 \times 10^5$ |
| Ion Energy Flux | 0.24 | 0.26 | $1 \times 10^5$ |
| Electron Number Flux | 0.08 | 0.16 | $1 \times 10^7$ |
| Electron Energy Flux | 0.20 | 0.20 | $1 \times 10^7$ |
| Hall Conductivity | 0.06 | 0.16 | 1 |
| Pedersen Conductivity | 0.08 | 0.10 | 1 |

Figures 45–48 show the IMF/SWS error histograms for these quantities, with the addition of the average energies, which again were not fit in the previous work. The RMS values for the electron and ion fluxes and the conductivities compare quite well with the previous work, with the possible exception of Map 18 in which there are several points, especially in the ion energy flux, for which the data greatly exceeds the model. Looking back at Figure 24, we see that this was probably because the "polar flux" in this case exceeded the threshold of $1 \times 10^5$ and was therefore included in the model. The statistically least populated case, Map 25, slightly exceeds the error level of the previous models, which is perhaps understandable because of the relatively poorer statistics in the IMF/SWS model, compared to the $K_p$ maps. The RMS errors in the average energy are very good, as are the median values, which are unity to better than 2%. This shows that the Chebyshev/Fourier expansion has succeeded in capturing the behavior. For the average energies, a threshold of 1 was used here.

The figures following show the histograms for the $K_p$ versions of the maps, omitting the Ion Fluxes. As mentioned several times before, the maps for the ion fluxes in the $K_p$ model were not redone in this fitting because the functional form and the data included in the maps was the same as that in Hardy *et al.* [1991]. Therefore the model did not need to be refit. For this reason, we cannot produce these histograms because we did not go to the trouble of editing and smoothing the data for all seven maps. Since the model and data are the same, though, the histograms in Figure 43 apply.

We note that the electron energy flux is a somewhat better fit than the original model, probably because the functional form has two extra coefficients and also because there are more data in the maps, leading to less noise in the data. The conductivities are about as good this time as last, so it is probable that the conductivity model is about as reliable as that in Hardy *et al.* [1987], although we have made no direct comparisons. Probably the most attractive feature of the AF–SAM models, over the previous ones, is that they are self–consistent in data source and functional forms.
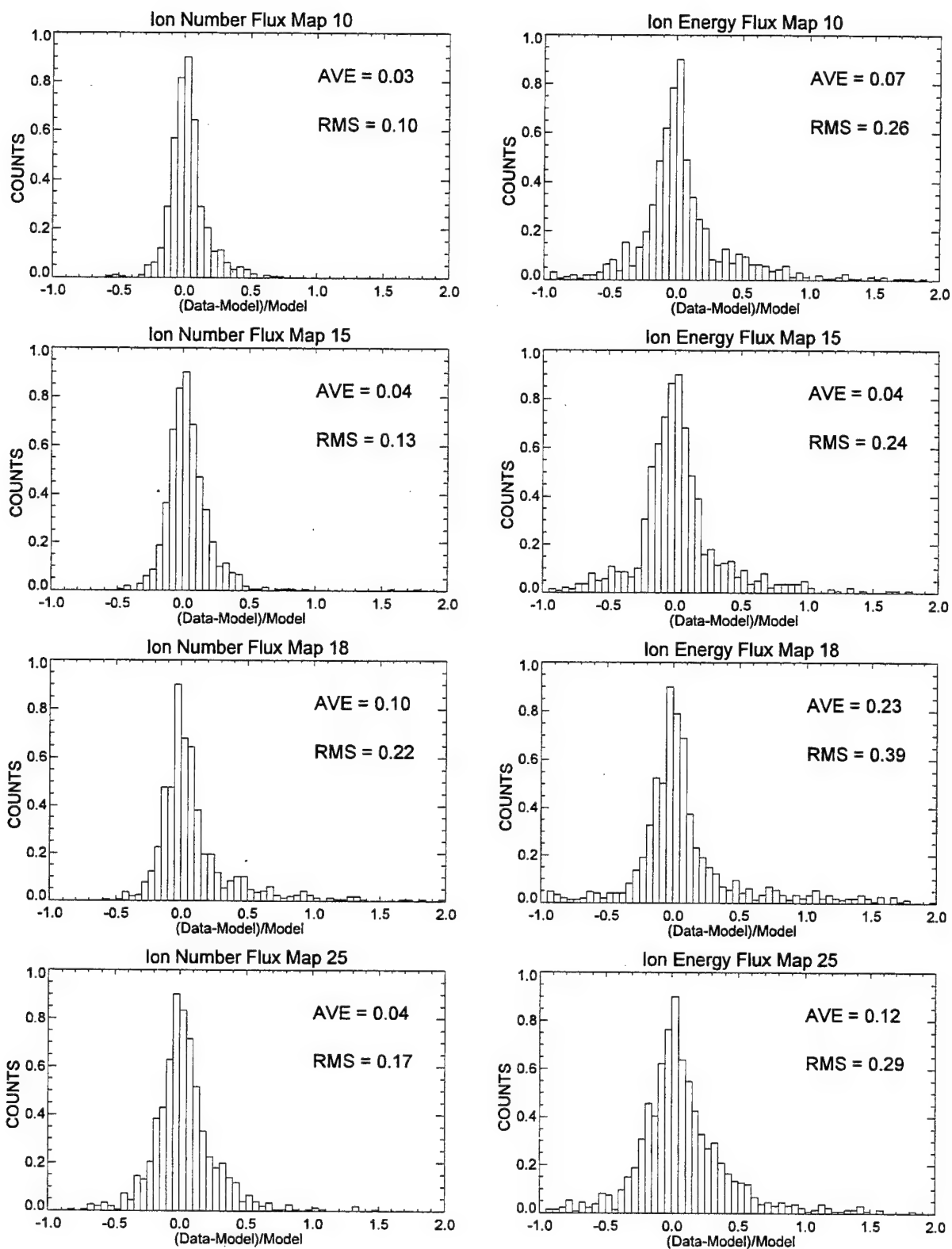
**Figure 45.** Histograms of the Difference Between the Smoothed, Edited Values of the Ion Number (left) and Energy (right) Flux for Four of the IMF/SWS Maps. All data points in the original maps were used above a threshold of $1 \times 10^5$. The histograms are normalized to unity.
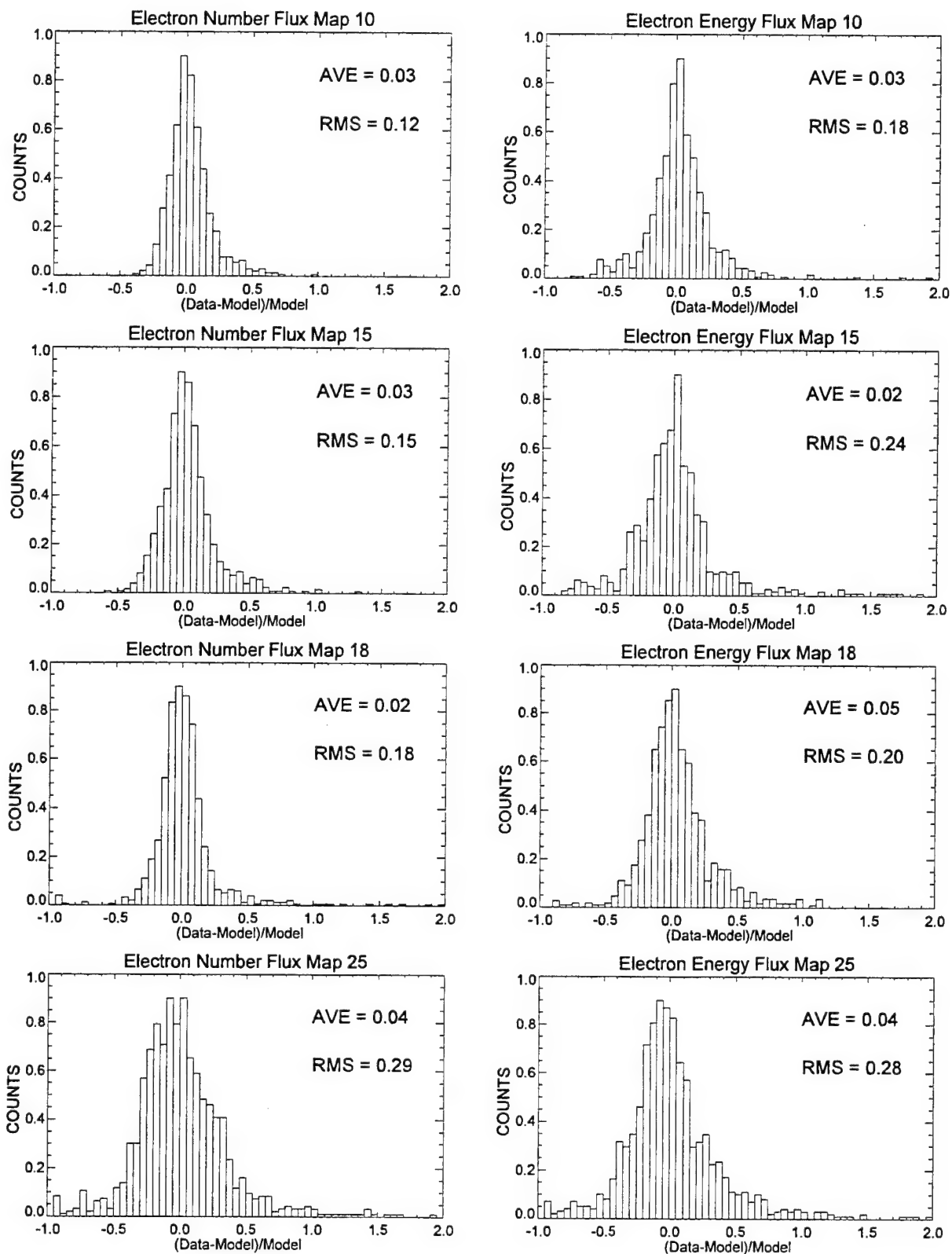
**Figure 46.** Same as Figure 45, Except for the Electron Number Flux and Electron Energy Flux. The threshold is taken at $1 \times 10^7$.

66
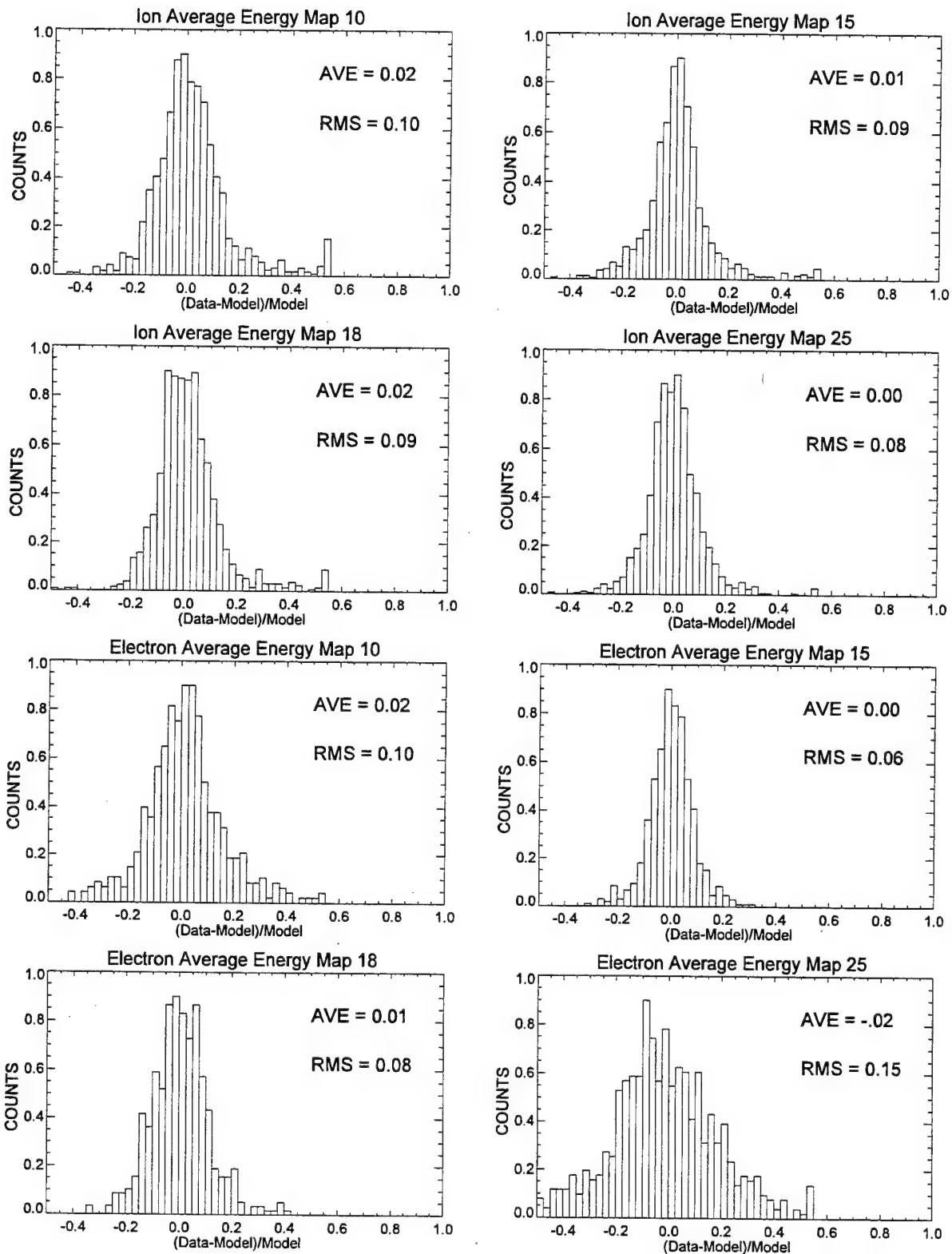
**Figure 47**. Same as Figure 46, Except for the Ion (top) and Electron (bottom) Average Energy. The threshold is taken at 1 keV.

67
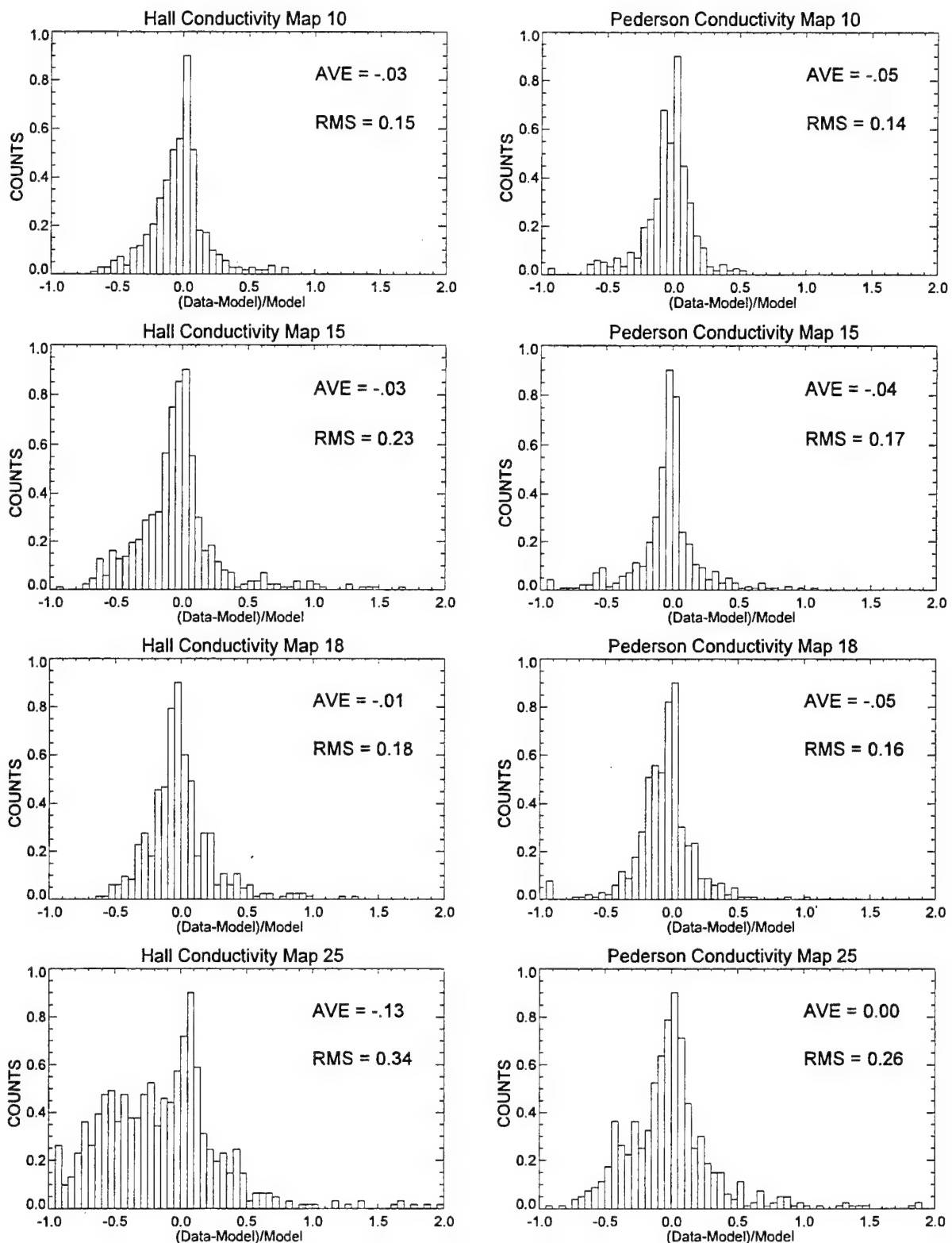
**Figure 48.** Same as Figure 47, Except for the Hall (left) and Pedersen (right) Conductivities. The threshold is taken at 1 mho.

68
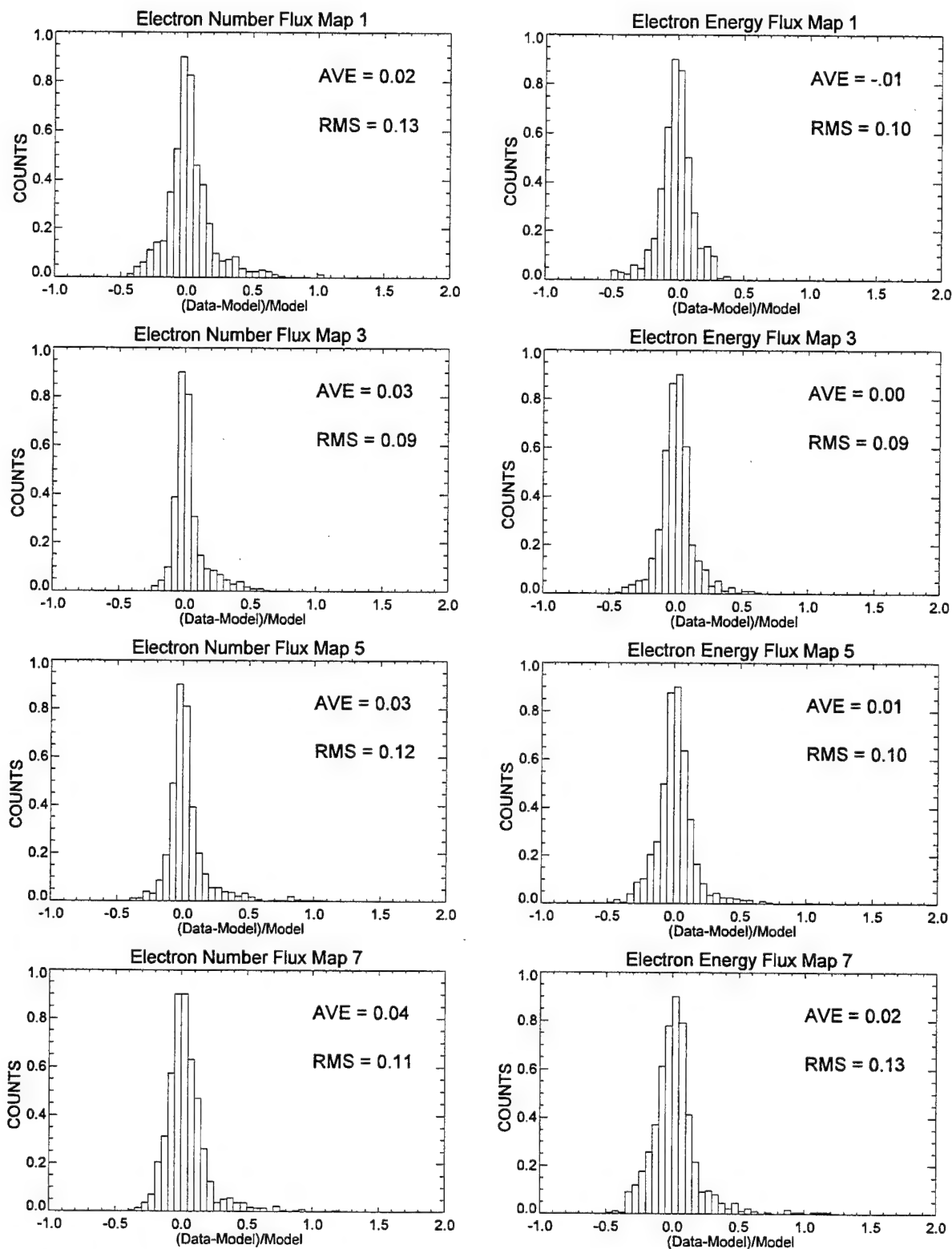
**Figure 49.** Histograms of the Difference Between the Data and Model for the $K_p$ Versions of the Electron Number Flux (left) and Electron Energy Flux (right). The threshold is $1 \times 10^7$.
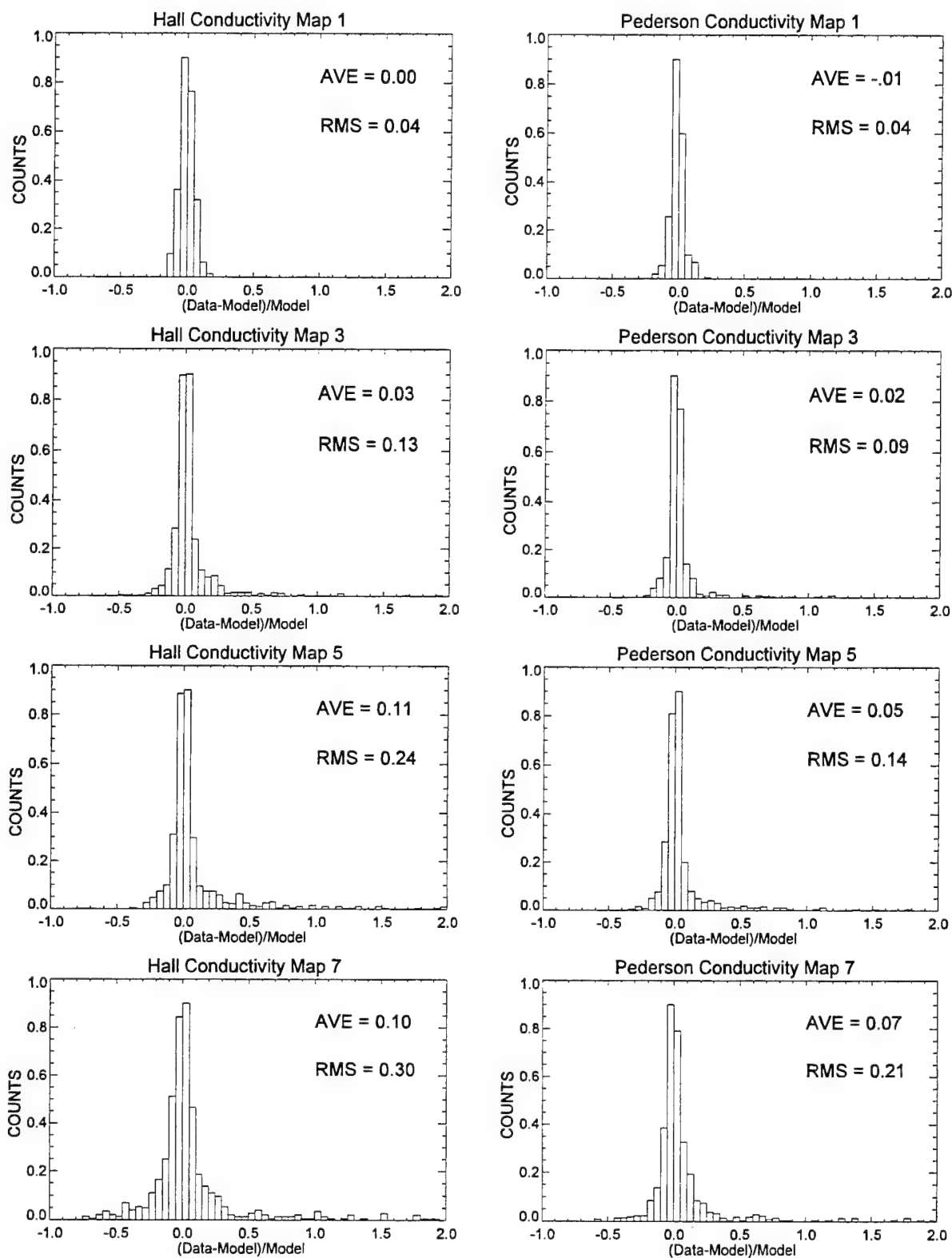
**Figure 50.** Same as Figure 49 Except for the Hall (left) and Pedersen (right) Conductivities. The threshold is 1 mho.

70
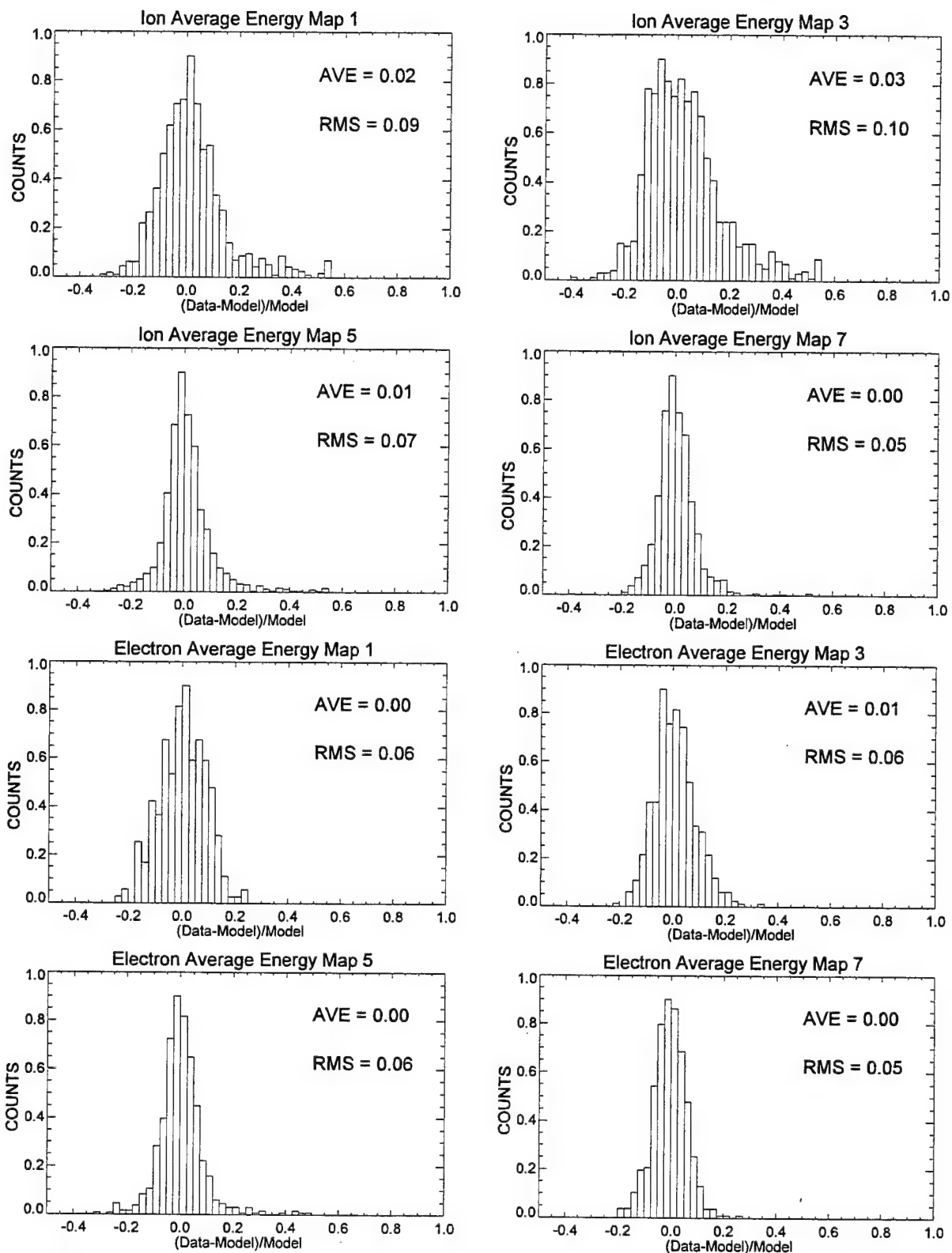
**Figure 51.** Same as Figure 50 Except for the Ion (top) and the Electron (bottom) Average Energy. Threshold is 1 keV.

71

## 5. Use of the Model Subroutines

AFSAM consists of a total of 10 Fortran subroutines along with 10 corresponding ASCII files containing the model coefficients. The names of these routines and data files are listed in Table 5. The routines can be used individually or any can be combined in the same driver code, as individual uses require. They are quite straightforward to use. Upon the first call, each routine looks for the proper data file and loads the coefficients. This saves I/O time on subsequent calls.

| TABLE 5. Model Subroutines and Data Files | | | | |
|:---:|:---:|:---:|:---:|:---:|
| # | Dependency | Property | Subroutine | Data File |
| 1 | IMF/SWS | Electron Fluxes | eleimf.f | eleimf.dat |
| 2 | IMF/SWS | Ion Fluxes | ionimf.f | ionimf.dat |
| 3 | IMF/SWS | Conductivities | conimf.f | conimf.dat |
| 4 | IMF/SWS | Electron Average Energy | eaveimf.f | eaveimf.dat |
| 5 | IMF/SWS | Ion Average Energy | iaveimf.f | iaveimf.dat |
| 6 | $K_p$ | Electron Fluxes | elekp.f | elekp.dat |
| 7 | $K_p$ | Ion Fluxes | ionkp.f | ionkp.dat |
| 8 | $K_p$ | Conductivities | conkp.f | conkp.dat |
| 9 | $K_p$ | Electron Average Energy | eavekp.f | eavekp.dat |
| 10 | $K_p$ | Ion Average Energy | iavekp.f | iavekp.dat |

The user specifies the CG Latitude and MLT desired, in degrees and hours, as well as the desired map, 1-7 for the $K_p$ version and 1-30 for the IMF/SWS model. For the fluxes and conductivities, the user must also specify which of the two quantities are desired. For fluxes, a 1 indicates Number Flux and a 2, Energy Flux. For conductivities, a 1 indicates Hall Conductivity and a 2 indicates Pedersen Conductivity. The computations are quite efficient, as a result of the relatively simple model functions and today's high powered equipment.

Because of the large number of coefficients in the various models, it seemed unnecessary to include all of them in this report. It is not anticipated that any potential user would enter them all by hand. However, for reference, we have included on the next two pages the functions evaluated for both an IMF/SWS and $K_p$ map. The $\log_{10}$ of the number and energy fluxes are listed. The units of the various quantities are particles/cm$^2$–sec–Sr for number flux, particles/cm$^2$–sec–Sr–keV for energy flux, keV for average energy and mohs for conductivity.

AFSAM IMF/SW Model for Map 15 MLT   0.0

| CG Latitude | 55 | 60 | 65 | 70 | 75 | 80 | 85 |
|---|---|---|---|---|---|---|---|
| Electron Number Flux | 4.481 | 6.673 | 8.282 | 8.400 | 8.084 | 6.883 | 6.883 |
| Electron Energy Flux | 4.200 | 6.820 | 8.801 | 8.628 | 8.062 | 6.765 | 6.765 |
| Electron Average Energy | 0.111 | 1.612 | 3.209 | 1.743 | 0.998 | 0.405 | 0.220 |
| Hall Conductivity | 0.000 | 0.000 | 13.654 | 12.991 | 0.500 | 0.500 | 0.500 |
| Pedersen Conductivity | 0.000 | 0.000 | 8.430 | 7.582 | 2.884 | 0.500 | 0.500 |
| Ion Number Flux | 1.453 | 4.738 | 6.519 | 6.222 | 5.425 | 4.735 | 4.735 |
| Ion Energy Flux | 1.707 | 5.455 | 7.794 | 7.343 | 6.393 | 5.438 | 5.367 |
| Ion Average Energy | 0.174 | 4.564 | 17.546 | 13.549 | 8.793 | 5.426 | 3.525 |

AFSAM IMF/SW Model for Map 15 MLT   6.0

| CG Latitude | 55 | 60 | 65 | 70 | 75 | 80 | 85 |
|---|---|---|---|---|---|---|---|
| Electron Number Flux | 4.176 | 5.821 | 7.430 | 8.227 | 8.330 | 7.703 | 6.906 |
| Electron Energy Flux | 2.678 | 5.480 | 8.115 | 8.594 | 8.134 | 7.461 | 6.765 |
| Electron Average Energy | 0.128 | 0.942 | 5.126 | 2.390 | 0.698 | 0.482 | 0.328 |
| Hall Conductivity | 0.000 | 0.000 | 10.194 | 11.970 | 0.500 | 0.500 | 0.500 |
| Pedersen Conductivity | 0.000 | 0.000 | 3.759 | 6.804 | 2.718 | 0.500 | 0.500 |
| Ion Number Flux | 2.436 | 3.973 | 5.503 | 6.557 | 6.273 | 5.466 | 4.735 |
| Ion Energy Flux | 0.000 | 1.195 | 5.678 | 7.334 | 7.034 | 6.183 | 5.367 |
| Ion Average Energy | 0.028 | 0.122 | 2.508 | 6.482 | 6.120 | 4.563 | 4.048 |

AFSAM IMF/SW Model for Map 15 MLT  12.0

| CG Latitude | 55 | 60 | 65 | 70 | 75 | 80 | 85 |
|---|---|---|---|---|---|---|---|
| Electron Number Flux | 2.778 | 4.073 | 5.367 | 6.677 | 8.244 | 7.859 | 6.883 |
| Electron Energy Flux | 3.302 | 5.087 | 6.858 | 7.919 | 7.864 | 7.198 | 6.765 |
| Electron Average Energy | 0.047 | 0.184 | 4.060 | 8.674 | 0.797 | 0.210 | 0.466 |
| Hall Conductivity | 0.000 | 0.000 | 2.844 | 6.942 | 3.043 | 0.500 | 0.500 |
| Pedersen Conductivity | 0.000 | 0.000 | 0.480 | 1.671 | 2.092 | 0.500 | 0.500 |
| Ion Number Flux | 3.134 | 3.952 | 4.769 | 5.589 | 6.540 | 6.337 | 4.735 |
| Ion Energy Flux | 0.000 | 0.828 | 4.245 | 6.615 | 7.177 | 6.484 | 5.367 |
| Ion Average Energy | 0.030 | 0.035 | 1.681 | 11.343 | 4.641 | 1.467 | 2.942 |

AFSAM IMF/SW Model for Map 15 MLT  18.0

| CG Latitude | 55 | 60 | 65 | 70 | 75 | 80 | 85 |
|---|---|---|---|---|---|---|---|
| Electron Number Flux | 1.335 | 3.968 | 6.534 | 8.048 | 8.002 | 7.286 | 6.883 |
| Electron Energy Flux | 3.633 | 5.280 | 6.945 | 8.475 | 7.856 | 6.765 | 6.765 |
| Electron Average Energy | 0.055 | 0.541 | 1.633 | 2.182 | 0.881 | 0.306 | 0.308 |
| Hall Conductivity | 0.000 | 0.000 | 2.150 | 7.347 | 2.852 | 0.500 | 0.500 |
| Pedersen Conductivity | 0.000 | 0.000 | 0.000 | 5.754 | 2.878 | 0.500 | 0.500 |
| Ion Number Flux | 0.000 | 2.871 | 5.702 | 6.391 | 5.800 | 4.993 | 4.735 |
| Ion Energy Flux | 0.000 | 1.692 | 6.778 | 7.527 | 6.605 | 5.502 | 5.367 |
| Ion Average Energy | 0.141 | 4.765 | 17.945 | 14.746 | 7.033 | 4.822 | 4.234 |

```
AFSAM Kp Model for Kp  1 MLT  0.0

CG Latitude              55      60      65      70      75      80      85

      Electron Number Flux   3.048   5.251   7.390   8.174   7.677   7.027   7.027
      Electron Energy Flux   1.429   4.587   7.586   8.241   7.469   7.185   7.185
   Electron Average Energy   0.043   0.504   1.748   1.165   0.733   0.499   0.420
         Hall Conductivity   0.000   0.000   4.861   4.197   0.500   0.500   0.500
      Pedersen Conductivity  0.000   0.000   3.291   4.292   1.416   0.500   0.500
          Ion Number Flux    0.000   2.058   6.245   6.202   5.283   5.149   5.149
          Ion Energy Flux    0.000   0.326   7.299   7.128   6.107   5.800   5.800
        Ion Average Energy   0.025   0.214   8.879   6.187   5.173   3.715   4.350


AFSAM Kp Model for Kp  1 MLT  6.0

CG Latitude              55      60      65      70      75      80      85

      Electron Number Flux   4.545   5.709   6.870   7.887   8.227   7.974   7.402
      Electron Energy Flux   2.288   4.619   6.931   8.269   7.920   7.453   7.185
   Electron Average Energy   0.041   0.100   1.474   2.583   0.560   0.314   0.350
         Hall Conductivity   0.000   0.000   2.163   6.675   0.500   0.500   0.500
      Pedersen Conductivity  0.000   0.000   1.339   4.579   1.885   0.500   0.500
          Ion Number Flux    0.389   2.434   4.477   6.268   6.536   6.002   5.365
          Ion Energy Flux    0.000   0.000   3.678   7.181   7.103   6.394   5.800
        Ion Average Energy   0.042   0.024   0.475   6.801   4.053   3.125   3.628


AFSAM Kp Model for Kp  1 MLT 12.0

CG Latitude              55      60      65      70      75      80      85

      Electron Number Flux   5.099   5.682   6.264   6.855   7.798   8.286   7.478
      Electron Energy Flux   0.874   3.379   5.872   7.612   7.782   7.557   7.185
   Electron Average Energy   0.087   0.052   0.705   4.474   1.439   0.203   0.353
         Hall Conductivity   0.000   0.000   1.016   4.250   2.956   0.500   0.500
      Pedersen Conductivity  0.000   0.000   0.303   1.702   2.159   0.500   0.500
          Ion Number Flux    2.209   3.175   4.140   5.108   6.212   6.926   5.621
          Ion Energy Flux    0.000   0.000   3.868   6.350   6.919   7.009   6.143
        Ion Average Energy   0.032   0.022   1.220   8.542   4.325   1.593   2.685


AFSAM Kp Model for Kp  1 MLT 18.0

CG Latitude              55      60      65      70      75      80      85

      Electron Number Flux   2.849   4.397   5.944   7.452   8.128   7.962   7.384
      Electron Energy Flux   0.932   3.300   5.661   7.502   7.930   7.463   7.185
   Electron Average Energy   0.030   0.042   0.660   1.140   0.653   0.385   0.475
         Hall Conductivity   0.000   0.000   0.545   2.017   1.642   0.924   0.500
      Pedersen Conductivity  0.000   0.000   0.000   1.938   2.212   1.248   0.500
          Ion Number Flux    0.845   2.897   4.941   6.430   6.421   5.884   5.149
          Ion Energy Flux    0.000   0.000   5.206   7.414   6.953   6.258   5.800
        Ion Average Energy   0.027   0.040   3.967  11.309   5.420   3.745   4.124
```

# 6. Summary

We have presented the details of data treatment and fitting that were carried out to provide functional representations of statistical maps of auroral properties generated from a great deal of DMSP electron and ion flux data. The models represent the average auroral conditions under both 7 divisions of $K_p$ as well as 30 divisions of IMF and Solar Wind Speed. The models include Number and Energy Flux for both Electrons and Ions and Hall and Pedersen Conductivities. These are represented by an Epstein function in CG Latitude and a Fourier series in MLT. The Average Energies for both Ions and Electrons are also modeled, with a combination Chebyshev/Fourier expansion in the same coordinates.

We have presented analysis of the extent to which the functional forms preserve the features of the original statistical maps. Through both contour plots and through error histograms, we have found that the modeling does not significantly alter the numerical results of the statistical studies and, in many cases, improves them through smoothing of minor statistical fluctuations. The results have been surveyed quite extensively and modifications have been made where necessary to preserve the quality of the fits. The user can therefore use these models with a high degree of confidence.

The Air Force Statistical Auroral Model (AFSAM) is an extension of earlier work [*Hardy et al.*, 1987;1991] providing a better representation of auroral electron fluxes and including electron and ion average energies, and should be considered a replacement to those earlier models. The models provide a convenient method to specify the aurora under various magnetospheric conditions, appropriate both to graphical displays and warning systems and to further, theoretical studies requiring auroral quantities as input.

# References

Bhavnani, K.H. and R.P. Vancour, *Coordinate systems for space and geophysical applications*, Phillips Laboratory, Hanscom AFB, MA, PL-TR-91-2296, 11 December 1991, ADA247550.

Brautigam, D.H., M.S. Gussenhoven and D.A. Hardy, A statistical study of the effects of IMF $B_z$ and solar wind speed on auroral ion and electron precipitation, *J. Geophys. Res.*, **96**, 5525, 1991.

Brautigam, D.H., W. McNeil, D. Hardy, and M. Gussenhoven, Air Force Statistical Auroral Models (AFSAM), presented at AGU Fall Meeting, San Francisco, California, 6–10 December 1998.

Hardy, D.A., M.S. Gussenhoven and E. Holeman, A statistical model of auroral electron precipitation, *J. Geophys. Res.*, **90**, 4229, 1985.

Hardy, D.A., M.S. Gussenhoven, R. Raistrick and W.J. McNeil, Statistical and functional representation of the pattern of auroral energy flux, number flux and conductivity, *J. Geophys. Res.*, **92**, 12,275, 1987.

Hardy, D.A., M.S. Gussenhoven and D.H. Brautigam, A statistical model of auroral ion precipitation, *J. Geophys. Res.*, **94**, 370, 1989.

Hardy, D.A., W. McNeil, M.S. Gussenhoven and D. Brautigam, A statistical model of auroral ion precipitation 2: Functional representation of the average patterns, *J. Geophys. Res.*, **96**, 5539, 1991.